Distribution Agreement

In presenting this thesis or dissertation as a partial fulfillment of the requirements for an advanced degree from Emory University, I hereby grant to Emory University and its agents the non-exclusive license to archive, make accessible, and display my thesis or dissertation in whole or in part in all forms of media, now or hereafter known, including display on the world wide web. I understand that I may select some access restrictions as part of the online submission of this thesis or dissertation. I retain all ownership rights to the copy right of the thesis or dissertation. I also retain the right to use in future works (such as articles or books) all or part of this thesis or dissertation.

Signature: Date:

Elasticity and Structure of Self-Assembled Systems with Defects and Inclusions

By

Ana West
Doctor of Philosophy
in Chemistry

Dr. James Kindt, Prof. of Chemistry
Advisor and Committee Member

Dr. Joel Bowman, Prof. of Chemistry
Committee Member

Dr. Tim Lian, Prof. of Chemistry
Committee Member

Dr. Eric Weeks, Prof. of Physics
Committee Member

Accepted:

Lisa A. Tedesco, PhD.
Dean of the James T. Laney School of Graduate Studies

Date

Elasticity and Structure of Self-Assembled Systems with Defects and Inclusions

By

Ana West
B.S., Kennesaw State University, 2006

Advisor: Prof. James T. Kindt, PhD

An abstract of
a dissertation submitted to the Faculty of the
James T. Laney School of Graduate Studies of Emory University
in partial fulfillment of the requirements for the degree of
Doctor of Philosophy
in Chemistry
2013

Abstract

Elasticity and Structure of Self-Assembled Systems with Defects and Inclusions

By Ana West

In this work we study the manner in which topological defects and inclusions alter the dynamics, the elasticity, and the conformational structure of three self-assembled molecular systems.

System 1: Protein hydrogels are responsive materials that form upon mixing natural or engineered peptides known as "junctions" and "linkers". There is great interest to employ protein hydrogels in biomedical applications especially as controlled-release drug delivery agents and as tissue engineering scaffolds. In this work we designed a simulation model of divalent linkers and junctions and evaluated how defects such as a stoichiometric mismatch in mixing components and loops couple with the long-time relaxation of shear stress and resulting viscosity. Junction multiplicities (ν) from three to nine are considered. The linker stiffness and the modes of pairs of junctions bonding are also explored. A stoichiometric mismatch as small as 1% in mixing peptides concentrations showed a sharp decrease in both shear relaxation time (τ_{shear}) and network viscosity. The rate of stress relaxation per bond re-arrangement event is two to three times increased than assumed in previous theories. The values of shear plateau moduli, (G^o) strongly deviates from the Gaussian chain predicting a linear relationship in number of linkers in the system (N_L). A simple phenomenological theory is developed to connect the findings of various simulation instances. The material properties such as G^o and τ_{shear} are related to the lifetime of a bond, τ_{bond}.

System 2: Evaluating the lipid membrane elasticity during processes that

require the lipid membrane to stretch, bend, break, or re-organize is essential to understanding cell membrane function. In this simulation study we investigate the edge tension of a bilayer edge resulting from having pores in lipid bilayers. Edge tension values reported from experiments vary greatly with method of investigation and techniques of edge tension detection are still being developed. In this study, simulations carried out for dioleoyl phosphatidylcholine (DOPC) with three different force-field parameter sets yielded edge line tensions of ∼45 pN, over 50% greater than the most recently reported experimentally determined value for this lipid. Edge tensions obtained from simulations of a series of phosphatidylcholine (PC) lipid bilayer ribbons with saturated acyl tails of length 12-16 carbons and with mono-unsaturated acyl tails of length 14-18 carbons is correlated with the excess area associated with forming the edge, through a two-parameter fit.

System 3: Quantum dots (QDs) are highly sought optical probes in biomedical imaging. Recent experiments showed increased photoluminescence stability and selective ligand exchange processes when small size CdSe QDs were embedded in the wall of small unimellar vesicles made of different phase lipid. The precise molecular details of lipid-ligand interface during the QD embedding instances are unknown. In this report we implemented united atom simulations to provide such a characterization. A 2.6 nm diameter QD and a 3.4 nm diameter QD both capped with oleic acid (OA) ligands are embedded in dilauroyl phosphatidylcholine (DLPC), dioleoyl phosphatidylcholine (DOPC),dimyristoyl phosphatidylcholine(DMPC), and distearoyl phosphatidylcholine (DSPC) lipid bilayers. The ligand density at same size QD and the initial QD embedding orientation is also varied. The lipid tail conformational disorder is evaluated as a distance dependent deuterium order parameter. More ordered lipid tails are observed for smaller size QDs and at lower employed ligand density. Orientational autocorrelation functions of lipid tails interacting with QD ligands show that the lipid tail mobility correlates with lipid phase independently of both nanocrystal size and capping ligand density.

Elasticity and Structure of Self-Assembled Systems with Defects and Inclusions

By

Ana West
B.S., Kennesaw State University, 2006

Advisor: Prof. James T. Kindt, PhD

A dissertation submitted to the Faculty of the
James T. Laney School of Graduate Studies of Emory University
in partial fulfillment of the requirements for the degree of
Doctor of Philosophy
in Chemistry
2013

"One thing I have learned in a long life: that all our science, measured against reality, is primitive and childlike – and yet it is the most precious thing we have." -Albert Einstein

Acknowledgements

I owe my profound gratitude to Prof. James Kindt, my thesis advisor for giving me the opportunity to work with his research group. The final outcome of this thesis would've not been possible without his guidance and his patience. During my time as his student I grew to admire how careful he is as a scientist and how deep his understanding of simulation methods and theory development really runs. He is brilliant! I thank him also for allowing me to pursue different research curiosities and for always challenging and inspiring me to improve and to find my own strengths/abilities/interests. I also heartily thank former and current Kindt group members, Dr. Fuchang Yin, Dr. Patrick Coppock, Dr. Hao Wang, Mr. Lewen Yang, and Ms. Lara Patel for their upbeat outlook on things.

I am also very grateful to committee member Prof. Eric Weeks from Emory's Physics Department for suggestions during the pre-examination process of studies included in this thesis and when completing other degree requirements. I also admire prof. Weeks' selfless willingness to teach and to mentor all students interested in *Soft Matter* topics. From the same department I want to thank Dr. Connie Roth for organizing and chairing the discussions of literature articles during the *Soft Matter* journal club.

I thank committee members Prof. Joel Bowman and Prof. Tim Lian for teaching me graduate courses in physical chemistry. I distinctly remember how splendidly prof. Bowman introduced the basics of quantum mechanics. Prof. Lian included quantum dot spectroscopy related theory in our courses/cumulative exams. I also credit him for inspiring my interest in quantum dot research.

I thank experimental collaborators of work on quantum dots in lipid bilayers, Dr. Khalid Salaita and his postdoc Dr. Weiwei Zheng as their studies guided my own simulation analysis. I also want to thank Dr. Justin Gallivan and his former student, Dr. Shana Topp for introducing me to the experimental side of reversible biomaterials work.

I was also fortunate enough to be involved with several teaching activities for which I am most grateful to Dr. Daphne Norton. I also enjoyed a great deal working with Renee Stein, a conservator from Carlos Museum.

I thank Dr. Henryk Witek and his student Chen-Pin Chou from NCTU in Taiwan for so graciously hosting a travelling abroad research experience.

From previous schooling I thank Dr. Janet Shaw, Dr. Philippe Laval, and Dr. Kevin Gwaltney of KSU for their enthusiasm in teaching and in advising students.

I also thank Emerson Center administrator Dr. Alexis Kaledin, and Prof. Jamal Musaev for making themselves so readily available in answering questions regarding computational hardware/software needs.I also thank Emory Laney Graduate School for financial support to attend professional conferences.

Finally I want to thank my family, especially John, Florentina, Miha, and my parents for their support.

Summary

In chapter 1 we briefly mention relevant statistical mechanics concepts and related molecular dynamics (MD) and Monte-Carlo (MC) simulation details. Chapter 2 provides the experimental and theoretical context to the peptide biomaterial studies. Work presented in Chapter 3 amounts to describing a new simulation model of divalent linkers and junctions that evaluates how defects such as a stoichiometric mismatch in mixing components and linker flexibility couples with the long-time relaxation of shear stress and resulting viscosity. Junction multiplicities (ν) from three to five are considered. Furthermore, the manner in which defects affect the time-dependent viscosity during gel aging is modeled as an approach to equilibrium through diffusion-limited recombination of complementary defects. In chapter 4 we expand the simulation model to also include networks with junction functionality six to nine. Loops and multiple bonding between pairs of junctions are also investigated. A simple model to connect the fraction of linkers involved in multiple junction bonding to network junction valency to number of available sites on neighboring sites is developed. A new interpretation of shear-relaxation rate is proposed, a theoretical framework that accounts for the simulation non-linear relationship between plateau shear modulus (G^0) and number of elastic chains (N_L). Chapter 5 is a brief introduction to lipid bilayer work, especially relevant to studies of Chapter 6, simulation work that characterizes both the lipid packing at the edge and the magnitude of edge tension of bilayers with pores. In Chapter 7 we explore via molecular dynamics simulation the structure and the dynamics of ligand-lipid interface from when incorporating different size quantum dots in lipid bilayers.

Contents

List of Figures

List of Tables

Published Work

Content of chapter 3 was published as:

A. West and J.T. Kindt, “Effects of defects on shear stress relaxation in selfassembled protein networks.” Soft Matter 8, 2895-2906 (2012).

Content of chapter 6 was published as:

A. West, K. Ma, J. L. Chung, and J. T. Kindt , “Simulation studies of structure and line tension of lipid bilayer edges: effects of tail structure and force-field.”J. Phys. Chem. A 117(32):7114-23 (2013)

Abbreviations

Chapters 5-7

DLPC:

dilauroyl phosphatidylcholine or
1,2-didodecanoyl-sn-glycero-3-phosphocholine

DMPC:

dimyristoyl phosphatidylcholine or
1,2-ditetradecanoyl-sn-glycero-3 phosphocholine

DSPC:

distearoyl phosphatidylcholine or 1,2-dioctadecanoyl-sn-glycero-3-phosphocholine

DOPC:

dioleoyl phosphatidylcholine or 1,2-di-(9Z-octadecenoyl)-sn-glycero-3-phosphocholine

POPC:

1-palmitoyl-2-oleoyl-phosphatidylcholine or 1-hexadecanoyl-2-(9Z-octadecenoyl)-sn-glycero-3-phosphocholine

OA:

oleic acid or (9Z)-Octadec-9-enoic acid

1

Simulation

Modern scientific inquiry strives to understand how nature works from carrying out lab experiments, from using and developing physical theory, and from conducting simulation.(1) Measurements made during experiments result in attributing specific numeric values to a property of interest. Physical theory consists in constructing greatly simplified mathematical models of the systems investigated in experiments and then calculating the same property. The solutions proposed from such theoretical models are often mere approximations and limited to describe idealized cases and general trends and are not always extremely useful to quantitatively interpret experimental values. Simulations are “numerical experiments” that aim to bridge the gap between experiment values and approximations of physical theory(1). Simulations also complement scientific findings as they can probe resolution of structural detail not easily available in experiment.

In simulation a model of the system still need be initially constructed and similar to theory may involve ignoring a great deal of complexity of physical systems. If sufficient microscopic information is available to input into the designed model, in many cases existing simulations methodologies today evolved to the point that values obtained from a particular simulation instance corresponds to a highly specific experimental investigation.

1.1 Foundational Statistical Mechanics Related Concepts

All macroscopic properties measured in physical chemistry experiments can be calculated from statistical mechanics related theory, which reports them as ensemble averages. An ensemble is an exhaustive, unique list of all allowed microstates of the system paired with their associated probabilities. A microstate of a system refers to each microscopic variable taking on a specific value. In the context of statistical mechanics, the system under investigation first need be assigned a microscopic description. For a classical system, a complete microscopic description means specifying the configuration phase space Γ of microstates , a vector space over which a function may be defined constructed from assigning a configurational coordinate and a momentum coordinate to all N particles in the system (2) :

$$\Gamma = (r^N, p^N) \tag{1.1}$$

In this notation, the vector r^N represents the position space,also called configuration space, and the vector p^N is the momentum space. The phase space may contain many constant energy surfaces, which are subspaces of Γ of reduced dimensionality. The Hamiltonian of the system is denoted $H(\Gamma)$. Specifying constraints enforces the allowed microstates in the ensemble, selecting only the states compatible with a lab measurement. If for a system we impose the total number of particles (N) to be fixed, if the volume (V) of the sample cannot change, and if the total energy (E) is kept constant, the representation is the microcanonical ensemble (NVE). The classical ensemble probability density for a system in equilibrium can be written as (3) :

$$\rho^{ens}_{NVE}(\Gamma) = \frac{1}{\Omega_{N,V,E}} \cdot \delta\left(H(\Gamma) - E\right) \tag{1.2}$$

with δ selecting those phase space configurations having the imposed E energy. For a classical (N, V, E) indistinguishable, single component system the total number of microstates in the system's ensemble is counted via integrals over the phase space:

$$\Omega_{NVE} = \frac{1}{N!h^{3N}} \cdot \int_E d\Gamma \delta \left(H\left(\Gamma \right) - E \right) \tag{1.3}$$

with h Planck‘s constant.

The density of states in microcanonical ensemble is homogenous over the constant energy surface . The ensemble probability density of states ρ_{NVE}^{eq} for a system in equilibrium is independent of time (stationary). (3, 4)The ensemble average of A(Γ) property of a system, is calculated as:

$$\langle A\left(\Gamma\right) \rangle = \int A\left(\Gamma\right) \cdot \rho_{NVE}^{eq} \tag{1.4}$$

The canonical ensemble (NVT) with fixed total number of particles (N), with constant volume (V), and with fixed temperature (T) is another representation commonly used in both theoretical and simulation investigations. In this formalism the phase space probability density of states is proportional to (3):

$$\rho_{NVT}^{ens} = \frac{1}{Q(N,V,T)} \cdot \exp\left(-\frac{H\left(\Gamma\right)}{k_B T} \right) \tag{1.5}$$

where $Q(N, V, T)$ is the canonical partition function, T is the temperature of the system and k_B is Boltzmann‘s constant.

The Hamiltonian of the system depends on all N particle vector coordinates and on all N particle vector momenta composing the system, $H[p^N(t), r^N(t)]$.The Hamiltonian of a system is composed of a kinetic part K dependent only on momentum of the particles and a potential part U dependent on particles’ positions (5):

$$H(\Gamma) = K(p^N) + U(r^N) \tag{1.6}$$

For a one component, indistinguishible N particles system we can write the Q(N,V,T) partition function as a kinetic part and as a configurational interacting part(3):

$$Q(N,V,T)=\frac{1}{N!h^{3N}}\int e^{-\beta K(p^N)}dp_1dp_2...dp_N\int e^{-\beta U(r^N)}dr_1dr_2...dr_N \tag{1.7}$$

with $\beta = 1/k_BT$. The kinetic energy term $K(p^N)$ is defined as:

$$K(p^N)=\frac{1}{2m}\sum_{i=1}^{N}\left(p_{ix}^2+p_{iy}^2+p_{iz}^2\right) \tag{1.8}$$

The integral over momenta can be evaluated analytically:

$$\int e^{-\beta K(p^N)}dp_1dp_2...dp_N=\left(\frac{2\pi m}{\beta}\right)^{3N/2} \tag{1.9}$$

And as such equation 1.7 classical canonical partition function ($Q(N,V,T)$) becomes:

$$Q(N,V,T)=\frac{1}{N!}\frac{1}{\Lambda(T)^{3N}}\int e^{-\beta U(r^N)}dr_1dr_2...dr_N \tag{1.10}$$

The term $\Lambda(T)$ is the de Broglie thermal wavelength:

$$\Lambda(T)=\left(\frac{\beta h^2}{2\pi m}\right)^{1/2} \tag{1.11}$$

Only classical simulations are introduced in this work. A simple test for the validity of the classical behavior of particle assumption is the temperature de Broglie $\Lambda(T)$ wavelength. According to this criteria, if $\Lambda(T)$ is considerably less than particles near-neighbor inter-separation then the classical approximation holds. From equation 1.11 we see that such is the case for heavier particle systems and at higher temperatures (T).

The evolution of the N particle system through phase space follows Hamilton‘s equation of motion:

$$\frac{\partial H}{\partial p_j} = \frac{p_j}{m_j} = \dot{r_j} \tag{1.12}$$

and

$$\frac{\partial H}{\partial r_j} = -\dot{p_j} \tag{1.13}$$

with j referring to the jth particle in the system.

MD simulations evaluate time-averaged physical observables over phase space probability density functions $\rho(r^N, p^N)$. During such investigations, a collection of microstates are sampled according to their equilibrium probability distribution. Macroscopic equilibrium properties determined in lab measurements are equated to simulation-determined values as:

$$A^{exp} = \langle A \rangle^{ens} = \langle A(t) \rangle^{eq} = \frac{1}{t_{md}} \int_{t=0}^{t_{md}} dt' A\left(\Gamma(t)\right) \rho_{NVE}^{eq}(\Gamma) \tag{1.14}$$

Dynamic properties evaluated in MD simulation are determined from constructing spatial and temporal correlation functions. Example properties evaluated in this manner include transport coefficients, relaxation rates, and absorption spectra. (3, 4, 6, 7)

If a system property is defined in terms of a single variable A tracked during simulation, the non-normalized time correlation function of fluctuations in the system is an autocorrelation function of the type:

$$C_{AA}(\tau) = \frac{1}{t_{md}} \int_{0}^{t_{md}} dt A(t) A(\tau + t) \tag{1.15}$$

Time correlation functions are used to calculate transport coefficients. Such estimations are permitted due to the remarkable linear response theory and the fluctuation dissipation theorem of time-dependent statistical mechanics.(4, 8) This formalism shows that under a weak (needed for linear approximation) applied energy perturbation that couples with a specific property A of a system (can be any system property), the timescale of return of property $A(t)$ to equilibrium values $\langle A \rangle_{eq}$ is proportional to the timescale determined from equilibrium time correlation function of fluctuations in A.

1.2 Selected Details of Molecular Dynamics (MD) Simulation

Molecular dynamics (MD) simulations provide structural features, thermodynamic equilibrium characterizations, and dynamical properties of various states of matter.(4) Scientific questions explored in MD simulation include the structure and dynamics of simple and complex fluids, phase diagrams, and topological defects distributions such as vacancies and interstitials, small size metal cluster lowest energy characterizations, and biologically relevant macromolecules and polymers structural and conformation changes. The first MD simulation evaluated a solid-liquid phase transition of a hard sphere system and was reported in 1957 by Alder and Wainwright (9). A next classic pioneer MD simulation paper is Rahman's paper from 1964 (10). He simulated 864 atom particles of liquid Ar. The analysis consists of determining the diffusion constant from velocity autocorrelation functions and the simulation liquid Ar structure. The diffusion constant calculation holds a special historic value, as is the first simulation autocorrelation function report.

The initial MD configuration of a system $r^N(0)$ is chosen to match the resolution of an X-ray structure. In the context of MD simulation Hamilton's equation can be written in Newton's formulation as (5):

$$\frac{\partial H}{\partial r_i} = -m_i \ddot{r}_i = \frac{\partial U}{\partial r_i} = -f_i \tag{1.16}$$

with f_i the total force on particle i, and m_i is the mass particle. The propagation of a system's coordinate and momentum in phase space by Newtons equation of motion corresponds to generating ρ_{NVE} states in the microcanonical ensemble. Force calculation in molecular dynamics simulations requires a potential energy function that is often approximated as a sum of bonded and non-bonded terms, with the non-bonded interactions often simplified to a sum of pairwise interactions.

For a system of N particles the force acting on particle i is evaluated as: (1)

$$f_i = m_i \ddot{r}_i = \sum_{i=1, i \neq j}^{N} f_{ij} \tag{1.17}$$

The force between pairs of particles f_{ij} is evaluated as the gradient of the potential energy functions $u(r)$ describing the physical interaction between particles (equation 1.18).

$$f_{ij} = - \bigtriangledown u(r) \tag{1.18}$$

From system to system investigated in MD simulation, the potential functions (the force-field) vary greatly in complexity. For polyatomic molecules with complex internal structure such as lipid molecules, a complicated functional form potential is typically required.

The interactions separated into two parts as bonded potentials and non-bonded potentials can be written as :

$$u(r^N) = u_{bonded}(r^N) + u_{nonbonded}(r^N) \tag{1.19}$$

The bonded potential $u_{bonded}(r^N)$ typically includes a bonded stretching potential between pairs of atoms having a chemical bond, a bond angle potential, and a dihedral angle interaction. If the atoms need be restrained to a specific chiral conformation or a specific configuration, an improper dihedral potential is also used. A typical functional form of such a potential is, respectively (5):

$$u_{bonded}(r^N) = \sum_{n=1}^{N_b} k_{b_n}(b-b_o)^2+\sum_{n=1}^{N_\theta} k_{\theta_n}(\theta-\theta_o)^2+\sum_{n=1}^{N_\phi} k_{\phi_n}\left[1+cos(m\phi-\phi_o)\right]+\sum_{n=1}^{N_\psi} k_{\psi_n}(\psi-\psi_o)^2 \tag{1.20}$$

The indices of summations $N_{(b\theta\phi\psi)}$ represent the number of bonds and angles that need be included and are determined by the size of the system. The set of constants $\{k_{b_n}, k_{\theta_n}, k_{\phi_n}, k_{\psi_n}, b_o, \theta_o, \phi_o, \psi_o\}$ is the force-field parameter representation employed in an MD calculation. Typically, these constants are developed to reproduce experimentally determined structural and energetic properties (e.g. data from X-ray scattering, NMR order parameter, energy of vibration modes from spectroscopy) and/or ab initio calculations output.

The non-bonded potential $u_{non-bonded}(r^n)$ is typically the Lennard-Jones (LJ) potential and a point charge (q_i, q_j) Coulomb electrostatic interaction:

$$u_{non-bonded}(r^N) = \sum_{(i,j)}^{n_{pairs}} \left\{ 4\varepsilon_{ij}\left[\left(\frac{\sigma}{r_{ij}}\right)^{12} - \left(\frac{\sigma}{r_{ij}}\right)^{6}\right] + \frac{q_i q_j}{r_{ij}} \right\} \tag{1.21}$$

with ϵ describing the strength of interaction and σ setting the distance at which the potential between two particles is zero.

In order to match properties evaluated in experiments, improvements to existing sets of force-fields parameters and modifications of functional forms of potential functions are implemented. For a discussion on lipid force-field development see reference 11.

Some equilibrium properties easily accessible in MD simulations include temperature, energies (kinetic, total, potential), heat capacities, pressures, and structural densities. Analogous to statistical mechanics calculations all other system properties can be derived from manipulating the MD basic output in the appropriate ensemble.

An example of a transport coefficient often evaluated in MD simulation is the shear viscosity. A shear viscosity coefficient calculation amounts to integrating over time autocorrelation functions constructed from trajectory averaged off-diagonal elements of the pressure tensor, $\sigma_{\alpha\beta}$, with $\alpha\beta = (xy, xz, yz)$ the Cartesian coordinates in the system:

$$\eta = \frac{V}{k_B T} \int_0^\infty \langle \sigma_{\alpha\beta}(0) \sigma_{\alpha\beta}(t) \rangle \tag{1.22}$$

with V the volume of the system and $k_B T$ the thermal energy.

The elements of pressure tensor $\sigma_{\alpha\beta}$ in simulation are evaluated as:

$$\sigma_{\alpha\beta} = \frac{1}{V} \left[\sum_j m_j v_{j\alpha} v_{j\beta} + \frac{1}{2} \sum_{i \neq j} r_{ij\alpha} f_{ij\beta} \right] \tag{1.23}$$

with j looping over all particle, m_j the mass of the particle, $v_{j\alpha(\beta)}$ the particle velocity in the specified direction, $r_{ij\alpha}$ is the inter-particle distance along α, and $f_{ij\beta}$ the paiwise force acting in a β orthogonal direction.

We also mention that in spite of great progress in recent years in parallelizing the MD force calculation loop (the most expensive step), molecular dynamics (MD) simulations suffer from limitations.(12) Cellular processes sustain life in a highly complex and dynamic manner. It involves specific atom compositions, countless reactions, macromolecules folded and stored in a very efficient way, highly specialized organelle machineries, and intricate compartmentalization mechanisms. Bonding preferences during conformational changes of bio-macromolecules such as proteins and DNA need be investigated with an atomic level of resolution. The time scale for significant molecule folding is significantly longer than those routinely samples in simulations (for atomistic systems, typical computing hardware enables calculations of low hundreds of ns at best). The size of an organelle is billions of atoms and such a calculation is too expensive as well. There is also the additional complication of each molecule type having a large number of variants (precise structures of thousands of lipids and thousands of membrane proteins are currently known (13, 14)). This composition is also dynamic and non-equilibrium like. Only simple models can be implemented in simulation. In addition the force-field parameter sets of ions and charged systems are known to often fail reproduce the physics of such interactions accurately.

1.3 Metropolis Monte-Carlo (MMC) Sampling

If only equilibrium system properties are needed, a computationally efficient way to sample the configuration space is the Monte-Carlo (MC) technique introduced by Metropolis and coworkers in 1953. (15) Monte-Carlo methods implement stochastic strides in the configuration-space (r^N) according to well-specified rules. The natural ensemble of Monte-Carlo calculations is the canonical (NVT) ensemble. Each configuration i corresponding to E_i energy in converged MC ensemble has a probability proportional to its statistical weight in an NVT equilibrium ensemble(16) :

$$\rho(i)^{eq} \propto \exp(-\frac{E_i}{k_B T}) \tag{1.24}$$

A robust MC algorithm must satisfy microscopic reversibility or the detailed balance condition. For a system in equilibrium, this requirement is fulfilled if the resulting rate of MC transition from any state i to state j is the same as the rate of the reverse transition, going from any state j to state i(4). The total probability flux is then:

$$\pi_{ij} \cdot \rho(i)^{eq} = \pi_{ji} \cdot \rho(j)^{eq} \tag{1.25}$$

Here π_{ij} refers to the conditional transition probability between states i and j or:

$$\pi_{ij} = \alpha_{ij} \times acc(i - j) \tag{1.26}$$

And equation 1.25 becomes:

$$\rho(i) \times \alpha_{ij} \times acc(i - j) = \rho(j) \times \alpha_{ji} \times acc(j - i) \tag{1.27}$$

with $\rho(i)$ term denotes the probability of state i distributed in a NVT ensemble, α_{ij} the probability that given an original state i an attempt will be made to change the state to j, and finally $acc(i-j)$, the probability of accepting the move from state i to state j. Metropolis Monte-Carlo further assumes that the frequency of attempting to reach state j from state i is the same as the frequency of aiming to reach state i from state j (4, 17):

$$\alpha_{ij} = \alpha_{ji} \tag{1.28}$$

The acceptance probability of new configurations j from current configurations i that also satisfies equation 1.28 then reduces to:

$$\frac{acc(i-j)}{acc(j-i)} = \frac{\rho_i^{eq}}{\rho_j^{eq}} = \exp(-\frac{E_j - E_i}{k_B T}) \tag{1.29}$$

The strides in the configurational space according to equation 1.29 must connect any two points in configurational space through a finite series of steps.

Dynamic system configurations and time dependent events such as diffusion of defects in solids are often characterized using Kinetic Monte-Carlo algorithms (KMC)(18, 19).

Processes that can be evaluated via Kinetic Monte-Carlo techniques correspond to Poisson distributed events where the time dependent rates of transitions between states of interest are uncorrelated in time. In such an implementation the allowed transitions between states need be accounted for or defined prior to each Monte-Carlo move. The actual transition probabilities decisions are per unit time and the time intervals between attempting to reach states of interest are rigorously tracked. Within KMC the rates of transitions between dynamic states of the system are also required to satisfy a detailed balance condition.

References

[1] D.C. Rapaport. *The art of molecular dynamics simulation.* Cambridge Unviersity Press, Cambridge, U.K., 2 edition, 2004. 1, 7

[2] D.J. Phillies, George. *Elementary lectures in statistical mechanics.* Springer-Verlag, New York, 2000. 2

[3] M. P. Allen and D. J. Tildesley. *Computer Simulation of Liquids.* Oxford University Press, New York, 1987. 2, 3, 5

[4] Daan Frenkel and Smit Berend. *Understanding Moelcular Simulation: From Algorithms to Simulations*, volume 1. Academic Press, London, 2002. 3, 5, 6, 10, 11

[5] E. Maginn and J.R. Elliott. Historical perspective and current outlook for molecular dynamics as a chemical engineering tool. *Ind. Eng. Chem. Res.*, 49:3059–3078, 2010. 3, 6, 7

[6] Hans C. Anderson. *Time-Dependent Statistical Mechanics 9. Linear response in classical statistical mechanics.* Oxford University, lecture notes., 2009. 5

[7] D. A. McQuarrie. *Statistical Mechnics.* University Science Books, Sausalito, CA, 2000. 5

[8] R. Kubo. The fluctuation-dissipation theorem. *Reports on Progress in Physics*, 29(1):255, 1966. 5

[9] B.J. Alder and T.E. Wainwright. Phase transition for a hard sphere system. *J. Chem. Phys.*, 27:1208–1209, 1957. 6

[10] A. Rahman. Correlations in the motion of atoms in liquid argon. *Phys. Rev.*, 136:A405–A411, 1964. 6

[11] Kenny B. Lipkowitz. *Reviews in Computational Chemistry*, volume 27. John Wiley and Sons, New Jersey, 2011.

[12] Ron O. Dror, Robert M. Dirks, J.P. Grossman, Huafeng Xu, and David E. Shaw. Biomolecular simulation: A computational microscope for molecular biology. *Annual Review of Biophysics*, 41(1):429–452, 2012. 9

[13] Eoin Fahy, Shankar Subramaniam, Robert C. Murphy, Masahiro Nishijima, Christian R. H. Raetz, Takao Shimizu, Friedrich Spener, Gerrit van Meer, Michael J. O. Wakelam, and Edward A. Dennis. Update of the lipid maps comprehensive classification system for lipids. *Journal of Lipid Research*, 50(Supplement):S9–S14, 2009. 9

[14] P. Raman, V. Cherezov, and M. Caffrey. The membrane protein data bank. *Cellular and Molecular Life Sciences*, 63(1):36–51, 2006. 9

[15] Nicholas Metropolis, Arianna W. Rosenbluth, Marshall N. Rosenbluth, Augusta H. Teller, and Edward Teller. Equation of state calculations by fast computing machines. *The Journal of Chemical Physics*, 21(6):1087–1092, 1953. 10

[16] D.N. Theodorou. Progress and outlook in monte-carlo simulations. *Ind. Eng. Chem. Res.*, 49:3047–3058, 2010. 10

[17] M. Rubinstein and R. Colby. *Polymer Physics*. Oxford University Press Inc., New York, 2003. 11

[18] W M Young and E W Elcock. Monte carlo studies of vacancy migration in binary ordered alloys: I. *Proceedings of the Physical Society*, 89(3):735, 1966. 11

[19] P. A. Flinn and G. M. McManus. Monte carlo calculation of the order-disorder transformation in the body-centered cubic lattice. *Phys. Rev.*, 124:54–59, 1961. 11

2

An Introduction to Self-assembled Responsive Biomaterials

2.1 Protein Networks in Experiments

A peptide hydrogel is a high molecular weight polymer network structure held together by permanent peptide bonds and physical bonds and it can absorb large amounts of water.

Synthesis strategies, properties, and typical uses of peptide-based biomaterials have been explored in several recent review articles and the references therein. (1–5) The physical bonds are reversible and include interactions of the type electrostatic interactions due to charged species, directional hydrogen bonding, and Van-der-Waals interactions. The chemical structural units used in peptide-based materials synthesis are the 20 natural occurring amino acids. Another physical interaction dictated by the identity of amino-acid used also include π-stacking due to aromatic amino-acids.

The material properties resulting from 3D peptide self-assembly are interesting as the reversibility of the bond and thus the strength of the material can be externally controlled in several ways such as introducing a junction-linker bond competing specie (6), changing the temperature of the system(7) altering the pH (8) , changing the ionic strength of the solution (9), changing the solvent polarity, introducing enzyme cleaving sensitive sequences or oxidative species, and also UV/vis light exposure.(1, 2, 4) Altering the network properties in an external manner render this class of biomaterials, responsive materials.

The identity of amino acids used in synthesis of peptide-based materials determines the type of resulting response(1). The basic amino-acids and the acidic amino-acids lead to additional Coulombic temporary interactions that can be further tuned via a change in pH and/or solution ionic strength. Hydrophobic amino-acids and amino acids capable to hydrogen bond offer the possibility to alter the resulting material by both changing the temperature and also the solvent polarity.

Typically, each monomer components undergoing self-assembly in a peptide based biomaterial consist of one or several permanent tandem peptide sequences. Such sequences may resemble random coil structure or well-defined protein secondary structure of the type alpha helices, leucine-zipper domains, beta-hairpins, coiled-coil domains, and beta-sheets.(1)The self-assembly resulting from mixing such components may take the form of nanometer size fiber like morphologies, tubes, micelle like structures, and reversible polymer networks.

This thesis models dynamic properties of polypeptide systems with topology resembling the classical picture of polymer network structure.

There is great interest to employ peptide biomaterials engineered from naturally occurring peptides in biomedical applications as delivery systems, biosensing units, and tissue engineering injectable scafolds.(2) Peptide-based materials may also serve as surface coating modifications or in applications such as nanowire templating technologies.(2) Recognition events between ligand and cell receptors and between enzyme actives sites for cell native ligand binding, drug molecule delivery, and molecular sensing probes can be easily designed from further decorating the peptide material monomer components with appropriate functional units(5).

A range of experimental techniques is needed to characterize each newly developed peptide hydrogel. Monomer folding behavior is determined from dynamic light scattering experiments (DLS) and reported as hydrodynamic radius (R_H) or radius of gyration (R_G). The monomer protein secondary structure is analyzed via techniques such as circular dichroism (CD) spectrometry. Multi-angle static light scattering measurements (Zimm plot investigations), electrophoretic gels, and FRET experiments are employed to show preferred number and modes of alignments of linker-junction interactions.(2, 8, 9) The kinetic constants and thermodyamic behavior of linker-junction monomer associations are studied via surface plasmon resonance (SPR) and isothermal titration calorimetry (ITC) (9–11).

Biological micro environmental factors that typically affect protein folding and function such as changes in temperature, pH, and ionic strength can also affect mechanical properties of peptide hydrogels. Assembled peptide based biomaterials need function in complex environments. While in some applications softer materials that can easily flow to target sites when injected or can take on the shape of a micro cavity are required, in other instances such as tissue engineering investigations, more robust hydrogels are desired, with an ability to support stress.

The strength of the peptide biomaterials is evaluated in rheological measurements and also in its modern form microrhelogy(12–14) as the plateau storage (elastic) modulus (G'). The stress relaxation profile is often the Maxwellian viscoelastic behavior, a simple exponential stress decay. Typically values measured for (G' of reversible protein networks from experiments are in the 100 Pa-1000 Pa range (7, 8). External factors found to affect the elastic modulus of reversible networks include linker length, temperature, and concentration, with higher equilibrium storage modulus for networks implementing longer linkers, higher concentration, and lower temperatures.(7, 15, 16) The relaxation time (τ_{shear}) was also measured during such investigations and found strongly correlated with the inverse linker-junction kinetic dissociation constant (k_{off}).

The physical theory used to describe the elasticity of reversible protein networks is called "The Transient Network Theory"(22). According to this theory the magnitude of G' is directly proportional to the network number density of chains (ρ_{chains}) capable to support stress and to the energy stored in each linker ($G' = k_B T \rho_{chains}$). Chains or linkers involved in binding pairs of junctions each having at least two other bonds (Scanlan (17) and Case (18) (SC) criterion for defining an elastic effective chain) are considered to have an ability to support stress. Reversible protein networks however are responsive to external stimuli of the type mentioned above and these factors can greatly affect the density of reacted groups that in turn determine the number of linker-junction bonds. As such the network composition on microscropic scale can vary significantly.

Even under optimized conditions to have the greatest number of junction-linker bonds possible, the real peptide networks that result are imperfect systems and not all linkers added during synthesis are able to support mechanical stress. For rheology measurements purposes, the re-normalization of chain density in networks with loops is implemented as to lower the storage modulus of hydrogels by an amount proportional to the fraction of looped linkers. (8, 16, 19) Linkers with unreacted ends must similarly be disregarded.

For practical applications such as controlled delivery and release, in addition to strength of hydrogels, the degradability of peptide networks or the breakdown of a percolated network is also of interest. In experiments, the rate of degradation of peptide based hydrogels has been explored by Tirrell et al.(20). A peptide network begins to loose its mass when simultaneously subsets of junctions/linkers lose all the bonding to the parent network structure. For this to happen it is required that the association kinetic constant (k_{assoc}) is slow and the separated fragments diffuse away without having a chance to rejoin the parent network.The rate of erosion was found to correlate with the presence of loops in the system. When loops are present, each junction on average is attached to the parent network by fewer bonds and network fragments are able to disengage sooner.

Individual pairs of junctions in percolated networks may be linked a single time or multiple times. In protein networks, the multiple junctions pairing effect was hypothesized and assumed negligible.(9) At the same added linker density, experimental storage modulus values characterizing the strength of materials to correspond to number of effective linkers in the system, currently do not distinguish between linkers serving to bind pairs of junctions multiple times. Simulation work can easily access resulting multiple junction pair fractions with functional form of interaction protential.

Correlating the dynamic signatures of reversible networks with the microscopic variation in the modes of junction-linker bonding such as paired vs. linear and/or in the presence of topological defects such as loops and stoichiometric mismatch is important in elucidating the equilibrium dynamics of protein network systems.

Although a far less explored area of protein networks dynamics and elasticity, the behavior of protein hydrogels in non-equilibrium regimes has also been described. Peptide networks have been previously subjected to creep test measurements(8) and the magnitude of strains supported with respect to applied external stimuli known to influence the hydrogel strength have been reported. In a more recent study reversible peptide networks subjected to high applied strains also uncovered an yielding regime due to a shear-banding mechanism.(15) Upon hydrogel injection, $\sim$ three times storage modulus shear thinning is calculated followed by a nearly full strength material recovery thus such materials can also have excellent self-healing capabilities. The high gel recovery rate was explained as due to having the very high strain regions localized to only pockets of percolated protein network. Shear-thickening behaviors is also possible to occur for peptide hydrogels in highly non-equilibrium regimes. Longer lifetimes with applied force for proteins functioning to create the junction-linker bond have been previously reported (21).

2.2 Background Elasticity Theory and Simulations

The general features of a reversible polymer network in elasticity theory include junction points and linkers as well as defects of the type dangling ends, loops, and other types of topological entanglements (i.e. knots). The majority of mass of such networks is concentrated in the junction points.

The onset of the efforts to develop a simple theory that shows how molecular rearrangements relate to the dynamic properties of reversible networks dates back to 1946 to work published by Tobolsky (22). His analysis considered reversible networks, free of entanglements, at equilibrium. Making use of the recently published kinetic theory of elasticity (23) as applied to polymers, Tobolsky argued that in a reversible network, if the stress that results from applying an instantaneous perturbation can be written as a sum of the stresses associated with each bond in the system, then each disconnecting bond event will relax the stored stress attributed to that bond. Because work is done upon the system during the applied perturbation, according to simple thermodynamic principles, the new bond that replaces the disconnected bond, must be in a relaxed state. If the number of bonds in the system is kept constant and if the stress can only relax via the disconnecting events, then the stress relaxation rate follows a simple exponential. Hence, in Tobolsky's theory, the bond-disconnecting event dictates the dynamic behavior of the networks and the viscosity is the constant that relates the exponential stress decay to the remaining stress in the system. Throughout the literature Tobolsky's theory is commonly referred to as the "transient network theory". This theory it is often used to explain experimentally found magnitude of storage modulus (G') and the relaxation time (τ_{shear}) of assembled protein networks.

Several assumptions are present in the transient network theory. The network is homogenous in structure and incompressible, the junction points move affinely with applied deformation, and the stress is uniformly transmitted across lengthscales. Also, the linker lengths follow a Gaussian distribution, the fluctuations in junction points do not contribute to modifying the stress stored in the connecting linkers, and the linkers connect to the parent network at a single point. Furthermore, the Green and Tobolsky probability of breaking the linker-junction bond is assumed independent of the state of the linker stretching. The relaxation of stress stored in a linker occurs independently of all other chains. Also, once a linker is relaxed due to a disconnecting event upon re-attaching to the network it does not contribute to the system's stress.

Other scientists incorporated additional microscopic details and instances into their models and showed how the dynamic properties of reversible networks changed compared to this simple model proposed by Green and Tobolsky.

Earlier theories investigated the reversible network relaxation associated with shear deformation of networks under stationary flows. In terms of microscopic parameters implemented to affect the observed behaviors, Lodge's theory (24) assumes an equal probability of breaking and re-forming chains the junction points with the stress at any given time dependent on flow history. In Kaye's work(25) the bond-disconnecting event is stress dependent. Yammamoto's theory (26, 27) considered that the bond breaking event should dependent on both end-to-end linker elongation and linker contour length. The linkers needn't be Gaussian chains. The first reference to attempting to introducing junction multiplicity as a parameter when discussing the relaxation of reversible networks was given by Lodge (28) when presenting a modified version of Kaye's theory.

The study of Wintjes et al. (29), related to the Lodge model relates the dynamic properties of transient networks to the degree of intermolecular bonding and kinetic constants of forming and breaking the bonds. This work is related to our own investigations in that local network connectivity is explicitly considered.

The network is composed of *connected* springs (equivalent to linkers having reacted ends) decorated with up to eight connected or free sticky points (binding sites) per chain. The total stress in the network is the sum of its Gaussian distributed connected springs. The chains are categorized into *active* and *inactive* chains based on their ability to support stress. The mechanism of stress relaxation consists of reptation like relaxation and simultaneous or individual sticky points disconnecting from their bonding place. The number of active chains is determined from both integrating over possible spatial configurations of individual chains and from following the kinetics of formation and annihilations of active chains.

The transition between free states and bound states required an activation energy that follows an Arrhenius type equation with the rate dependent on an activation energy barrier of breaking and reforming the bonds, as to reflect the chemistry of interacting groups. Raising this activation energy corresponded to longer relaxation times and wider plateau regions. The concentration/fraction of active chains were also found dependent on the kinetic constant of reversible bond. The stress relaxation rates are also sensitive to having an energy difference between the energy of breaking a bond and to the energy of forming a new bond. If there is a high energy barrier to breaking the bond but a low energy barrier to forming a bond the disconnecting events are rare events and the stress will not relax for a long time. The plateau moduli curves have high values and wide plateaus regions.

A single relaxation time corresponding to a single exponential decay is observed for having low activation energy barriers and as much as two stickers per chain. The relaxation time of a chain segment should reflect the summation over all rate constants associated with relaxing its partial domains.

The shear stress plateau in the system is from summing over number of active chains in the system. The number N of sticky points per chain influenced both the magnitude of shear modulus and the number of plateau regions. The number of plateaus that result is N/2 for a system that has an even number of stickers per chain and (N-1)/2 plateaus for a system whose chains have an odd number of stickers. A higher number of stickers lead to higher magnitude shear modulus plateaus values thus making for stronger materials. The shear relaxation time is also increaded in these systems.

In a later study (30) for a polymer chains with several sticky points per chain Jongschaap isolated situations where the disconnecting events do not necessarily contribute to the overall relaxation of the system. If the sticker where the dissociation process occurs is tightly neighbored only by stickers that are yet to dissociate, such as an intramolecular type bonding instance, then these events belongs to a time scale that does not necessarily contribute to the macroscopic stress relaxation profile of the system. In the same study two types of stickers with different binding abilities were also explored.

The microscopic parameters considered in the theory developed by Tanaka and Edwards (31, 32) the rate at which the bonds disconnect themselves from the bonding place and the rate at which the bonds successfully recombine to a new place in the systems with the former dependent on absolute magnitude of end-to-end distance due to tension in the chain, temperature, and linker molecular weight. The equilibrium number of active chains also considers a rate of new bond formation that explicitly includes an energy barrier to forming new chains. The stress relaxation modulus decrease with temperature is postulated due to the thermal motion increasing the frequency of bond dissociation events. Only a weak dependence is observed with increasing the contour linker length. Explicit formula for the complex viscosity typically determined in rheology experiments is also presented. The Green-Tobolsky limit of this equation is also shown in the frequency domain, with $G'(w)$ explicitly dependent on the constant rate of bond dissociation event and the population of chains at equilibrium.

Tanaka and Edwards' work also transitions towards investigating non-equilibrium, non-linear effects such as shear thinning by considering a end-to-end distance dependent probability function describing the disconnecting events. In polymer theory, the resulting elongation of a polymer chain under strong non-linear stretching and the force needed to exert the elongation is typically explained via the Langevian function(33, 34). The probability of the disconnecting event explicitly in Tanaka's work considers the tension in the chain along with a coupling constant that controls the magnitude of rate of dissociation at that elongation.(35) The lifetimes of the bonding points in the network are predicted to monotonically decrease when increasing the applied shear. In other studies Tanaka and co-workers (35–37) investigated how junction multiplicity, linker length, and intramolecular re-arrangements such as loops formation influence the percolation limit. The evolution of number of linkers capable to support stress in this limit is also investigated.

Cates' work (38, 39) is related to reptation theory and it is more complex compared to the transient network theory because it considers reversible self-assembly with the possibility of chains also entangling.

Dynamics and elasticity of both entangled and unentangled systems were considerd by Rubinstein and co-workers, both near the percolation regimes and also when the networks are fully formed. (40–43) We briefly mention developments for unentangled, reversible, fully formed networks. The reacting groups are 'sticky points' and a large number (up to 20) were considered located on the same chain at equidistant positions. The polymer mass between the sticky points on the same chain was referred to as 'strands'. The fraction of recombination events by sticky ends of strands that result in the dangling end finding the old partner is discounted as means of stress relaxation in the system. Two time scales are considered to control the material dynamics of the networks, the relaxation time of the strand and the relaxation time of the chain. Two plateau moduli are discussed, G_0 and G_1 with $G_0 > G_1$. The shear modulus plateau

G_0 is linear in density of strands and the energy stored per strand. This modulus corresponds to the elastic limit of a traditional rubber like network. The magnitude of G_1 on the other hand is linear in number of chains. The shear viscosity of the system is the product of G_1 and the relaxation time of the chain.

Previously the dynamic properties of reversible networks have also been studied in simulations.(16, 44–46) Please also see references of papers cited end of previous sentence. Here we briefly explore molecular dynamics/Monte-Carlo hybrid simulation work published by Hoy and Fredrickson(46) where the microscopic reversible network structure resembles the classical polymer network picture and it is closest in that regard to our own investigation. (46) Bond breaking and bond recombination is achieved via Monte-Carlo moves. The relationship between strength of interaction at the sticky points was changed from very weak when no network structure percolates up to four times above the gel transition. Thermodynamic equilibrium constants were calculated for each magnitude of interaction energy considered. One unique feature of this simulation study is that the time scales are manipulated in such a manner that under some instances the bond breaking events and the bond forming events become correlated. As such the bond recombination event is both kinetically controlled and diffusion controlled. The lifetimes of the sticky points were separated into a *bare* lifetime of a bond that corresponds to kinetics of disassociation and an *effective* lifetime of a bond where separated stickers diffuse away by connecting to a new partner and in doing so the old bond relaxes. For a percolated network, a relationship is established between these important system relaxation time scales and the probabilities of bond re-combinations due to kinetic considerations or due to a diffusion contribution.

Synthesized reversible protein networks need function in highly non-equilibrium conditions such as they need to flow when injected or need be strong materials that can support mechanical stress when employed in applications such as scaffolds in tissue engineering. We conclude this section by mentioning lessons learned from both experiment and theory of telechelic reversible networks pertaining to non-equilibrium, non-linear regime.

This class of reversible networks differs from protein networks that a considerably higher junction multiplicity is achieved in experiment. Also the microscopic descriptions of such assembly resemble flower-like micelles with arms capable to inter-bond reversibly into networks rather than having a rubber like polymer network structure. Their equilibrium dynamic behavior has been the object of numerous experimental and theoretical studies and the trends observed were compared to transient network theory predictions not so unlike the dynamic and elastic behavior of reversible peptide networks.

Under applied shear stress beyond the linear regime, Jenkins's work (47) on the hydrophobic ethoxylated urethane (HEUR) systems observed a shear-thickening viscosity regime ($\sim 70\%$ increase) at lower shearing rates. Three shear-thinning viscosity regimes were also observed with increasing the non-linear shearing rates. The shear-thickening viscosity was explained as shear-induced new junction points formation, as loops to active linkers non-equilibrium prompted rearrangements, and as an increase in the relaxation times of the system due to the reduction in number of superbridges. Interestingly, the first two shear-thinning regions had a storage modulus similar to the shear-thickening region but accelerated, distinct shear relaxation times that lowered the shearing viscosity. The authors concluded that the topology of the network is thus mostly unchanged by the applied stress. The junctions' lifetimes were however greatly affected by the shear deformation. The sharp change in the viscosity for the last shear-thinning region is believed characteristic of network fragmentations.

Previously, the non-linear reversible network dynamic behavior was also interpreted as strictly resulting from shear-induced non-affine extensions of the linkers that lead to highly strained networks. Berret et al.'s work (48) on the F-HEUR systems consisted of step-strains experiments with applied strains in the 0.01-3.0 regime. The onset of the non-linear regime was identified for applied step strains larger than 0.4 and it was followed by a strain hardening region under conditions of strain smaller than ∼2. The strain hardening region was characterized by a strong increase in the storage modulus attributed to stiffening of the linkers themselves due to a non-linear stretching as well as a decrease in the relaxation time with larger applied strains.

The strain hardening phenomenon due to non-affine chain deformations was also studied by Cooper et al. in hydrophobically capped poly-(ethylene oxide) networks via applied shear experiments similar to those done by Jenkins. In this study it was also shown that increasing a systems concentration leads to mildly higher non-linear viscosity as well as lower onsets for the shear-thickening phenomena. Higher temperatures lowered the non-linear viscosity and delayed the onset of the shear-thickening viscosity. Roughly tripling the linkers molecular weights resulted in the absence of the shear-thickening region. This feature was attributed to a shorter final non-equilibrium linker stretching.

Among the theoretical studies aiming to explain the non-linear behavior of reversible networks, the Marruci model (49, 50), the Tanaka/Edward theory mentioned previously, and the van den Brule/Hoogerbrugge simulation work (51) are the most popular. The framework of Marruci's model is similar to Tanaka's work but conceptually different in that the chains are considered to re-attach to the network in strained states. His derivations explain the experimentally observed shear-thickening regions as strongly correlated to the existence of shear-induced chain stretching. The shear-thickening rate changed with the end-to-end distance independently of the junction-linker binding statistics. The increase in viscosity is explained by additional energy stored in the deformed linkers and believed dependent on the binding and the unbinding events as well as on the applied shear rates (higher initial shear rates believed to increases stored energy). The probability of formation of the new elastic chains is linked to the ability of the dangling chains to explore its environment and end-to-end distance dependent. The probability of a linker disengaging from the network is dependent on the chain extension and it has probability 1 when the linker is fully extended. The spectra of the relaxation times reflects the relationships between the degree of initial linker stretching, the effect of partial chain relaxation, and the number of binding/unbinding events. Van Den Brule's Brownian dynamics simulations derived theory added an additional dimension to explaining the shear-thickening behaviors in reversible networks as the simulations indicate that under non-linear shear flow, the probability of junction point formations tend to be higher for longer linkers.

Some of the limitations of the Marruci's model are shown in Mewis' work (52). The onset of the non-linearity features is observed at much lower shear rates than predicted from the Marruci theory and believed to be caused by also changes in the relaxation times of the linkers.

It is also possible that with nonlinear applied forces, the end-to-end distance evolution lead to equilibrium similar terminal linker configurations but less gradual changes in some of the kinetic parameters that dictate the settling of the non-equilibrium behavior. The effects of varying the strength of associations at the junction points was further studied by Mckinley et al. (53) Finally, the non-linear dynamic behavior of systems with free chains and both inter-chain and intra-chain bonding capabilities was also explored previously and explained to correlate with a coagulation of linkers (54).

2.3 This Work

The existing simulation work cited above, such as Monte-Carlo (MC) type investigations, aims to identify likely topological network structures(16). Simulation work that considers network local connectivity (often lattice models) limits itself to establish or verify geometric or rigid percolation exponents. Simulation studies such as Hoy and Fredrickson' s MC/MD investigation (46) that evaluated the network percolation due to energy of interaction and also explored network dynamics are hard to find in literature.

In this simulation and theory work we conduct a systematic investigation of the relationship between local network connectivity and resulting rheological (elastic/dynamic) signatures of fully percolated reversible (protein) due to pre-imposed degrees of stoichiometric mismatch in mixing components.

Protein hydrogels in experiment most compatible with these studies are two component systems, more specifically divalent linkers terminated at both ends by peptide ligand sequences and junction components consisting of several ligand complimentary binding sites, all sites linked covalently as a single rigid unit. As a simulation model, a hybrid Monte-Carlo, Molecular Dynamics (MCMD) simulation model is constructed. The Monte-Carlo move reproduces the bond-rearrangement move that relaxes the stress in the system. The molecular dynamics (MD) segment of the trajectory relaxes the stress in the system thus creating uncorrelated bond breaking and bond forming events. The ensemble thermodynamic observables that lead to material properties such as viscosity calculations are determined from averages across the MCMD trajectory.

A fraction of looped linkers and specific modes of junction-junction bonding are also implemented. A distribution in linker lengths is incorporated. The stiffness of the linkers is changed. The number of ligand-junction interaction per junction component determines the valence of the network. The network topology is precisely considered in each instance and the valence is increased from three to nine. In simulation, the reversible network structural defects and topological details mentioned above are investigated separately and then in combination with one or all others.

A simple phenomenological theory is introduced and relates our various simulation cases findings. Explicit microscopic defect migration rates that lead to stress relaxation in all instances are presented. The material properties evaluated include the rate of stress relaxation and the shear relaxation time (τ_{shear}), and the plateau shear modulus G' (in this work G or G^0) determined in rheology experiments. Applicability to other regimes and systems such as close to network percolation threshold limit and telechelic networks respectively are also explored. Furthermore, the time-dependence of viscosity during gel "aging" is modeled as an approach to equilibrium through diffusion-limited annihilation of complementary unreacted groups.

References

[1] Robert J. Mart, Rachel D. Osborne, Molly M. Stevens, and Rein V. Ulijn. Peptide-based stimuli-responsive biomaterials. *Soft Matter*, 2(10):822–835, 2006. 14, 15

[2] Dominic Chow, Michelle L. Nunalee, Dong Woo Lim, Andrew J. Simnick, and Ashutosh Chilkoti. Peptide-based biopolymers in biomedicine and biotechnology. *Materials Science and Engineering: R: Reports*, 62(4):125–155, 2008. 15, 16

[3] Kristi S. Anseth, Andrew T. Metters, Stephanie J. Bryant, Penny J. Martens, Jennifer H. Elisseeff, and Christopher N. Bowman. In situ forming degradable networks and their application in tissue engineering and drug delivery. *Journal of Controlled Release*, 78(13):199–209, 2002.

[4] Constantinos Tsitsilianis. Responsive reversible hydrogels from associative ”smart” macromolecules. *Soft Matter*, 6(11):2372–2388, 2010. 15

[5] Rein V. Ulijn, Nurguse Bibi, Vineetha Jayawarna, Paul D. Thornton, Simon J. Todd, Robert J. Mart, Andrew M. Smith, and Julie E. Gough. Bioresponsive hydrogels. *Materials Today*, 10(4):40 – 48, 2007. 14, 16

[6] Shana Topp, V. Prasad, Gianguido C. Cianci, Eric R. Weeks, and Justin P. Gallivan. A genetic toolbox for creating reversible ca2+-sensitive materials. *Journal of the American Chemical Society*, 128(43):13994–13995, 2006. 15

[7] Helena Teles, Paulina J. Skrzeszewska, Marc W. T. Werten, Jasper van der Gucht, Gerrit Eggink, and Frits A. de Wolf. Influence of molecular size on gel-forming properties of telechelic collagen-inspired polymers. *Soft Matter*, 6(19):4681–4687, 2010. 15, 16, 17

[8] W. Shen, J.A. Kornfield, and D.A. Tirrell. *Macromolecules*, 40:689–692, 2007. 15, 16, 17, 18

[9] W. Shen, J.A. Kornfield, and D.A. Tirrell. *Soft Matter*, 3:99–107, 2007. 15, 16, 18

[10] D. Brokx, Richard, Maria M. Lopez, J. Vogel, Hans, and G. I. Makhatadze. Energetics of target peptide binding by calmodulin reveals different modes of binding*. *The Journal of Biological Chemistry*, 276(17):14083–14091, 2001.

[11] Silvia Montigiani, Giovanni Neri, Paolo Neri, and Dario Neri. Alanine substitutions in calmodulin-binding peptides result in unexpected affinity enhancement. *Journal of Molecular Biology*, 258(1):6–13, 1996. 16

[12] John C. Crocker and David G. Grier. Methods of digital video microscopy for colloidal studies. *Journal of Colloid and Interface Science*, 179(1):298–310, 1996. 16

[13] V. Breedveld and D. J. Pine. Microrheology as a tool for high-throughput screening. *Journal of Materials Science*, 38(22):4461–4470, 2003.

[14] T. G. Mason and D. A. Weitz. Optical measurements of frequency-dependent linear viscoelastic moduli of complex fluids. *Physical Review Letters*, 74(7):1250–1253, 1995. PRL. 16

[15] Bradley D. Olsen, Julia A. Kornfield, and David A. Tirrell. Yielding behavior in injectable hydrogels from telechelic proteins. *Macromolecules*, 43(21):9094–9099, 2010. 17, 18

[16] Tom Annable, Richard Buscall, Rammile Ettelaie, and D Whittlestone. *Journal of Rheology*, 37:695–726, 1993. 17, 24, 27

[17] J. Scanlan. *J. Polym. Sci.*, 43:501, 1960. 17

[18] L. C. Case. *J. Polym. Sci.*, 43:397, 1960. 17

[19] Tom Annable, Richard Buscall, and Rammile Ettelaie. Network formation and its consequences for the physical behaviour of associating polymers in solutiion. *Colloids and Surfaces A: Physicochemical and Engineering Aspects*, 112:97–116, 1996. 17

[20] Wei Shen, Kechun Zhang, Julia A. Kornfield, and David A. Tirrell. Tuning the erosion rate of artificial protein hydrogels through control of network topology. *Nat Mater*, 5(2):153–158, 2006. 17

[21] Jan Philipp Junker, Fabian Ziegler, and Matthias Rief. Ligand-dependent equilibrium fluctuations of single calmodulin molecules. *Science*, 323(5914):633–637, 2009. 19

[22] M. S. Green and A. V Tobolsky. A new approach to the theory of relaxing polymeric media. *The Journal of Chemical Reviews*, 14:80–92, 1945. 17, 19

[23] H. Pelzer. Kinetic theory of the elasticity of rubber. *Reports on Progress in Physics*, 6:330–334, 1939. 19

[24] A.S. Lodge. A network theory of flow birefringence and stress in concentrated polymer solutions. *Trans. Faraday Soc.*, pages 120–130, 1956. 20

[25] A. Kaye. *Brit. J. Appl. Phys.*, 17:803–806, 1966. 20

[26] Misazo Yamamoto. The visco-elastic properties of network structure i. general formalism. *Journal of the Physical Society of Japan*, 11(4):413–421, 1956. 20

[27] Misazo Yamamoto. The visco-elastic properties of network structure ii. structural viscosity. *Journal of the Physical Society of Japan*, 12(10):1148–1158, 1957. 20

[28] A. S. Lodge. Constitutive equations from molecular network theories for polymer solutions. *Rheologica Acta*, 7(4):379–392, 1968. 20

[29] R.H.W. Wintjes, R. J.J. Jongchaap, M.H.G. Duits, and J. Mellema. A new transient model for associative polymer networks. *Journal of Rheology*, 43(2):375–391, 1999. 20

[30] R. J.J. Jongchaap, R.H.W. Wintjes, M.H.G. Duits, and J. Mellema. A generalized transient network model for associative polymer networks. *Macromolecules*, 34:1031–1038, 2001. 22

[31] F. Tanaka and S. F Edwards. Viscoelastic properties of physically crosslinked networks. transient network theory. *Macromolecules*, 25:1516–1523, 1992. 22

[32] F. Tanaka and S. F Edwards. *J. Non-Newtonian Fluid Mech.*, 43:247–271, 273–288,289–309, 1992. 22

[33] F. Tanaka. *Polymer Physics: Applications to Molecular Association and Thermoreversible Gelation.* Cambridge University Press, New York, 2011. 23

[34] F. Tanaka and T. Koga. *Macromolecules*, 39:5913, 2006. 23

[35] F. Tanaka and Masahiko Ishida. Elastically effective chains in transient gels with multiple junctions. *Macromolecules*, 29:7571–7580, 1996. 23

[36] F. Tanaka and T. Koga. Intramolecular and intermolecular association in thermoreversible gelation of hydrophobically modified associating polymers. *Computational and Theoretical Polymer Science*, 10:259–267, 2000.

[37] Fumihiko Tanaka. Thermoreversible gelation of associating polymers. *Physica A: Statistical Mechanics and its Applications*, 257(14):245–255, 1998. 23

[38] M. E. Cates and S. J. Candau. Statics and dynamics of worm-like surfactant micelles. *Journal of Physics: Condensed Matter*, 2(33):6869, 1990. 23

[39] M.E. Cates. *Macromolecules*, 20(9):2289–2296, 1987. 23

[40] L. Leibler, M. Rubinstein, and R. Colby. Dynamics of reversible networks. *Macromolecules*, 24:4701–4707, 1991. 23

[41] M. Rubinstein and N Alexander, Semenov. Dynamics of entangled solutions of associating polymers. *Macromolecules*, 34:1058–1068, 2001.

[42] M. Rubinstein and A. N. Semenov. Thermoreversible gelation in solutions of associating polymers: 2. linear dynamics. *Macromolecules*, 31:1386–1397, 1998.

[43] A. N. Semenov and M. Rubinstein. Thermoreversible gelation in solutions of associative polymers. 1. statics. *Macromolecules*, pages 1373–1385, 1998. 23

[44] James T. Kindt. Simulation and theory of self-assembly and network formation in reversibly cross-linked equilibrium polymers. *The Journal of Chemical Physics*, 123(14):144901–11, 2005. 24

[45] Daniel Vernon and Michael Plischke. Viscoelasticity near the gel point: A molecular dynamics study. *Phys. Rev. E.*, 64:031505–1–031505–5, 2001.

[46] Robert S. Hoy and Glenn H. Fredrickson. Thermoreversible associating polymer networks. i. interplay of thermodynamics, chemical kinetics, and polymer physics. *The Journal of Chemical Physics*, 131(22):224902, 2009. 24, 27

[47] K. C. Tam, R. D. Jenkins, M. A. Winnik, and D. R. Bassett. A structural model of hydrophobically modified urethaneethoxylate (heur) associative polymers in shear flows. *Macromolecules*, 31(13):4149–4159, 1998. 25

[48] Y. Serero, V. Jacobsen, J. F. Berret, and R. May. Evidence of nonlinear chain stretching in the rheology of transient networks. *Macromolecules*, 33(5):1841–1847, 2000. 25

[49] Sharon X. Ma and Stuart L. Cooper. Shear thickening in aqueous solutions of hydrocarbon end-capped poly(ethylene oxide). *Macromolecules*, 34(10):3294–3301, 2001. 26

[50] G. Marrucci, S. Bhargava, and S. L. Cooper. Models of shear-thickening behavior in physically crosslinked networks. *Macromolecules*, 26(24):6483–6488, 1993. 26

[51] B. H. A. A. van den Brule and P.J. Hoogerbrugge. Brownian dynamics simulation of reversible polymer networks under shear using a non-interacting dumbbell model. *Journal of Non-Newtonian Fluid Mechanics*, 113:303–334, 1995. 26

[52] J. Mewis, B. Kaffashi, J. Vermant, and R. J. Butera. Determining relaxation modes in flowing associative polymers using superposition flows. *Macromolecules*, 34(5):1376–1383, 2001. 27

[53] Anubhav Tripathi, Kam C. Tam, and Gareth H. McKinley. Rheology and dynamics of associative polymers in shear and extension: theory and experiments. *Macromolecules*, 39(5):1981–1999, 2006. 27

[54] Shi Qing Wang. Transient network theory for shear-thickening fluids and physically crosslinked networks. *Macromolecules*, 25(25):7003–7010, 1992. 27

3

Effects of defects on the shear stress relaxation in self-assembled protein networks

3.1 Introduction

Self-assembled networks formed by cross-linking of proteins with specific interactions are of practical interest for possible applications in drug delivery and other areas of biomaterials.(1–15) The ability to precisely engineer the length and properties of connecting segments, combined with the enormous variety of binding groups that are available in naturally occurring proteins, provides a powerful toolbox to create hydrogel networks with desired properties. The use of monodisperse components with high-specificity, high-affinity interactions facilitates a precise connection between experiment and theory by eliminating uncertainties about the dynamics, thermodynamics, and stoichiometry of interactions that are typical of traditional hydrogels. Due to the specificity of the interactions, network rearrangements can be unambiguously defined in terms of discrete binding and dissociation events with well-defined stoichiometry, rather than the breaking and forming of ill-characterized interactions within aggregates of unknown structure. The dissociation rates for high-affinity protein-protein interactions are slow enough ($\sim 0.01 - 100s^{-1}$) that relaxation of local network conformation can be assumed to be complete in between bond-breaking events.

Systems with these features lend themselves to systematic investigation of the connections between microscopic events and bulk rheological properties, under a different set of assumptions than has been typically used to treat reversible networks formed by chains containing multiple weak sticky sites.(16–30) For instance, recent work has explored the rheology of synthetic peptides interacting via leucine zipper domains, with particular attention to controlling the tendency of loop formation through binding of two domains within the same peptide.(4–6) The network organized from a single component monomer engineered as a triblock protein - two leucine zipper domains flanking a flexible linker domain. The leucine zipper domains originating from the same monomer or from a different monomer joined in a tetramer or a pentamer arrangement. Their binding strength and thus the overall material properties could be rationally altered via adjustments in the pH of the medium.

Another recent example of an engineered gel was developed and studied by Topp et al.(7) The architecture in that example relied on the mixing of two components, a divalent linker segment (terminated by calmodulin-binding peptide domains) and a tetravalent junction assembly featuring four calmodulin domains, bound together by leucine zipper interactions. As the calmodulin/CBP attraction is dependent on the presence of calcium ions, so the gel formation depended sensitively on calcium content.

Aside from the sensitivity to calcium content, the architecture of this system is intriguing for having distinct junction and linker components. One practical advantage is that a small number of junction types and linker types can be combined to form a large variety of gels with different properties. Furthermore, the use of two-component gels has the advantage that gel formation may be initiated simply by mixing the components, rather than relying on external triggers such as changing solution properties.(31) Another interesting property - which may be a benefit or a liability for practical applications is the ability to vary the level of network defects (for instance, dangling linker ends or unfilled junction sites) simply by changing the mole ratio of junctions and linkers. As equilibrium constants K_D for bond dissociation may be in the nanomolar or picomolar range, the equilibrium ratio of defects to bonds formed may be as low as 10^{-3} or 10^{-4} assuming perfect stoichiometry. Tuning the ratio of the two components away from a 1:1 matching of junction and linker sites, however, will lead to a controllable defect fraction that is not sensitive to K_D. In this study, we use mesoscale simulation and theory to explore some general aspects of long-time dynamics in networks formed from mixtures of polyvalent junctions with divalent linkers (Figure 3.1).

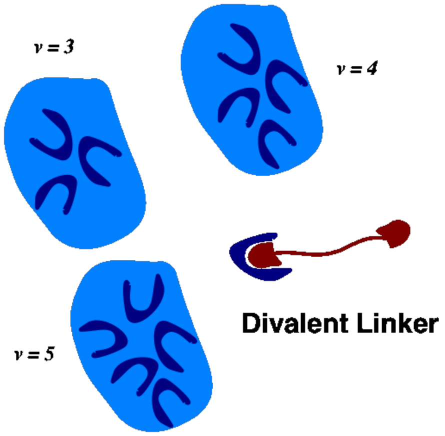

Figure 3.1: Cartoon representations of "junctions" and "linker" components -

The basis of the analysis is the hypothesis that defects play an essential role in the dynamics of the network at long timescales. The classical transient network model of Green and Tobolsky [16] posits that the breaking of a small fraction of the bonds in the system relaxes, on average, the corresponding fraction of the shear stress in the system. The rate of relaxation is therefore congruent to the rate of chain breaking, consistent with experimental observations that the characteristic times measured for strand rearrangements correspond to the shear stress relaxation time.(4, 5, 5) As noted by Rubinstein and Semenov (20) dissociation events in a network are frequently followed by recombination, as the partners cannot diffuse away from each other. If a linker dissociates from a junction binding site, three outcomes are probable: the linker will re-associate with the same site, the linker will associate with a different nearby unoccupied junction binding site, or a nearby dangling linker will associate with the junction binding site. The latter two outcomes result in the migration of the defect (open junction site or dangling linker) to a new site, along with replacement of one bond with a new bond. Over time this rearrangement of bonds allows the network to flow, or to relax stress from an initial applied shear strain. In the following we use a simple simulation model to evaluate the rate of defect migration, and the resulting rate of relaxation of shear stress, and their dependence on junction multiplicity, defect concentration, and linker stiffness. The results are used to develop a phenomenological theory to predict the dependence of shear viscosity on the thermodynamics and kinetics of linker-junction binding, stoichiometric mismatch, and junction multiplicity. Finally, the time-dependence of viscosity during gel aging is modeled as an approach to equilibrium through diffusion-limited recombination of complementary defects.

3.2 Simulation Model

3.2.1 Key Assumptions

We focus on stress relaxation via discrete defect-mediated network rearrangement events. We assume that these events take place on a timescale ($\sim k_{off}^{-1} = 10^{-3} - 10^{2} s$, with k_{off} the first-order linker-junction dissociation rate) that is long compared with the linker relaxation time ($\sim 10^{-6} s$) that will mediate the structural fluctuations of the network at fixed connectivity. Therefore, between defect migration events the structure equilibrates fully. Molecular dynamics (MD) simulation trajectories of the fixed network are performed between bond rearrangements (modelled via a Monte Carlo (MC) procedure) to sample the equilibrium fluctuations in structure and shear stress. While the true interval between bond-breaking events would be described by a Poisson distribution with a mean of $(2N_L k_{off})^{-1}$ (with N_L the number of linkers in the system), for our purposes we only aim for MD simulation intervals long enough that successive bond rearrangement events are uncorrelated and that structural and thermodynamic averages can converge to equilibrium values.

We assume that the linker-junction bond has a very low dissociation equilibrium constant K_D so the linker-junction dissociation is a rare event. The probabilities that both ends of the linker dissociate at once, or that two neighbouring linkers dissociate simultaneously and exchange junctions, are treated as negligible. Therefore, once one end of the linker dissociates, a linker will always either re-form a bond with the same junction or with a nearby junction. The fraction of free sites during the simulation is conserved, and is solely dependent on the stoichiometric mismatch between junctions and linkers. Furthermore, the dissociation rate is assumed independent of linker extension.

Once a linker is dissociated at one end, it is assumed to rapidly sample an equilibrium distribution of linker lengths and to rotate rapidly and isotropically around the junction to which it remains attached. Its probability of reattachment either to its original junction or to a new junction is therefore assumed to be proportional to the equilibrium probability that the linkers extension matches the distance between the remaining junction and the new or original junction.

These assumptions form the bases of the mixed MD/MC simulations described below. From the simulation results we seek the factors determining success rate of defect migrations and the relationship between defect migration events and shear stress relaxation. Using these relationships we will then consider in general how the stress relaxation rate will depend, in a linker-junction network, on stoichimetry, junction valence, kinetic and equilibrium dissociation constants of the linker-junction bond (k_{off} and K_D), and preparation history of the network.

3.2.2 Model details

The simulation model consists of N_J "junctions", which interact with all other junctions via a repulsive short-ranged potential, and N_L "linkers" connecting pairs of junctions, which appear as bonding interactions between pairs of junctions. Bonded and repulsive potential functions are plotted in figure 3.2. For the bonding interaction, an anharmonic potential is used that represents the extensibility of the linker:

$$U_b(r) = \frac{1}{4}k^* \left(r^2 - r_o^2\right)^2 \tag{3.1}$$

where k^* is the force constant and r_o is the equilibrium length of the linker. This quartic potential was used instead of a harmonic potential to give a stiffer upper limit to the maximum distance between linked junctions. Other than their effects in bridging junctions, linkers positions and configurations are not explicitly defined; they may cross each other with no topological restrictions. Entanglements, repulsion between linkers, and orientation effects (i.e. linker-junction-linker angle dependence) are neglected.

In the absence of a non-bonded repulsive potential, the network collapses into a dense cluster of linked junctions after many MC/MD cycles. Therefore, in addition to the bonded potential, a purely repulsive $1/r^{12}$ potential between all pairs of junctions (whether or not connected by linkers) was used. This repulsive potential is truncated smoothly to zero through a shift potential at a distance of $r_c = 0.766r_0$. The repulsive potential, which is similar to a hard-sphere potential for spheres of diameter $0.7r_0$, represents excluded volume interactions between junctions. Details of this repulsive potential are given in equation 3.2 and table 3.1.

$$U_{rep}(r) = \begin{cases} C_{rep}(r^{-12} - D) & r \leq r_1 \\ C_{rep}(r^{-12} - A(r - r_1)^3 - B(r - r_1)^4 - D) & r_1 < r < r_c \\ 0 & r \geq r_c \end{cases} \tag{3.2}$$

Parameters A, B, and D are chosen to satisfy continuous first and second derivatives of the potential at the shift function start distance r_1 and that the potential and force reach zero at the cut-off distance r_c.

The valency ν of the network is defined as the maximum number of linkers that may bind to each junction in that network. In a defect-free network with N_J junctions, the total number of linkers (N_{Lo}) would equal $N_J \cdot \nu/2$. In the current simulations, the properties of the network are defined in terms of linker to junction mismatch, more specifically in terms of the fraction of missing linkers denoted s, compared to the total number needed in a perfectly matched network. The stoichiometric mismatch factor s is related to the actual number of linkers in the network (N_L) and the total number of linkers of a defect free network (N_{Lo}) as $s = 1 - N_L/N_{Lo}$. Simulations were performed used a range of valencies, fractions of missing linkers, and spring constants k^* as indicated in table 3.2. In each case, to generate a starting configuration, junctions were placed at the vertices of an fcc lattice with nearest neighbor distance equal to the bond length r_0 . Pairs of junctions to be linked (ν pairs per junction) are chosen randomly among the twelve possibilities dictated by the fcc-lattice nearest neighbours. The defect sites were created by randomly cancelling the bonded interactions among an appropriate number of pairs of bonded junctions, representing a deficit of linkers.

Constant NVE molecular dynamics (MD) simulations were performed using Gromacs 3.3.(32) The Monte Carlo (MC) moves and the incorporation of the

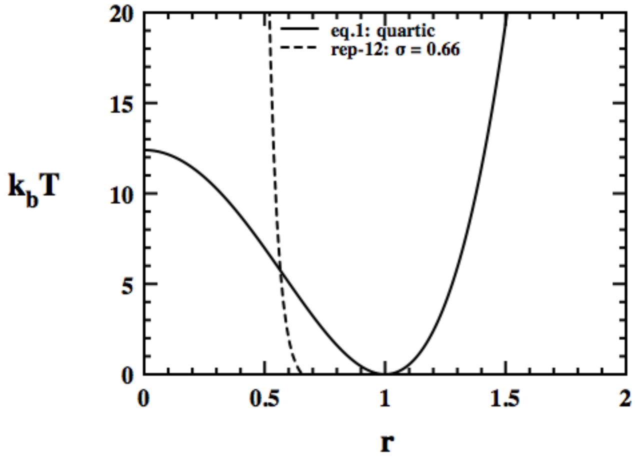

Figure 3.2: Form of interaction potential used in simulations - Bonded and repulsive potential functions (eq. 3.1 and 3.2), in reduced units; bonded potential shown is for $k^* = 20$.

Table 3.1: Overview - Simulation Parameters in Reduced Units.

thermal energy (k_BT^*)	1.0
energy-minimized linker length (r_0)	1.0
junction mass (m^*)	1.0
force constant (k^*) (unless otherwise noted)	20.0
repulsive potential parameter C_{rep}	$6.43 \cdot 10^{-3}$
shift function start distance (r_1)	0.745
1/r12 cut-off distance (r_c)	0.766
A, B, D	$-2.92 \cdot 10^6, 9.77 \cdot 10^7, 28.8$
MD time step (t^*)	0.0004
duration of MD relaxation interval	62.0
number density of junctions (n^*)	$\sqrt{2}$

necessary Gromacs utilities were handled with a homemade Perl wrapper script. The total length of the trajectories collected for each of the systems consists of a minimum of $3.0 \cdot 10^5$ Monte-Carlo bond rearrangement move attempts, each followed by a molecular dynamics (MD) relaxation interval. The length of each MD trajectory (155,000 time steps, or 62 times the reduced time unit of $(m^* r_0^2/k_B T)^{1/2}$), was chosen to give sufficient time for that relaxation, rather than represent the true (assumed very long) interval between junction dissociations. The junction velocities were generated from a Maxwell-Boltzmann distribution appropriate to the system temperature at the start of each MD trajectory. Periodic boundary conditions were imposed in the xyz directions of a cubic simulation box.

Table 3.2: Overview - Simulation Networks.

Junctionvalency (ν)	fraction of missing linkers (s)	linker spring constant (k^*)
3	0.005, 0.025, 0.0375, 0.050	20
4	0.005, 0.025, 0.050	20
	0.005, 0.025	40
	0.005, 0.025	80
	0.005, 0.025	120
5	0.040, 0.080, 0.140	20

3.2.3 Monte Carlo algorithm for bond-rearrangement moves

The equilibrium dissociation constant K_D for the linker-junction bond is assumed to be low enough that linkers remain bonded to at least one junction at all times. Changes in connectivity proceed through breaking of linker-junction bonds and reforming new bonds at defective junctions (Figure 3.3). This defect migration move was attempted after each MD block.

First, randomly, a linker connecting any two junctions of the network is chosen with equal probability. Next, it is assumed that the selected linker disconnects itself from either junction with equal probability. At this stage, the dangling end of the linker will either reconnect itself to the old junction and thus leave the network

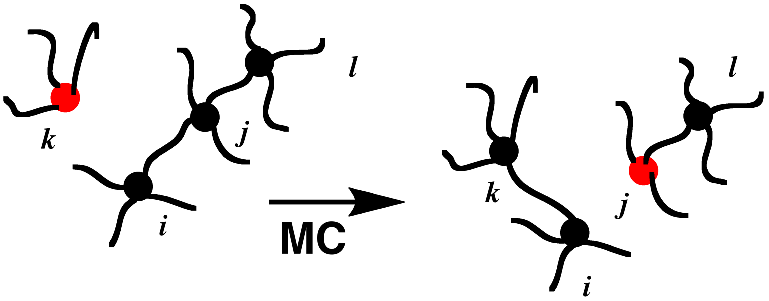

Figure 3.3: Molecular details of a successful Monte-Carlo (MC) move - Initially, one end of the linker connecting the junctions i and j disconnects due to the transient nature of the linker-junction interaction. In its vicinity, junction k has an incomplete valency due to the stoichiometric imbalance. Upon the successful defect migration, the linker connects junction i with junction k. The junction with an incomplete valency is now junction j.

topology unchanged, or form a new bond by attaching itself to any defect junction in the system. In either case, the probability of reattachment to some junction (new or old) is 1, consistent with the assumption of a very low K_D. The probability of forming each possible connection (new or old) is proportional to the Boltzmann factor $exp[-U_b(r_{ij})]$ associated with the linkers potential energy U_b at the new (or old) bond length r_{ij}. In a system with no defects ($s = 0$), the probability p of reattachment to a new junction becomes zero and the network connectivity cannot change. The simulation model does not permit a linker to attach at both ends to the same junction (i.e. loop), nor does it permit more than one linker to bridge any pair of junctions (i.e. double-bond). According to linear response theory, the network viscosity can be computed from the integral of the autocorrelation function of the off-diagonal elements σ_{ij} (where i and j represent x,y, or z and $i \neq j$) of the stress tensor.(33, 34) At a given fixed connectivity (i.e., in between defect migration events) the average shear stress of the network cannot in general relax to zero, but converges to some non-zero average after a period of local fluctuations in structure. After each Monte-Carlo move attempt an MD simulation with bonds fixed was performed as described above. Stress tensor elements were derived from these simulations using the following equation:

$$\sigma(t/t_{MC}) = \left\langle \frac{1}{V} \sum_{k \neq l} r_{i(kl)} (f_{j(kl)}^{bonded} + f_{j(kl)}^{repulsive}) \right\rangle \tag{3.3}$$

where r and f are distance and force respectively, k and l are indices of junctions, i, j are Cartesian directions, and triangular brackets indicate an average over a single MD trajectory.

The averages of σ_{ij} fluctuate around zero over a full trajectory consisting of 300,000 MC defect migration attempts each followed by an MD trajectory (Figure 3.4, top panel). The time correlation function $C_{\sigma\sigma}$ of σ_{ij} , averaged over the three shear directions, is shown in Figure 3.4 (lower panel) along with a best-fit single exponential decay curve. All systems yielded good approximations to single-exponential shear stress time correlation functions:

$$C_{\sigma\sigma}(t) = C_o \exp(-t/\tau_{shear}) \tag{3.4}$$

In the presence of bonds, the shear stress remains strongly correlated over many MC/MD blocks, confirming that the average values of σ_{ij} from equation 3.3 are well-converged. The majority of the shear stress arises directly from the bonded forces; for instance, at $\nu = 4, k^* = 20, s = 0.005$, the rms contribution to all σ_{ij} from the bonding potential terms accounted for 85% of the total rms value of off-diagonal stress elements. The constraints imposed by the linkers can lead to persistent steric repulsions between junctions, which will contribute to the systems response to applied shear and are appropriate to include in equation 3.3. (A velocity-dependent term is also included in the calculation of stress tensor elements by Gromacs, but over the course of a single trajectory its contribution is negligible, $< 1\%$ of the root-mean-square stress for off-diagonal elements σ_{ij}.) In the absence of bonds, shear stress correlations decayed within a single MD trajectory, indicating that the

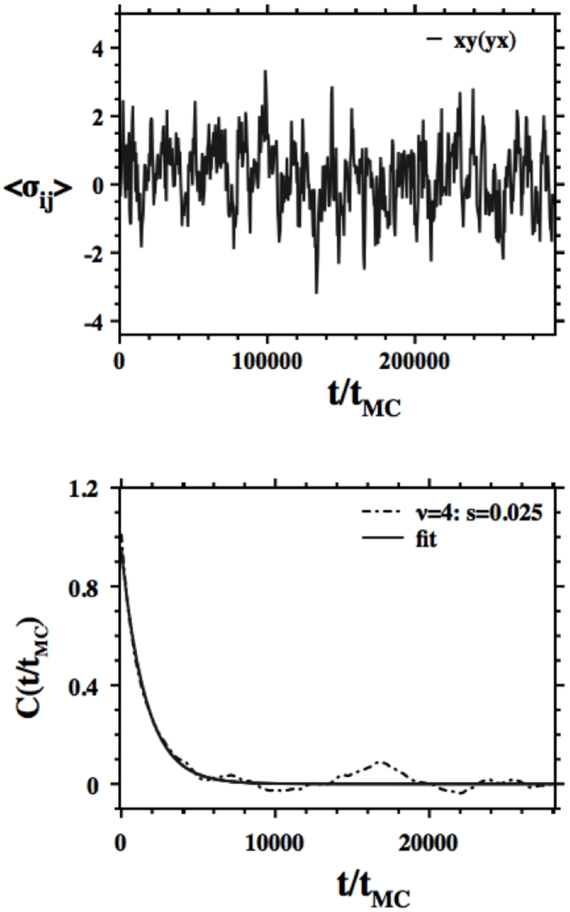

Figure 3.4: Example trajectory stress tensor element and time-correlation function - (Top panel)The evolution of one of the off-diagonal elements of the stress tensor ($\langle\sigma_{xy}\rangle$) over a full trajectory of 300,000 MC steps in a tetravalent network with $k^* = 20$ and $s = 0.025$. (Lower panel) The resulting time stress-stress autocorrelation ($C_{\sigma\sigma}$) function and its exponential fit.

junctions alone flow freely in the absence of bonds. The exponential fit of the correlation function to equation 3.4 yields a shear relaxation time in terms of the time between MC steps, t_{MC}. Based on the model assumptions, this interval corresponds to $(2N_L k_{off})^{-1}$; we use this conversion to express a dimensionless relaxation rate $k_{off} \cdot \tau_{shear}$ in the Results and Discussion sections.

3.3 Results

3.3.1 Rate of defect migration

The fraction p of junction-linker dissociation events that lead to defect migration in simulations increases with the product of stoichiometric mismatch s and junction valence ν, as shown in figure 3.5. Systems with the same linker extension force constant but different valence give nearly identical curves. Increasing force constant with fixed valence and mismatch s yielded decreasing defect migration probabilities (Figure 3.6).

The dimensionless shear relaxation times $k_{off} \cdot \tau_{shear}$ decreased with increasing stoichiometric mismatch, and were generally lower for the trivalent system than for networks with $\nu = 4$ or 5. (Figure 3.7) . Relaxation times increased with increasing linker extension force constant. (Figure 3.8)

The shear viscosity η is related to the integral of shear stress autocorrelation function $C_{\sigma\sigma}$ by:

$$\eta = \frac{V}{k_B T} \int_0^\infty C_{\sigma\sigma}(t) dt \qquad (3.5)$$

with V the system volume.(32, 33) With an autocorrelation function following the simple exponential form of equation 3.4, and using simulation units where $k_B T = 1$, this yields $\eta = VC_0 \cdot \tau_{shear}$. In an equilibrium network system with a single stress

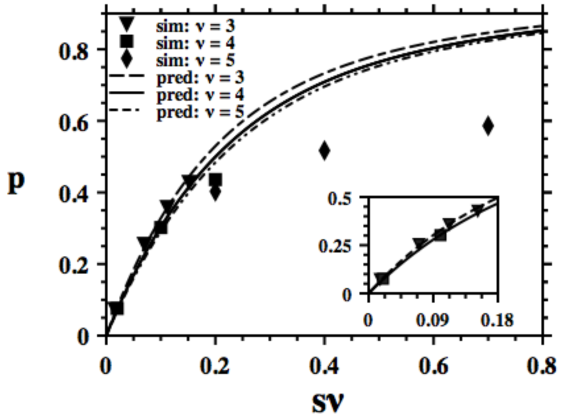

Figure 3.5: Rate of defect migration - The fraction of successful defect migration moves (p) vs. the fraction of junctions with available binding sites ($s\nu$) from simulations with k*=20 bonded potential spring constant. The symbols are the simulation values, while curves are the predicted defect migration probabilities from equations 3.6-3.8.

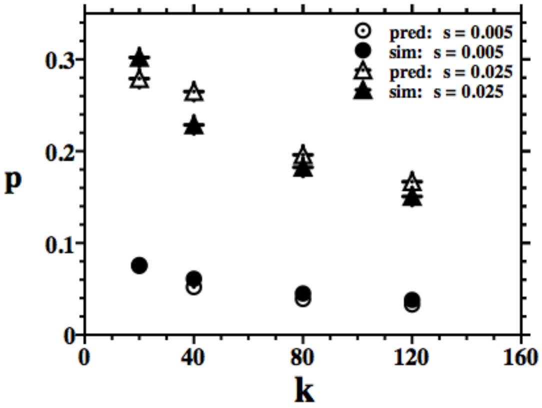

Figure 3.6: Rate of defect migration in stiffer networks - Simulation and predicted defect migration probabilities (p) with increasing the spring constant of the bonding potential (k^*). The data shown are for tetravalent networks with $s = 0.005$ and $s = 0.025$.

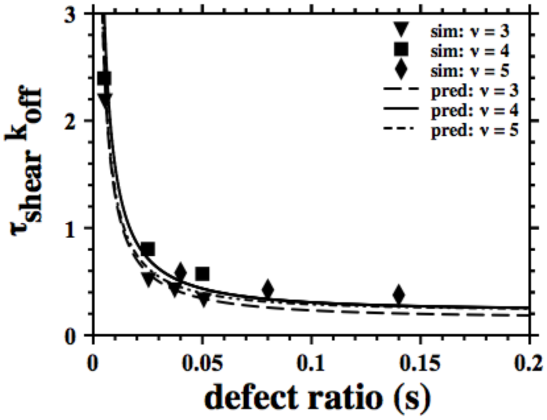

Figure 3.7: Relaxation time vs. stoichiometric mismatch in simulation - Dimensionless network shear relaxation times ($\tau_{shear}k_{off}$) vs. the fraction of missing linkers (s) from simulations (symbols) and predictions (solid curves) for $k^* = 20$.

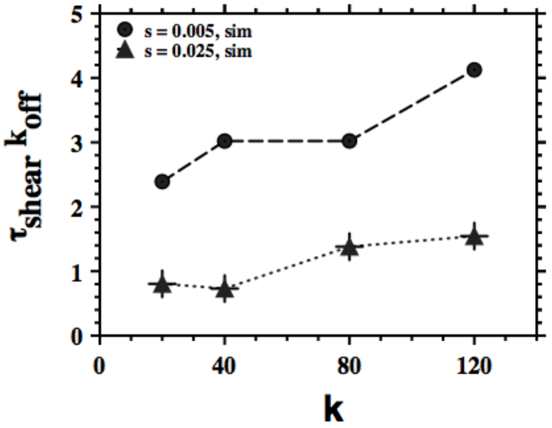

Figure 3.8: Relaxation time in stiffer networks - Dimensionless network shear relaxation times ($\tau_{shear}k_{off}$) in tetravalent networks as a function of linker extension force constant (k^*).

relaxation time τ_{shear} , the viscosity can be expressed as the product of τ_{shear} with the shear modulus G of the corresponding fixed network ($\eta = G\tau_{shear}$).(18–20, 35) Therefore, $G = VC_0$. Figure 3.9 shows G, normalized to linker density, for all networks simulated. The network shear modulus per linker increases with increasing junction valence. Fixed networks with greater defect fractions can be seen as mixtures of junctions with different valences, so it is consistent with this trend that increasing s lowers the modulus per linker for $\nu = 4$ and $\nu = 5$. There furthermore seems to be an increase in modulus per linker with increased linker stiffness (figure 3.9, lower panel). In general, the trends suggest that the greater the degree of constraint on the junction positions (due to higher valence or stiffer linkers), the greater the shear modulus per linker.

3.4 Discussion

The interpretation of simulation results is conveniently decomposed into two questions: how does the rate of defect migration depend on system properties, and how does stress relaxation depend on defect migration?

3.4.1 Rate of defect migration

The rate of successful defect migration per linker-junction association is the product of the rate of linker-junction dissociation k_{off} and the fraction p of dissociation events that are not followed by trivial recombination of the original linker-junction pair. The product $k_{off} \cdot p$ is analogous to the inverse of the renormalized effective bond lifetime τ_b^* in the theory of Semenov and Rubinstein.(20) As we assume high linker-junction affinity, this recombination is inevitable unless the linker can bind to another open site. The migration success fraction p is therefore related to the ratio of the number of open sites to the number of junctions, which (again, in the limit of high

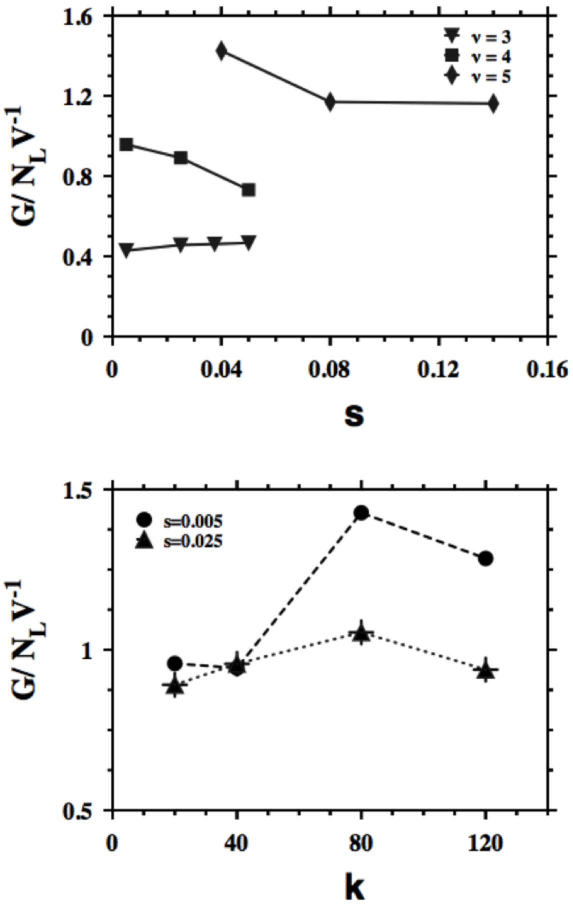

Figure 3.9: Fixed network shear modulus - Dimensionless fixed-network shear modulus (G) for networks $k^* = 20$ and varying stoichiometric mismatch (s) (top) and for tetravalent networks at varying linker stiffness k^* (bottom).

linker-junction affinity) is proportional to the product of the stoichiometric mismatch factor s and the junction valency ν.

To understand the dependence of p on s, ν, and k^* observed in simulations and plotted in figures 3.5 and 3.6, we seek the probability that a defect-containing junction is in reach of a linker that has dissociated at one end from its junction site. We first determine the average total number of junctions N_r within bonding range of a junction, excluding junctions already linked to that junction (because double bonding was not permitted in the simulations). To find N_r here we use structural information from the simulations, specifically the pair radial distribution function $g_{nb}(r)$ between non-bonded junctions. Figure 3.10 shows $g_{nb}(r)$ at three valencies obtained from averaging over simulated structures. The structure apparent in the non-bonded radial distribution function is qualitatively similar to that of a hard-sphere fluid at a volume fraction of 0.25, (36) except for a depletion of non-bonded neighbor density near $r = 1$ (more pronounced with increasing valence ν) due to the enrichment of bonded neighbors near the bonded potential minimum. To obtain N_r we integrate numerically over the distribution of junction-junction separation distances derived from simulations, weighting each distance by the Boltzmann weight associated with forming a bond of a given length. The effective mean number N_r of junctions within bonding range, exclusive of those currently linked to a given junction, can be calculated as:

$$N_r = \rho \int_0^\infty 4\pi r^2 g_{nb}(r) \frac{\exp -(\beta U_b(r))}{\langle \exp -(\beta U_b(r)) \rangle_b} \, dr \tag{3.6}$$

with ρ the total junction concentration, $g_{nb}(r)$ the pair distribution function between junctions that are not connected by a linker, and the bracketed average of Boltzmann weights in the denominator taken over the distribution of bonded junctions. Table 3.3 shows values of N_r obtained numerically using Eq. 3.6, in which the bonded potential U_b is taken from Eq. 3.1 and simulation results were used for $g_{nb}(r)$. Because the dependence of $g_{nb}(r)$ on stoichiometric mismatch s was negligible (curves at varying s were identical within the thickness of the lines plotted in figure 3.10), we treat N_r as independent of s. The decrease in N_r with increasing ν comes from the exclusion of increasing numbers of bonded neighbors from the potential sites for forming a new bond, while the decrease with increasing k^* comes from the narrowing of the range of stable bond lengths.

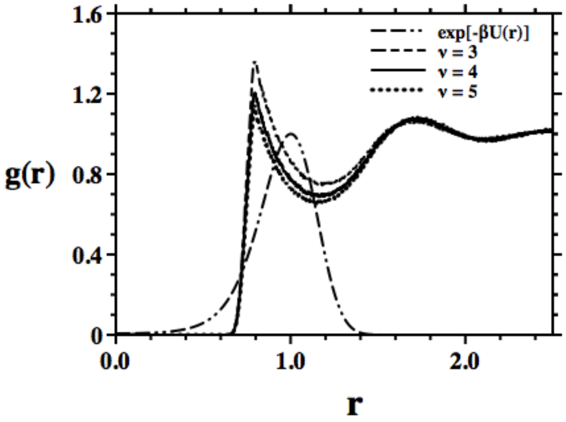

Figure 3.10: Non-bonded junctions network structure - Non-bonded radial distribution functions ($g_{nb}(r)$) vs. r from simulations at varying network valence and Boltzmann weight associated with the bonded potential $exp[-U_b(r)]$ for $k^* = 20$ (two dots-dashed curve).

Table 3.3: Networks in Simulation -Overview - Nonbonded neighbor junctions (N_r) from simulations.

Junction valency (ν)	Spring Constant (k^*)	N_r
3	20	8.3
4	20	7.5
4	40	5.3
4	80	3.8
4	120	3.1
5	20	7.1

At very small $s\nu$, the probability of a single available defect within bonding range is simply $N_r s\nu$, the probability of multiple defects within bonding range is negligible, and given equal chance of the linker recombining with its current junction or binding to the defect, the migration success probability $p = s\nu N_r/2$. When the product $s\nu N_r$ is comparable to unity, the likelihood of multiple defects within bonding range cannot be neglected. To estimate p in this regime, we need to consider the probability P_i that $i = 0, 1 \ldots N_r$ of the N_r neighbouring junctions may have a defect site. Assuming that defects are distributed randomly,

$$P_i = \left(\frac{N_r!}{(N_r-1)!i!}\right)(s\nu)^i(1-(s\nu))^{N_r-i} \tag{3.7}$$

A linker dissociating from a junction with i defects in binding range will have a probability of $1/(i+1)$ of returning to its original junction, so the probability of successful migration of the defect will be $i/(i+1)$. Summing over possible numbers of neighbouring junctions with defects i we can approximate an overall probability of defect migration:

$$p = \sum_{i=0}^{N_r}\left(\frac{i}{i+1}\right)P_i \tag{3.8}$$

Since N_r calculated from equation 3.6 is generally not an integer, we evaluate p as the weighted sum of values calculated with the two nearest integers. We note that at low $s\nu$, P_i is negligible for $i \geq 2; P_i \sim N_r s\nu$ from Eq. 3.7; and Eq. 3.8 reduces to $p \sim s\nu N_r/2$.

The application of equations 3.7-3.8 and data from Table 3.3 to predict the success rate of defect migration over a range of valencies, linker stiffnesses, and stoichiometric mismatches is successful in the limit of low $s\nu (s\nu < 0.2)$, as shown in inset of figure 3.5 and figure 3.6. These equations however overpredict the success probability at higher values of $s\nu$. The near collapse of the three curves in figure 3.5 onto one shows that changing the topology of the networks has a small effect on the resulting defect migration probabilities at fixed $s\nu$ and linker stiffness. Increase in linker stiffness leads to a significant decrease in p (Figure 3.6), as a less flexible linker has a narrower bonding range and fewer potential bonding partners (Table 3.3).

In an experimental system where the $U_b(r)$ and $g(r)$ are not known, N_r might be estimated from linker and junction dimensions. With an estimate r_{max} for a maximum probable linker extension, and a minimum approach distance r_{min} (calculated from the junction diameter, plus any minimum extension distance for the linker):

$$N_r \sim \frac{4\pi}{3}\rho(r_{max}^3 - r_{min}^3) \tag{3.9}$$

This approximation amounts to an assumption of constant $g_{nb}(r) = 1$ and a square-well form for the bonding potential $U_b(r)$.

3.4.2 Effect of defect migration on stress relaxation

A range of timescales is typically observed in experimental stress relaxation profiles for associating networks (see e.g. ref. 26). The present analysis produces simple exponential relaxation (see fig. 3.4). Here, only relaxation on the timescale of junction-linker dissociation is included in the calculation, as the rapid fluctuations of the network at fixed connectivity are averaged out over the MD sampling intervals. The use of a simple divalent linker (rather than a linker with multiple associative sites), the exclusion of multiple bonds, and the absence of any entanglement effects (explicitly excluded, but arguably unimportant in a system with short linkers) remove other additional relaxation processes that may introduce additional complexity.

From figures 3.5 and 3.7 it is evident that increased stoichiometric mismatch leads to increasing defect migration rates and decreased stress relaxation times. To pursue this analysis in more depth we consider the transient network model of Green and Tobolsky. (16) According to this model, the breaking of one of N_L linkers within the network should on average relax a fraction $1/N_L$ of the shear stress in the system. The autocorrelation function for the off-diagonal elements of the pressure tensor should therefore follow:

$$C_{\sigma\sigma}(t) = C_0 \left(\frac{N_L - 1}{N_L}\right)^{t/\tau_{mig}} \approx C_0 \exp\left(\frac{-t}{N_L \cdot \tau_{mig}}\right) \tag{3.10}$$

where τ_{mig} is the average time between successful defect migration events, i.e. $(2N_L k_{off} p)^{-1}$. Comparison with equation 3.4 leads directly to $\tau_{shear} = N_L \tau_{mig} = (2pk_{off})^{-1}$. However, the shear stress relaxation times obtained from simulation were between 2 and 4 times faster than predicted by equation 3.10. We therefore recast equation 3.10 with an additional constant a as:

$$C_{\sigma\sigma}(t) = C_0 \left(\frac{N_L - a}{N_L}\right)^{t/\tau_{mig}} \approx C_0 \exp\left(\frac{-at}{N_L \cdot \tau_{mig}}\right) \tag{3.11}$$

with a representing an effective number of linkers relaxed per migration event, yielding

$$\tau_{shear} = N_L a^{-1} \tau_{mig} = (2apk_{off})^{-1} \tag{3.12}$$

Values of the a parameter determined by equation 3.11 are shown in figure 3.11 for a range of systems at different valences ν and stoichiometric mismatch fractions s.

To interpret the deviation from the transient network theory prediction that $a = 1$, we consider two assumptions of the model that leads to eq. 3.11:

1. defect migration events involve bonds that support an average amount of stress
2. breaking one bond does not influence the stresses supported by any other bonds

If highly-stressed linkers are more likely to migrate (in violation of the first assumption) the average defect migration event will relax a disproportionate fraction of the shear stress in the system. By construction in the present simulations, the probability of an initial bond-breaking event is independent of bond extension. Nevertheless, high-energy linkers are less likely to re-form, and therefore more likely to migrate, than linkers near the minimum extension. Indeed, as shown in figure 3.12, the distribution of bonds broken and reformed during successful bond migrations

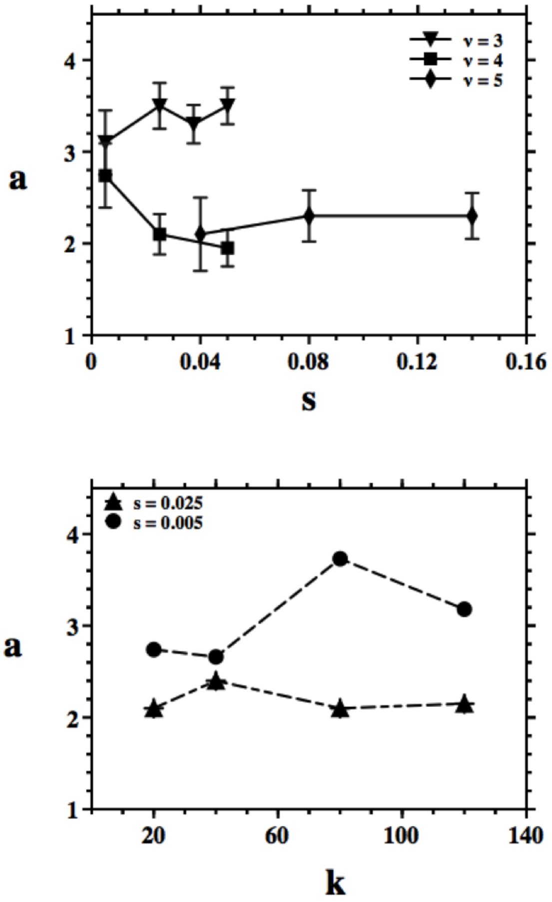

Figure 3.11: Effective number of linkers affected by migration move vs. stoichiometric mismatch - The effective number of linkers (a) relaxed by each defect migration event, from fits of $C_{\sigma\sigma}$ obtained in simulation to Eq. 3.11, versus the fraction of missing linkers (s) at $k^* = 20$ (upper) and for varying k^* at $\nu = 4$ (lower).

(new bonds) is broader than the overall bond length distribution (all bonds), indicating a modest selection bias towards highly stretched or highly compressed (i.e., high-stress) linkers. Their disproportionate representation among the bonds breaking and forming will tend to produce a value of $a > 1$.

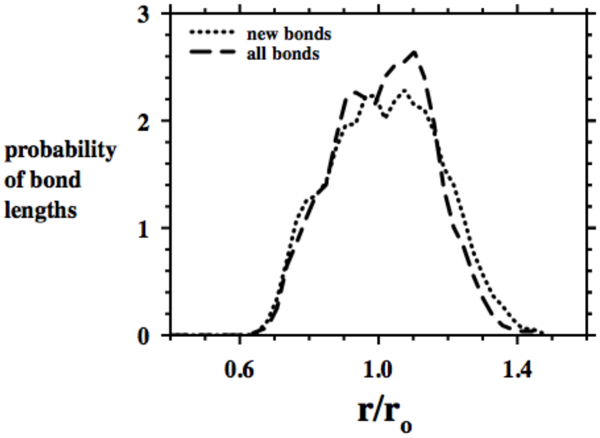

Figure 3.12: Distributions of linker lengths - Normalized length distribution of newly formed bonds (..) versus all bonds (–) in a tetravalent system($k^* = 20, s = 0.025$).

In the limit of high defect concentration s where the defect migration event success probability p approaches 100%, the average stress of a migrating linker must equal the average stress of all linkers, and the first assumption becomes exactly valid; conversely, when successful defect migration is rare, the bias towards migration of high-energy, high-stress bonds may become greater. This trend is illustrated in figure 3.13, where a is plotted versus the success probability p for all cases. With the exception of the trivalent systems, a tends toward larger values at small p. At $p > 0.15$, however, a plateaus near 2 (and not 1) for $\nu = 4$ and $\nu = 5$, indicating that selective migration of highly-stressed bonds is not the primary explanation for $a > 1$.

Breakdown in the assumption that bond rearrangement involving one linker will not affect stress in other linkers is likely to account for the finding of $a \approx 2$ in tetra- and penta-valent systems. Such an effect is not at all surprising; the shift in a linkers connectivity changes the mean force on both new and the old defect junction sites,

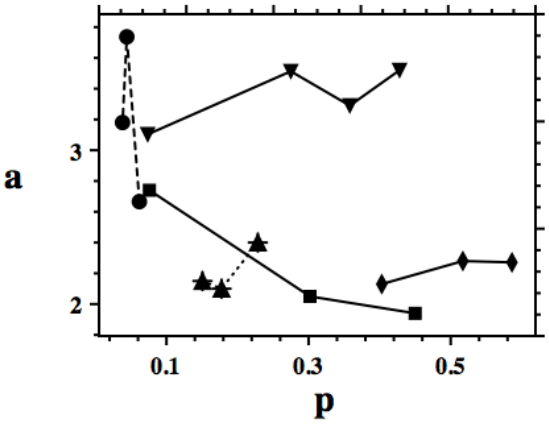

Figure 3.13: Number of linkers affected by migration move - Fractional stress per defect migration a vs defect migration success probability p for all the simulated systems ($k^* = 20$: $\nu = 4$: rectangles, $\nu = 5$: rhombi, $\nu = 3$: inverted triangles, $\nu = 4$, $s = 0.005$, k-dependence:circles, and $\nu = 4$, $s = 0.025$, k-dependence:triangles).

resulting in a change in mean position that affects the stresses experienced by all other linkers attached to those junctions. It appears that in the present simulations, this indirect effect is roughly equal to the direct effect assumed in transient network theory, leading to $a \sim 2$ (except at low p), and is not strongly sensitive to valence (above $\nu = 3$) or to linker stiffness.

The anomalous behaviour of trivalent networks (with a consistently greater than 3) can also be explained through a breakdown in the second assumption. In a trivalent system, there is a qualitative difference in the freedom of motion of a junction that is bonded to three other junctions via linkers, and a defect junction, which is bonded to two. A trivalent junction with one site vacant is no longer a junction in a topological sense, but simply the midpoint of an extra long and flexible linker consisting of two regular linkers connected by the defect junction. Transfer of the defect from one junction to another will have a pronounced effect on the stresses not only of the linker that migrates, but also of the other linkers on both junctions involved in the transfer. This could enhance the indirect effect and account for the higher stress relaxation per migration event. In summary, the linker-junction bond dissociation rate, the number of linkers relaxed by each defect migration event, and the shear stress relaxation time relate as $\tau_{shear} = (2ak_{off}p)^{-1}$. The parameter a here is an empirical factor determined from simulations; however, this relationship has some predictive power, as a appears to remain roughly constant over a range of conditions (Fig. 3.11). Fixing $a = 2.3$ for all $\nu = 4$ and $\nu = 5$ networks and $a = 3.3$ for $\nu = 3$ networks, and using Eq. 3.6-3.8 to calculate p, we can model the dependence of the shear relaxation over a continuous range of stoichiometric mismatch values and compare our results with simulation in Fig. 3.7. Deviation is seen at high mismatch, where the numerical model overpredicts the success rate p of defect migration.

Given the linear relationship between p and mismatch s at small s, we can generally predict an inverse relationship between τ_{shear} and degree of mismatch at low s (i.e., $s\nu < 0.1$),

$$\tau_{shear} = (2k_{off}ap)^{-1} = (ak_{off}N_r s\nu)^{-1} \tag{3.13}$$

Simulation and our simple model differ in details at higher s, but both show that p levels off, and τ_{shear} should fall off more slowly with increasing s than indicated by equation 3.13. Equation 3.13 predicts an unphysical infinite relaxation time in the limit of perfect stoichiometric matching, $s = 0$; this problem will be addressed in the following section.

3.4.3 Relevance to other regimes

The simulations described above represent systems containing defects of only one type: free junction sites resulting from a stoichiometric deficit of linkers. In the remainder of the discussion, we consider how insights from these simulations are applicable to systems with excess linkers and to systems where both defect types are present at equilibrium. Finally, the rate at which the defect levels approach their equilibrium values, following a perturbation or during the initial network assembly,will be treated.

3.4.3.1 Linker excess vs. linker deficit

In a network formed with a small excess of linkers, the predominant defect type will be a linker with only one end attached to a junction. The dangling end can migrate through a rearrangement very similar to the one shown in figure 3.3. A spontaneous junction-linker dissociation event on a site near a dangling end defect may be followed either by recombination of the original pair or by formation of a new bond between the junction and the dangling linker. In the latter case, the initially dissociated linker, left with no free junction sites, becomes a new dangling end defect. Under the same assumptions of rapid equilibration of the linkers and neglect of linker-linker interactions, this migration will proceed at the identical rate and have the identical impact on stress relaxation as the migration of a vacant junction site. Therefore, we predict that a linker excess should have a similar effect on the rate of stress relaxation as a linker deficit of the same magnitude, and that the dependence of viscosity on mixing ratio should be symmetric around the exact matching condition.

At the exact matching condition ($s = 0$), there remains at equilibrium a low level of both types of defect, analogous to the intrinsic concentration of free electrons and holes in an undoped semiconductor or to the concentration of hydronium and hydroxide ions in pH-neutral water. In the above simulations, the intrinsic defect concentration was assumed to be negligible compared with the defects arising from the deficit of linkers. The actual equilibrium concentrations of linker-junction bonds formed (ρ_{LJ} = number of linker-junction bonds per unit volume) resulting from mixing pre-defined densities of junction sites ($\rho_J = \nu N_J/V$) and linker sites ($\rho_L = 2N_L/V$) can be calculated through the law of mass action. Using an equilibrium constant K_D for the reaction in which a linker dissociates from a junction site yields the following:

$$\rho_{LJ} = \frac{1}{2}\left\{ \begin{array}{c} (K_D + \rho_L + \rho_J) \\ \pm\left(\rho_J^2 + \rho_L^2 + K_D^2 - 2\rho_{LJ} + 2\rho_L K_D + 2\rho_J K_D\right)^{1/2} \end{array} \right. \tag{3.14}$$

The fraction m_{eq} of junction sites that contain a defect of either type at equilibrium is obtained by adding the free linker site concentration $(\rho_L - \rho_{LJ})$ and the free junction site concentration $(\rho_J - \rho_{LJ})$ and dividing by ρ_J :

$$m_{eq} = (\rho_L + \rho_J 2\rho_{LJ})/\rho_J \tag{3.15}$$

In a stoichiometrically balanced mixture, with $\rho_J = \rho_L$, and in the limit of low K_D, equations 3,14 and 3.15 simplify to

$$m_{eq} = 2(K_D/\rho_J)^{1/2} \tag{3.16}$$

If we assume that the contributions from migration of both types of defect are additive (and neglect any contributions from events where defect pairs are created or annihilated), we can use Eq. 3.16 and the approximate relation $p = N_r m_{eq}\nu/2$ (valid for low m_{eq}) to estimate the shear stress relaxation time at the stoichiometric matching conditions at equilibrium:

$$\tau_{shear,eq} = \frac{1}{2k_{off}ap} = \frac{1}{k_{off}a\nu m_{eq}N_r} = \frac{1}{2k_{off}a\nu N_r\sqrt{\frac{K_D}{\rho_J}}} \tag{3.17}$$

Figure 3.14 shows theoretical total equilibrium defect concentrations as a function of linker/junction ratio, and the resulting dependence of relaxation time on composition, for a system with properties modelled on a Cm/CBP interaction with 1 nM K_D. The notable result is that even a 0.5% deviation from perfect stoichiometric matching of linkers and junctions changes the relaxation time several-fold. Farther from perfect

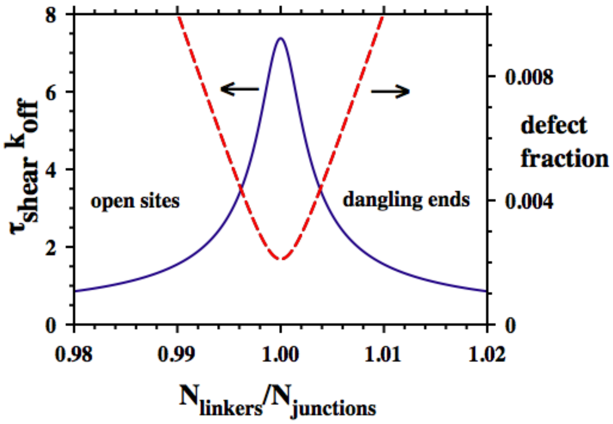

Figure 3.14: Predicted relaxation time vs. stoichiometric mismatch - The equilibrium fraction (m) of junction sites containing a defect (dashed curve) and the dimensionless shear relaxation time $\tau_{shear}k_{off}$ (solid curve) vs. the degree of linker mismatch ($N_L/N_{Lo} = \nu N_J/2$), calculated according to equations 3.13-3.16 for a tetravalent system with dissociation constant $K_D = 10^{-9}$ M and $\rho_J = 1.0 \times 10^{-3} M$. The value $a = 2.3$ was used based on simulation results.

matching, dependence of relaxation time on mixing ratio is less sensitive as the probability of successful defect migration p reaches a plateau region. In fact, the relationship $\tau_{shear} \sim k_{off}^{-1/2}$ is roughly obeyed as $p \sim 1/2$ and $a \sim 2$.

Contrary to intuition, following Eq. 3.17, the shear stress relaxation time τ_{shear} at perfect stoichiometric matching is predicted to decrease when the junction valency is increased and the junction concentration N_J/V kept constant (assuming no change to other kinetic and structural properties). This prediction arises because the probability that a bond breaking event will lead to a defect migration is proportional (in this limit) to the fraction of junctions that have a defect, which is in turn proportional to the square root of the junction valence.

3.4.3.2 Time-dependent defect levels during approach to equilibrium

As the model predicts a strong dependence of shear stress relaxation time on the defect concentration, the material properties of the network should evolve as defect concentrations approach their equilibrium levels during the initial formation of a gel or following a perturbation. Here we assume starting conditions in which most junctions and linkers are fully saturated, but with moderate, equal concentrations of both dangling linkers and open junction sites. The same defect diffusion process that provides a mechanism for stress relaxation also provides the means for defects of different types to find and cancel each other out. When a dangling linker is close (within a linker distance r_0) to an open junction site, this defect annihilation will proceed very quickly; therefore, we treat this process as a diffusion-controlled reaction where the diffusing reactants are the defects. The second-order rate constant (k_{dcr}) for defect annihilation is estimated in formula 18 based on the standard formula $k_{dcr} = 4\pi R^*(D_A + D_B)$.(37) The diffusion coefficients D for both types of defect should be equal and can be estimated by considering the rate of defect migration per defect ($\approx \nu N_r k_{off}/2$) and the mean migration distance ($\sim r_o\sqrt{2}$) to give $D = \nu N_r k_{off} r_0^2/6$ for three dimensions. Assuming a reaction distance R^* of r_o yields:

$$k_{dcr} = (4\pi/3)\nu N_r k_{off} r_o^3 \qquad (3.18)$$

The rate of defect annihilation is proportional to the product of the concentrations of the two defect types, each of which accounts for half the defect density ($m\rho_J$). This rate is balanced at equilibrium by the rate of formation of new defect pairs, which (in a nearly perfect network) can be considered a constant. The net rate of change in defect concentration is therefore:

$$\frac{dm\rho_J}{dt} = -2k_{dcr}\left(\frac{m}{2}\rho_J\right)^2 + 2K_D k_{dcr}\rho_J \qquad (3.19)$$

We note that substituting the equilibrium defect level m_{eq} from Eq. 3.16 into Eq. 3.19 leads to a net rate of zero, as appropriate for the equilibrium state. Solving equation 3.19 and dividing through by ρ_J gives the evolution of defect fraction:

$$m\,(t) = m_{eq}\frac{(1 + C\exp(-k_{dcr}\rho_J m_{eq} t))}{(1 - C\exp(-k_{dcr}\rho_J m_{eq} t))}$$

with:

$$C = \frac{m(0) - m_{eq}}{m(0) + m_{eq}} \tag{3.20}$$

which describes a non-exponential decay to m_{eq} from a network with initial defect fraction $m(0)$. For reasonable values of $m(0)$, defect levels approach equilibrium on a timescale

$$\tau_{age} = [k_{dcr}\rho_J m_{eq}]^{-1} \tag{3.21}$$

The timescale τ_{age} of the approach to equilibrium will generally be faster than the stress relaxation time at equilibrium; the ratio between the two reduces (through eq. 3.17, 3.18) to:

$$\frac{\tau_{age}}{\tau_{shear,eq}} = \frac{3a}{4\pi\rho_J r_o^3} \tag{3.22}$$

Applying Eqs. 3.17 and 3.20 yields the following expression for the linear shear stress response to a step-strain initiated at $t = 0$ when the system is in a non-equilibrium state ($m(0) > m_{eq}$):

$$\sigma(t) = \sigma(0)\exp\left(\frac{-t}{\tau_{shear,eq}}\right)\cdot\exp\left(\frac{1 - C\exp\left(-\frac{t}{\tau_{age}}\right)}{1 - C}\right)^{\left(-2\frac{\tau_{age}}{\tau_{shear,eq}}\right)} \tag{3.23}$$

with C defined as in Eq. 3.20. As shown in 3.15, this equation describes a relaxation with a rate that is initially faster than the equilibrium exponential relaxation rate but rapidly reduces to the equilibrium exponential decay function over a time $\tau_{age} = 0.70k_{off}^{-1}$ in the example plotted.

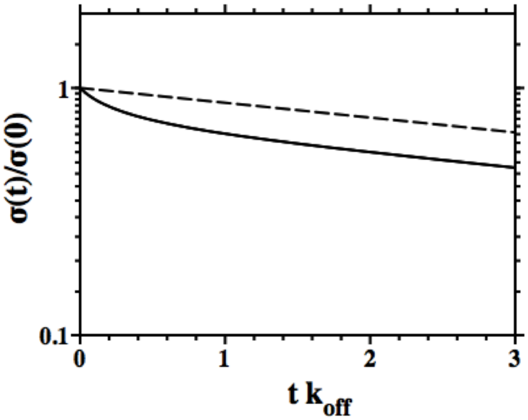

Figure 3.15: Step strain experiment: how stoichiometric mismatch sffects stress relaxation - Time-dependent relaxation of shear stress $\sigma(t)$ from eq. 3.23 for following a step strain imposed at $t = 0$ on network with non-equilibrium defect level $m(0) = 10m_{eq} = 0.02$ (solid line). System properties are as described for Figure 3.14, with $N_L/N_{Lo} = 1$. Dashed line shows the exponential stress relaxation for an equivalent system with equilibrium defect level $m_{eq} = 0.002$ at $t = 0$.

3.4.4 Relevance to single-component networks

The above analysis of time-dependent aging behavior (eq. 3.18-3.23, figure 3.15) under conditions of matched linker and junction concentrations is perfectly transferable to single-component networks formed from junctions with v sticky sites attached to flexible chains (maintaining the assumptions of high affinity, high specificity, rapid conformational relaxation of chains, and no loops or double bonds). Similarly, the equilibrium defect fraction and relaxation time of such a single-component self-assembled network are available from eq. 3.14-3.17, setting $\rho_L = \rho_J$. The concept of defect migration as a means of shear stress relaxation is therefore a general one. The junction/linker type of network is special primarily in that the defect concentration can be controlled simply by changing mixture composition.

3.5 Conclusions

In this report we have explored a simple simulation model to offer predictions for how stress relaxation rates in high-affinity, high-specificity junction/linker reversible networks will depend on the properties of the components and on their relative concentrations. Although the model relies on several assumptions, we hope that the predictions will be experimentally testable and lead to a deeper understanding of how specific network rearrangement events manifest in the rheology of reversible networks. The simulation model allowed the decomposition of the stress relaxation rate into the rate of discrete bond rearrangement events (defect migrations) in the network and the mean stress relaxation per defect migration. The mean stress relaxation per defect migration is greater than predicted by the classic theory of Green and Tobolsky(16) by a factor $a \sim 2 - 3$, with the factor a representing an effective number of linkers relaxed per migration event. The a factor is not strongly sensitive to changes in junction valence, linker properties, or stoichiometric mismatch; the greatest factor in stress relaxation is therefore the rate of bond rearrangements. We find a strong dependence of shear relaxation time τ_{shear} on the fraction mv of network junction sites bearing defects, which enable bond rearrangement processes as depicted in figure 3.3. Below $m\nu \sim 0.1$, this relationship to a good approximation

$$\tau_{shear} = (ak_{off}N_r m\nu)^{-1} \tag{3.24}$$

with N_r the effective number of neighboring junctions in bonding range that might contain defects. N_r is sensitive to linker properties; in systems with flexible linkers, a linker detached at one end is more likely to find a defect site at an appropriate distance, leading to a greater rate of bond rearrangement and faster relaxation. The defect level m in a stoichiometrically matched network is governed by the equilibrium between bonds forming and breaking

$$m_{eq} = 2(K_D V/\nu N_J)^{1/2} \tag{3.25}$$

Adding or removing linkers to or from a stoichiometrically matched network introduces additional defects to an extent proportional to the degree of mismatch s (fraction of missing or extra linkers) for $s > m_{eq}$. Assuming junction-linker interactions with a nanomolar dissociation constant K_D and millimolar junction concentration N_J/V, equation 3.25 yields values of the order $m_{eq} \sim 10^{-3}$. In such a system, we predict that the shear relaxation rate (and therefore the shear viscosity) will vary over an order of magnitude or so with only a few percent change in linker concentration around the stoichiometric matching condition. At defect levels $m\nu > 0.1$, where most junctions will be close to at least one defect, further increases in defect level will cause a weaker decrease in shear relaxation time than given by eq. 3.24.

The approach to equilibrium through annealing of defects in a stoichiometrically matched system has also been examined. Since the annealing process proceeds through the same defect migration process as stress relaxation, we predict that τ_{shear} approaches its equilibrium value (from a system that has been perturbed, or during the initial network formation) on a timescale τ_{age} that will generally be faster than the equilibrium shear relaxation time, with the ratio between these two times given in eq. 3.22.

References

[1] Martin Ehrbar, Ronald Schoenmakers, Erik H. Christen, Martin Fussenegger, and Wilfried Weber. Drug-sensing hydrogels for the inducible release of biopharmaceuticals. *Nat Mater*, 7(10):800–804, 2008. 36

[2] Paulina J. Skrzeszewska, Frits A. de Wolf, Marc W. T. Werten, Antoine P. H. A. Moers, Martien A. Cohen Stuart, and Jasper van der Gucht. Physical gels of telechelic triblock copolymers with precisely defined junction multiplicity. *Soft Matter*, 5:2057–2062, 2009.

[3] Julia E. Babensee. Interaction of dendritic cells with biomaterials. *Seminars in Immunology*, 20(2):101 – 108, 2008.

[4] W. Shen, J.A. Kornfield, and D.A. Tirrell. *Macromolecules*, 40:689–692, 2007. 37, 39

[5] W. Shen, J.A. Kornfield, and D.A. Tirrell. *Soft Matter*, 3:99–107, 2007. 39

[6] Wei Shen, Kechun Zhang, Julia A. Kornfield, and David A. Tirrell. Tuning the erosion rate of artificial protein hydrogels through control of network topology. *Nat Mater*, 5(2):153–158, 2006. 37

[7] Shana Topp, V. Prasad, Gianguido C. Cianci, Eric R. Weeks, and Justin P. Gallivan. A genetic toolbox for creating reversible ca2+-sensitive materials. *Journal of the American Chemical Society*, 128(43):13994–13995, 2006. 37

[8] F. Heath, P. Haria, and C. Alexander. Varying polymer architecture to deliver drugs. *AAPS Journal*, 9(2):E235 – E240, 2007.

[9] Keiji Numata and David L. Kaplan. Silk-based delivery systems of bioactive molecules. *Advanced Drug Delivery Reviews*, 62(15):1497 – 1508, 2010.

[10] L. Li, B. M. Charati, and L. K Kiick. Elastomeric polypeptide-based biomaterials. *J. Polym. Sci. A Polym. Chem.*, 1(8):1160 – 1170, 2010.

[11] Molly M. Stevens, Stephanie Allen, Martyn C. Davies, Clive J. Roberts, Jill K. Sakata, Saul J. B. Tendler, David A. Tirrell, and Philip M. Williams. Molecular level investigations of the inter- and intramolecular interactions of ph-responsive artificial triblock proteins. *Biomacromolecules*, 6(3):1266–1271, 2005.

[12] Rein V. Ulijn, Nurguse Bibi, Vineetha Jayawarna, Paul D. Thornton, Simon J. Todd, Robert J. Mart, Andrew M. Smith, and Julie E. Gough. Bioresponsive hydrogels. *Materials Today*, 10(4):40 – 48, 2007.

[13] Karin S. Straley and Sarah C. Heilshorn. Independent tuning of multiple biomaterial properties using protein engineering. *Soft Matter*, 5:114–124, 2009.

[14] R. Andrew McMillan, Jeanie Howard, Nestor J. Zaluzec, Hiromi K. Kagawa, Rakesh Mogul, Yi-Fen Li, Chad D. Paavola, and Jonathan D. Trent. A self-assembling protein template for constrained synthesis and patterning of nanoparticle arrays. *Journal of the American Chemical Society*, 127(9):2800–2801, 2005.

[15] Ian R. Wheeldon, Scott Calabrese Barton, and Scott Banta. Bioactive proteinaceous hydrogels from designed bifunctional building blocks. *Biomacromolecules*, 8(10):2990–2994, 2007. 36

[16] M. S. Green and A. V Tobolsky. A new approach to the theory of relaxing polymeric media. *The Journal of Chemical Reviews*, 14:80–92, 1946. 37, 56, 68

[17] L. G. Baxandall. Dynamics of reversibly crosslinked chains. *Macromolecules*, 22(4):1982–1988, 1989.

[18] L. Leibler, M. Rubinstein, and R. Colby. Dynamics of reversible networks. *Macromolecules*, 24:4701–4707, 1991. 51

[19] Michael Rubinstein and Audrey V Dobrynin. Associations leading to formation of reversible networks and gels. *Current Opinion in Colloid & Interface Science*, 4(1):83 – 87, 1999.

[20] M. Rubinstein and A. N. Semenov. Thermoreversible gelation in solutions of associating polymers: 2. linear dynamics. *Macromolecules*, 31:1386–1397, 1998. 39, 51

[21] F. Tanaka and S. F Edwards. Viscoelastic properties of physically crosslinked networks. transient network theory. *Macromolecules*, 25:1516–1523, 1992.

[22] F. Tanaka and S. F Edwards. *J. Non-Newtonian Fluid Mech.*, 43:247–271, 273–288,289–309, 1992.

[23] R. J.J. Jongchaap, R.H.W. Wintjes, M.H.G. Duits, and J. Mellema. A generalized transient network model for associative polymer networks. *Macromolecules*, 34:1031–1038, 2001.

[24] R.H.W. Wintjes, R. J.J. Jongchaap, M.H.G. Duits, and J. Mellema. A new transient model for associative polymer networks. *Journal of Rheology*, 43(2):375–391, 1999.

[25] Tom Annable, Richard Buscall, Rammile Ettelaie, and D Whittlestone. *Journal of Rheology*, 37:695–726, 1993.

[26] David M. Loveless, Sung Lan Jeon, and Stephen L. Craig. Rational control of viscoelastic properties in multicomponent associative polymer networks. *Macromolecules*, 38(24):10171–10177, 2005.

[27] Michael J. Serpe and Stephen L. Craig. Physical organic chemistry of supramolecular polymers. *Langmuir*, 23(4):1626–1634, 2007.

[28] Wayne C. Yount, David M. Loveless, and Stephen L. Craig. Small-molecule dynamics and mechanisms underlying the macroscopic mechanical properties of coordinatively cross-linked polymer networks. *Journal of the American Chemical Society*, 127(41):14488–14496, 2005.

[29] Shihu Wang, Chun-Chung Chen, and Elena E. Dormidontova. Reversible association and network formation in 3 : 1 ligand-metal polymer solutions. *Soft Matter*, 4:2039–2053, 2008.

[30] Robert S. Hoy and Glenn H. Fredrickson. Thermoreversible associating polymer networks. i. interplay of thermodynamics, chemical kinetics, and polymer physics. *The Journal of Chemical Physics*, 131(22):224902, 2009. 37

[31] Cheryl T. S. Wong Po Foo, Ji Seok Lee, Widya Mulyasasmita, Andreina Parisi-Amon, and Sarah C. Heilshorn. Two-component protein-engineered physical hydrogels for cell encapsulation. *Proceedings of the National Academy of Sciences*, 106(52):22067–22072, 2009. 38

[32] Erik Lindahl, Berk Hess, and David van der Spoel. Gromacs 3.0: a package for molecular simulation and trajectory analysis. *Molecular modeling annual*, 7(8):306–317, 2001. 42, 48

[33] Daan Frenkel and Smit Berend. *Understanding Moelcular Simulation: From Algorithms to Simulations*, volume 1. Academic Press, London, 2002. 45, 48

[34] Daniel Vernon and Michael Plischke. Viscoelasticity near the gel point: A molecular dynamics study. *Phys. Rev. E.*, 64:031505–1–031505–5, 2001. 45

[35] M. Rubinstein and R. Colby. *Polymer Physics*. Oxford University Press Inc., New York, 2003. 51

[36] Andrij Trokhymchuk, Ivo Nezbeda, Jan Jirsak, and Douglas Henderson. Hard-sphere radial distribution function again. *The Journal of Chemical Physics*, 123(2):024501, 2005. 53

[37] M von Smoluchowski. Versuch einer mathematischen theorie der koagulationskinetik kolloider lösungen. *Z. phys. Chem*, 92(129-168):9, 1917. 65

4

Simulation study of stress relaxation rates in transient network

4.1 Introduction

The rheology of supramolecular networks formed from transient interactions of chains has been an area of intense study through theory, experiment, and computation.(1) The diversity of this class of materials enables a wide range of applications,(2) but resists description based on simple universal principles. For various specific systems under various regimes, a comprehensive theoretical description of network rheology may involve elements of percolation theory, rubber elasticity theory, statistical theories of the distributions of defects, single-chain polymer dynamics, entangled polymer dynamics, and microscopic kinetics of association and dissociation.(3–26)

Protein engineering allows the high-affinity, high-specificity non-covalent lock and key interactions encoded in protein and peptide structures to be used in network building blocks in various ways.(27, 28) Two-component networks in which one component contains only lock sites and the other only key domains are useful in a practical sense because they allow gel formation to be initiated by mixing.(29) Furthermore, such networks are interesting because the ratio between linker and junction concentrations can be tuned to influence network properties.

In a recent simulation study on a simplified model junction-linker network system, where junctions contained $\nu \geq 3$ binding sites and linkers consisted of an elastic chain with binding domains at either end (depicted schematically in Fig. 4.1) we monitored the rate of bond breaking and reforming (defect migration) events, and fraction of shear stress relaxed per event.(22) The product of these two factors corresponds to the shear stress relaxation time in Maxwellian cases where shear stress relaxes with a single exponential time dependence. We found that the shear stress relaxation rate was two or more times faster than the defect migration rate, indicating that each linker that detached in a system with N_L linkers released more than twice its proportional share (G_0/N_L) of the stress in the system, even when all linkers were active in the sense that each connected a unique pair of multivalent junctions within the network. This multiplier effect was attributed to the secondary effect of releasing one bond from a junction on the stress supported by other linkers attached to that junction.

In the previous work it was also found that the plateau shear stress modulus G^0, or equivalently the high-frequency modulus of the corresponding *fixed* network structure, increased faster than linearly as linkers were added, in contrast to assumptions of classical rubber theory.

In the present study, extending the previous model calculations to linker-junction networks with higher junction multiplicity, and relaxing the prohibitions on linkers connecting sites on the same junction and on multiple linkers connecting the same pair of junctions, offers a broader perspective that allows us to make connections between these two results. A small fraction of loops was also allowed to form. The data appear qualitatively consistent with the following general relationship between the shear stress relaxation time and the bond rearrangement time:

$$\tau_{shear} = \frac{G^0}{c_L \left(\frac{\partial G^0}{\partial c_L}\right)_{c_J}} \frac{\tau_{bond}}{2} \tag{4.1}$$

where c_L and c_J are linker and junction concentrations. Equation 4.1 can be justified by considering ensembles of network topologies. In this report we present the new simulation data and discuss factors that influence the bond rearrangement rate, the stress relaxation rate, and the plateau shear modulus. We will conclude with an argument for the applicability of eq. 4.1 in the case of linker-junction networks, and a discussion of whether and how it may apply to associating networks in general.

4.2 Methods

Mixed molecular dynamics/Monte Carlo (MD/MC) simulations of network rearrangement and stress relaxation were performed as in ref. 30, with additional methods to account for loop formation and multiple bonding as specified below. Briefly, junctions are represented by particles that interact with other junctions via a purely repulsive isotropic potential, independent of bonding state. Linkers are represented via a bonding interaction between pairs of junction particles, representing the free energy of linker extension, with no explicit linker-linker interaction or linker-junction-linker angle potential energy. The number of binding sites per junction (valency ν) is fixed for each system, with the current work covering the range from $\nu = 3$ to $\nu = 9$. Where loops are permitted, both ends of a linker may occupy different sites on the same junction. The total number of linkers is less than $N_J\nu/2$, leaving a fraction s of junction sites open. States with a single dangling linker end are considered only as transient intermediates for network rearrangements; these are presumed to have a vanishingly short lifetime relative to the time between dissociation events (though still long relative to the internal relaxation of the danging linker), and so are not included in the calculation of the systems shear stress. In the same spirit, rearrangements involving the simultaneous breaking of more than one linker-junction bond were not considered.

Dissociation and reattachment are treated using a Monte Carlo procedure attempted between MD segments. The rate of dissociation is presumed to be independent of the bond extension. The relative probabilities of re-attachment of the linker end to all open junction sites i (including the linkers previous attachment site) are made proportional to $exp[-\beta U(r_{ij})]$, where r_{ij} is the distance between site i and the attachment site of the other end of the linker.

It is assumed that the affinity of linker ends for junction sites is very high, so that upon dissociation, the linker reattaches either to its original junction site or to a nearby open junction site before the MD simulation is resumed; the rearrangement of the network thus depends on a detached linker end reassociating with an open junction site defect, leaving the defect at its original attachement site. An MD trajectory at constant NVT in a cubic box is then used to generate an equilibrium thermal ensemble of junction configurations under the influence of the new linker network topology and to calculate the mean values of the pressure tensor. The duration of the MD simulation was 62 in reduced units of (junction mass $\times r_0^2/k_BT)^{1/2}$ for all simulations. However, the interval t_{MC} between MC steps represents the mean duration between junction-linker dissociation events, i.e. $(2N_Lk_{dissoc})^{-1}$.

In the previous work, no more than one linker could connect any pair of junctions (multiple bonds were prohibited) and a linker could not loop back to a different site of the same junction. In the present simulations, for certain trajectories, multiple bonds and/or loops were permitted. A loop could be formed if, upon dissociation of one end of a linker, an empty site exists on the junction to which the linker remains attached. The Boltzmann weight for forming a loop was assigned to be $w = 0.5$ corresponding to an energy penalty for forming the looped state of $0.7k_BT$ relative to the energy at its most stable extension. A looped linker does not exert any force on any junctions. The formation and breaking of multiple bonds, where allowed, was treated with the same statistics as for single bonds; no energy preference or penalty was assigned. During molecular dynamics trajectories, forces from all linkers were treated additively, so that the force between a pair of junctions at given distance was proportional to the number of linkers that connect them.

The description of bonded and non-bonded interactions between junctions was introduced previously (22). For the bonding interaction, an anharmonic potential is used that represents the extensibility of the linker:

$$U\left(r\right) = \frac{1}{4}k\left(\frac{r^2}{r_0^2} - 1\right)^2 \tag{4.2}$$

where k is the force constant (set to $20k_BT$) and r_0 is the equilibrium extension of the linker. A purely repulsive $1/r^{12}$ potential between all pairs of junctions (whether or not connected by linkers) was used. This repulsive potential is truncated smoothly to zero through a shift potential at a distance of $0.766r_0$. Details of this repulsive potential are given in ref. 22. In all simulations, 500 junctions were contained in a volume of $353.55r_0^3$, yielding a junction number density of $2^{1/2}$.

The original network topology is created by adding random linkers across nearest neighbor pairs in an fcc lattice of junctions, up to the limit of $N_J\nu(1-s)/2$, with no more than ν linkers attached per junction and no more than one linker per pair of junctions. $\sim 300,000 - 400,000$ cycles of one MD trajectory followed by one MC move attempt were performed for each system. The larger number of cycles was implemented for simulations with $\nu > 6$ networks. Following $\sim 10,000$ cycles of equilibration, the averages of the three off-diagonal pressure tensor components $_{ij}$ are recorded for each MD trajectory and used to calculate a time-correlation function across the trajectories:

$$C_{t/t_{MC}} = \left\langle \left\langle \sigma_{ij} \right\rangle_{t'/t_{MC}} \left\langle \sigma_{ij} \right\rangle_{(t'+t)/t_{MC}} \right\rangle \tag{4.3}$$

where the inner brackets represent averages within individual MD trajectories and the outer brackets represent an average over the three directions and across MD/MC steps throughout the trajectory.

The shear relaxation time (τ_{shear}) is determined by a fit to a single exponential for the decay in time correlation function:

$$C_{t/t_{MC}} = C^0 exp\left(-\frac{t/t_{MC}}{\tau_{shear}}\right) \tag{4.4}$$

From equation (4.4) the plateau shear modulus, G_0 corresponding to the fixed network is calculated as $G_0 = VC_0/k_BT$.

The topologies of the newly simulated systems along with the type of topological defects investigated are enumerated in table 4.1.

For each system modeled, the probability p that a linker-junction dissociation event would result in a new bond, and the statistics of loop formation and multiple bonding were also determined and tabulated in table 4.2. Values of p predicted using a previously derived formula (reference 22, equations 4.6-4.8) in all newly simulated systems are also given. This formula depends on determining the variable N_R, the mean number of neighbouring junctions (each carrying an average of $s\nu$ empty junction sites) available within bonding distance for a disconnected linker. The incorporation of multiple bonding and looping requires that the formula for calculating N_R be adapted, as the definition of an available junction site is expanded.

$$N_R = \frac{1}{\langle exp(-\beta U_b(r))\rangle_{bonds}} c_J \int_0^\infty 4\pi r^2 g_{avail}(r) exp(-\beta U_b(r)) dr + w_{loop} \tag{4.5}$$

Here, $g_{avail}(r)$ represents the pairwise junction radial distribution function calculated over only non-connected junctions (for single-bonding systems) or over all junctions (for multiply-bonding systems). This definition reduces to that given in ref.

Table 4.1: Overview of newly simulated systems

Bonding Type	Valency (ν)	Defect Concentration (s)
SB[a] only	5	0.025
	6	0.0047
	6	0.0253
	7	0.0051
	7	0.0251
	8	0.0250
	9	0.0248
SB and MB[b]	3	0.0227
	3	0.0507
	4	0.005
	4	0.025
	4	0.035
	4	0.050
	5	0.0248
	5	0.040
	6	0.0047
	6	0.0253
	7	0.0051
	7	0.0251
	8	0.0250
	9	0.0248
SB and Q[c]	4	0.005
	5	0.0096
	5	0.0248
	5	0.040
	6	0.0047
	6	0.0253
	7	0.0051
	7	0.0251
SB, MB, and Q	4	0.005
	5	0.0096
	5	0.0248
	5	0.040
	6	0.0047
	6	0.0253
	7	0.0051
	7	0.0251

a=single bonds between pairs of junctions
b=multiple bonds also allowed, c=loops

22 for systems where only single bonds are permitted and loops may not occur ($w_{loop} = 0$).

In networks with multiple bonding, the number of connections between pairs of junctions are described using the variable b_n or more precisely its average, $\langle b_n \rangle$, defined as average fraction of linkers involved in a specific mode of junction bonding across the entire MC/MD trajectory (i.e. $n = 1$ means single bonds, $n = 2$, double bonds, etc.).

Fractions of junctions containing two or more linkers bridging to the same junction (i.e. multiple bonds) increased when the junction valence increased (fig. 4.1, top panel). Across the trajectories, the final $\langle b_n \rangle$ values were reached after $\sim 10,000$ MC/MD cycles and remained constant. Across the trajectories the average fractions of loops take $\sim 40,000$ MC/MD cycles to reach the final values.

To better understand how different components of the interaction potential contribute to the shear modulus, network structures selected at random from the MD/MC simulations were simulated under applied shear stress. For each junction valence, three network topologies generated during the initial simulations (without multiple bonds or loops) were simulated under constant shear stress σ_{ij} (without defect migration) to calculate $G = d\sigma_{ij}/d\gamma$ in the low strain ($\gamma < 0.05$) linear regime. G was calculated from the average strain response of these topologies each sheared along three directions. Variability of G among different shear directions for the same topology, or among different topologies at the same ν, was of the order of 10% in most cases. These simulations were performed using the original forcefield parameters and with three variations: with bonding force constant increased by a factor of 2, with junction-junction non-bonded interactions eliminated, and with both non-bonded interactions eliminated and the anharmonic linker extension potential replaced by a harmonic potential with the same effective force constant.

4.3 Results

4.3.1 Network structure: multiple bonds and loops

In networks that allow multiple bonding, the statistics of multiple bonding can be predicted statistically from a model based on random assignment of the ν bonds of a central junction to the $\nu \times N_R$ sites available on neighboring junctions. The average fractions of linkers involved in a specific mode of junction binding, $\langle b_n \rangle$, with $n = 1$ for single bonding, $n = 2$ for double bonding etc., is:

$$\langle b_n \rangle = C_{n-1}^{\nu-1} \frac{N_R \cdot C_{\nu-n}^{\nu N_R - \nu}}{C_{\nu}^{\nu N_R}} \tag{4.6}$$

where the denomiator $C_{\nu}^{\nu N_R}$ is the total number of ways ν bonds can be distributed among νN_R sites. As mentioned previously in simulations N_R can take on non-integer values. In using equation 4.6, the reported $\langle b_n \rangle$ values are a weighted average between the two nearest integer neighbors bounding the N_R values calculated in simulation. Figure 4.1 shows that the predictions of eq. 4.6 yield excellent agreement with simulation results.

In figure 4.2 we show the resulting average fractions of loops $\langle q \rangle$ with changing the networks topology. Across the MC/MD trajectories the average fractions of loops fluctuate on the order of shown error bars. We observe that the loop fraction increases with valence when only single bonds can be formed, but otherwise remains constant independently of degree of stoichiometric mismatch, s.

4.3.2 Defect migration probability

The probability p in figure 4.3 refers to the probability of a linker end forming a new bond as opposed to returning to its original junction site. This probability is

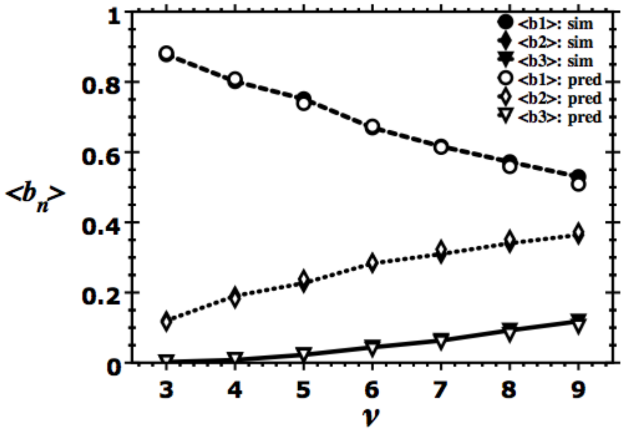

Figure 4.1: Structure of networks with multiple bonding: simulations and predictions - Average fractions of linkers $\langle b_n \rangle$ linking pairs of junctions vs. junction multiplicity (ν) from simulations and agreement with equation 4.6. The dark symbols are simulation values ; clear symbols correspond to predictions. The simulation data presented corresponds to $s \sim 0.025$ degree of stoichiometric mismatch. In all networks among the $b_n > 1$ modes of junction binding, the b_2 type of junction binding (double bonds) is dominant.

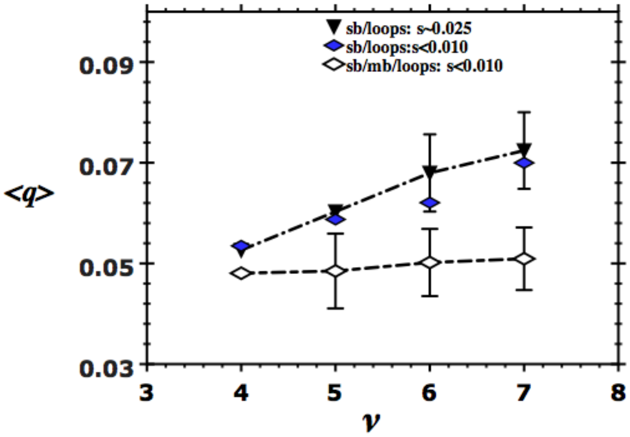

Figure 4.2: Structure of networks with loops - Mean fraction of looped linkers $\langle q \rangle$ (those with both ends attached to same junction) versus network junction multiplicity, ν. Linkers with ability to loop were introduced in networks having only single bonds between pairs of junctions or also multiple bonds in networks with similar concentrations of stoichiometric mismatch in mixing components.

determined irrespective of the initial or final linker topology (single bond, multiple bond, or loop.)

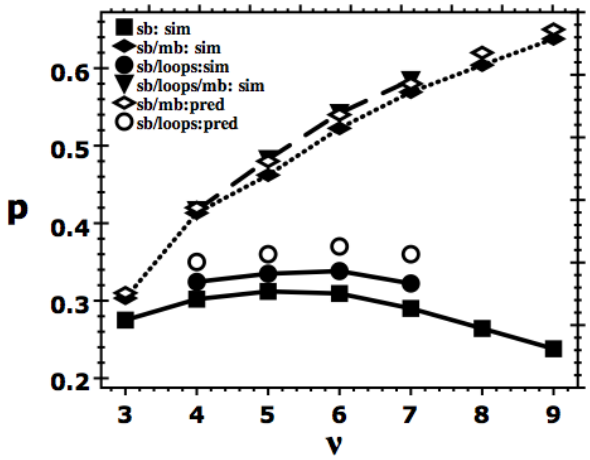

Figure 4.3: Rate of defect migration - Simulation probability of defect migration (p) vs (ν) for networks with single junction pairing, for systems with single bonding and loops, for networks with single bonds (sb) and multiple bonds (mb), and for the networks with sb, mb and loops (solid symbols and curves) at defect ratio $s \sim 0.025$. The clear symbols correspond to predictions using formula derived previously(22) (Eq. 3.8).

As shown in figure 4.3, the migration probability p at fixed defect fraction s increased with valence ν when multiple bonds were permitted. With only single bonds permitted, the defect migration probability reached a maximum and then decreased with higher ν. Sample agreement with predictions is shown for networks with single bonding and multiple bonding and networks with single bonding and loops. Predictions for the probability of defect migration in all other systems and for all degrees of stoichiometric mismatch are listed in table 4.2.

4.3.3 Plateau Storage Modulus G^0

Figure 4.4 shows the plateau shear modulus G^0 obtained from the variance in shear stress (see eq. 4.3 and 4.4) during MC/MD simulations for networks with different topologies as a function of the linker/junction ratio. Lower G^0 shear modulus values were obtained for networks allowing pairs of junctions to be bonded more than once

Table 4.2: Summary data analysis for all newly simulated networks

Bonding Type	ν	s	N_R	p_{pred}	p_{sim}	a	τ_{shear}	C_0	$G/N_L V^{-1}$	$G/N_{elastic} V^{-1}$
sb only	5	0.025	7.0	0.34	0.31	2.2	0.66	5.0	1.46	1.46
	6	0.0047	5.3	0.083	0.088	3.2	1.80	9.3	2.20	2.20
	6	0.0253	5.7	0.38	0.31	1.9	0.84	6.8	1.65	1.65
	7	0.0051	4.5	0.095	0.094	2.0	2.68	11.3	2.31	2.31
	7	0.0251	4.4	0.37	0.29	2.6	0.66	11.1	2.31	2.31
	8	0.0250	3.5	0.36	0.27	2.0	0.94	15.9	2.90	2.90
	9	0.0248	2.9	0.35	0.23	2.1	1.03	19.1	3.09	3.09
sb and mb	3	0.0227	10.2	0.31	0.30	3.8	0.47	0.68	0.33	0.35
	3	0.0507	10.5	0.53	0.53	3.3	0.30	0.59	0.30	0.32
	4	0.005	10.7	0.11	0.10	1.7	3.03	1.84	0.66	0.73
	4	0.025	10.4	0.42	0.41	3.0	0.44	1.78	0.65	0.72
	4	0.035	10.3	0.51	0.50	2.5	0.43	1.64	0.60	0.67
	4	0.050	10.2	0.62	0.60	2.3	0.40	1.66	0.62	0.69
	5	0.0248	10.5	0.48	0.46	2.0	0.57	2.84	0.83	0.94
	5	0.040	10.3	0.62	0.60	1.8	0.49	2.64	0.78	0.90
	6	0.0047	10.7	0.15	0.15	2.4	1.53	4.73	1.12	1.37
	6	0.0253	10.5	0.54	0.52	1.8	0.56	4.47	1.08	1.33
	7	0.0051	10.8	0.19	0.18	1.4	2.00	6.31	1.28	1.64
	7	0.0251	10.5	0.58	0.57	2.0	0.47	5.75	1.19	1.51
	8	0.0250	10.4	0.62	0.60	1.9	0.46	8.1	1.46	1.93
	9	0.0248	10.3	0.65	0.64	1.2	0.68	10.5	1.70	2.34
sb and loops	4	0.005	8.3	0.083	0.087	2.0	2.83	1.98	0.70	0.74
	4	0.025	8.2	0.35	0.32	2.2	0.70	2.18	0.79	0.83
	5	0.0096	7.4	0.17	0.18	2.6	1.13	4.18	1.20	1.27
	5	0.0248	7.3	0.36	0.33	2.4	0.61	4.31	1.25	1.33
	5	0.040	7.2	0.51	0.43	2.4	0.49	3.60	1.06	1.13
	6	0.0047	6.8	0.085	0.098	2.4	2.08	6.00	1.42	1.51
	6	0.0253	6.7	0.37	0.34	2.5	0.59	6.68	1.61	1.73
	7	0.0051	6.1	0.12	0.11	3.0	1.48	10.30	2.10	2.25
	7	0.0251	5.8	0.36	0.33	2.3	0.66	9.60	2.00	2.15
sb, mb, and loops	4	0.005	11.8	0.12	0.11	2.6	1.89	1.64	0.58	0.70
	4	0.025	11.5	0.44	0.42	2.5	0.52	1.54	0.56	0.69
	5	0.0096	11.9	0.26	0.24	2.4	0.90	2.62	0.75	0.96
	5	0.0248	11.5	0.51	0.48	2.1	0.53	2.53	0.74	0.95
	5	0.040	11.4	0.65	0.62	2.2	0.39	2.65	0.78	1.00
	6	0.0047	11.9	0.16	0.16	2.0	1.74	4.69	1.11	1.46
	6	0.0253	11.6	0.57	0.54	1.8	0.54	4.38	1.06	1.40
	7	0.0051	11.8	0.20	0.19	2.6	1.07	6.52	1.33	1.86
	7	0.0251	11.6	0.62	0.58	1.9	0.47	4.72	0.98	1.30

thus compelling us to explore the amount of stress arising from multiple bonds vs. single bonds. We define the number of effective elastic bonds, $N_{elastic}$, as the mean total number of pairs of junctions that are connected by one or more bonds, which can be related to the mean fractions $\langle b_n \rangle$ of linkers involved in different bonding modes as:

$$N_{elastic} = N_L \sum_n \frac{b_n}{n} \tag{4.7}$$

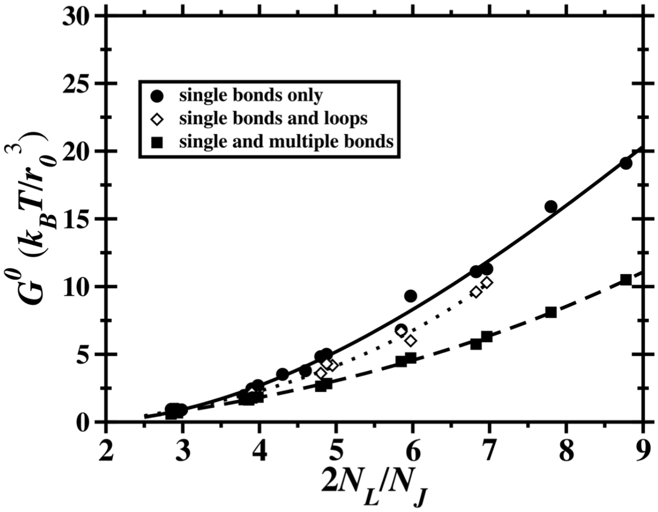

Figure 4.4: Plateau storage modulus from linear response theory simulations - Variations in shear modulus G^0 vs. mean network connectivity ($2N_L/N_J$) with defect type from simulations (symbols) and fits to the points.

The ratio of G^0 to the concentration of elastic bonds is plotted against that concentration ($N_{elastic}/V$) in figure 4.5. The data collapse approximately to a line, indicating that networks with single and multiple bonds with the same total number of bonds have similar G_0.

Simulations of three randomly selected network topologies (with only single bonds and no loops) from the MD/MC simulations were subject to applied shear stress to determine their storage modulus (figure 4.6). These simulations were repeated with identical topologies, but changing bonded and non-bonded interaction parameters as described in Methods. The averages over three network structures, sheared in three

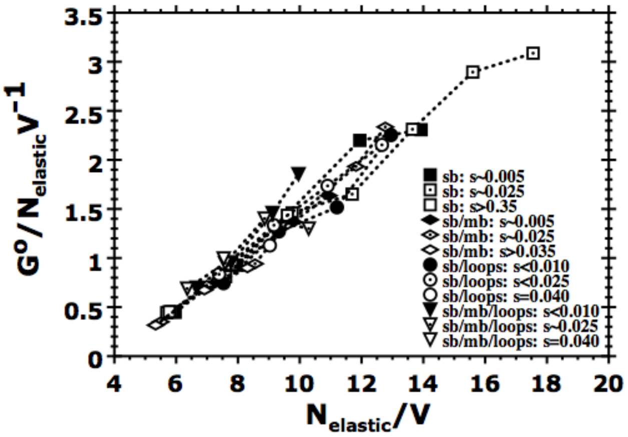

Figure 4.5: Plateau storage modulus from effective elastic bonds - Storage modulus G^0 normalized to the concentration of elastic linkers and as a function of the mean junction connectivity ν (twice the ratio of the number of junction-junction bonding interactions, with multiple bonds counted as one and intrajunction loops not counted, to the number of junctions). The data collapse approximately to a line.

directions each, were in good agreement with the results obtained from the full MD/MC trajectories via linear response theory, as represented by the agreement with the fitting curve reproduced from figure 4.4 (dotted line vs. circles). For the trivalent junction system, changes to the bond stiffness or the non-bonded interactions had a negligible influence on G^0 . These influences generally grew with increasing junction valence.

4.3.4 Stress relaxation rate

The ratio of the shear stress relaxation rate to the defect migration rate was expressed in the previous study using the quantity a. This relationship can be cast in the expression:

$$C_{\sigma\sigma}(t) = C_0 \left[\frac{N_L - a}{N_L}\right]^{p \cdot t/t_{MC}} = C_0 e^{-t/\tau_{shear}} \tag{4.8}$$

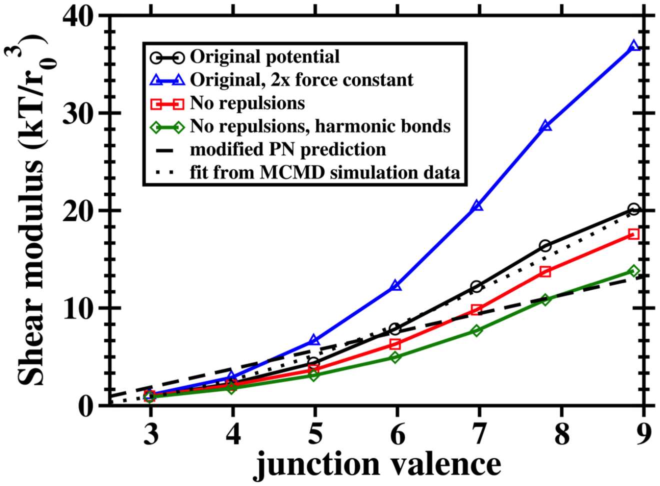

Figure 4.6: Magnitude of plateau storage modulus with form of interaction potential and from other considerations - Evolution of plateau shear modulus (G^0) vs. junction multiplicity (ν) with functional form of interacting potential and type of bonding/nonbonding contributions from simulations and predictions.

Equation 4.8 then is equivalent to $a = N_L t_{MC}/(p\tau_{shear})$. $N_L t_{MC}/p$ is the average residence time of a linker connecting two junctions in units of the MC attempt time, or half the average residence time τ_{bond} of a specific linker-junction bond. So, we can simply express a as half the ratio τ_{bond}/τ_{shear}. For singly bonded systems, we find a values somewhat greater than 3 for $\nu = 3$ and $a \sim 2$ up to $\nu = 9$.

4.4 Discussion

4.4.1 Network structure

The fraction of multiple bonds present in the system matched the prediction of a statistical formula based on random assignment of the ν bonds of a central junction to the $\nu \times N_R$ neighbors (figure 4.1). Trends in the percent of linkers that loop back to the same junction depended on whether multiple bonding was permitted (figure 4.2). With increasing valence, both the number of intramolecular junction sites and the number of intermolecular junction sites increase. When multiple bonding is allowed, these both increase linearly with ν and the loop fraction remains unaffected. When only single bonding is possible, each linker connected to a different junction eliminates the other sites on that junction, and so the number of possible inter-junction sites increases less steeply than the number of intra-junction sites, explaining the steady rise in the fraction of loops in this case.

4.4.2 Defect migration rate

In previous work,(22) we found that the probability p that a linker-junction dissociation event will be successful in producing a defect migration is proportional to the stoichiometric mismatch s at low s:

$$p = \frac{1}{2} s \nu N_R \tag{4.9}$$

where ν is the valency of the junctions and N_R is a measure of the mean number of neighboring junctions that are potential reattachment sites for the free linker site. The defect migration success probability p then levels off at higher s, where on average every junction is near one or more defect sites. The success probability increased with valence ν at fixed s, because the total number of available sites increase and the number of available sites in bonding range will also increase. Extending this analysis to $\nu = 9$, we see that above $\nu = 6$, when only single bonds are permitted, the increase with valence plateaus and is reversed (figure 4.3). The decrease comes from the fact that N_R decreases by 1 for each increase by 1 in ν. As v approaches the total number of neighbors, the fraction of those neighbors that are not already bonded to the original junction, and that are potential sites for a new bond, becomes small. On the other hand, when multiple bonds are permitted between any pair of junctions, empty sites on all neighbors are potential targets for a new bond, and p increases with valence. The possibility of loop formation opens up available defect sites on the same junction as potential targets for a new bond, and so also increases the defect migration success probability.

4.4.3 Trends in plateau modulus G^0

From MC/MD trajectory simulations, we have determined the plateau shear modulus (G^0) from the product of system volume with mean square of the average shear stress, averaged over fluctuations within the MD simulation time between defect migration attempts (eq. 4.3, 4.4). This shear stress reflects asymmetries in the fluctuating network topology, and corresponds to the ratio between stress and strain over time periods between local relaxation times and topological relaxation times. When local relaxation occurs much faster than changes in network topology, there is a plateau in the frequency-dependent storage modulus over intermediate frequencies, so the modulus of the fixed network (G^0) corresponds to the plateau modulus over this frequency range. (We do not treat the highest-frequency relaxation rate of these systems, as the model is not designed to treat these realistically.) We remind the reader that the plateau shear modulus is independent of the dynamics of bond rearrangement, and should represent an average **static** shear modulus for the network in the absence of bond dissociations or rearrangements.

Classical rubber theory (CRT) based on an assumption of independently extending Gaussian chains, predicts that:

$$G^0 = (N_L/V)k_BT \tag{4.10}$$

with N_L the number of linkers (exclusive of loops). Given that the linkers in the present simulation do not follow Gaussian chain statistics in their equilibrium extension distribution, there is no reason to expect adherence to the predictions of CRT or to the related phantom network (PN) model (30, 31) . In fact, for affine deformations of a set of linkers that follow a harmonic extension potential

$U(r) = (1/2)k(r - r_0)^2$, one can predict:

$$G^0 = (N_L/V)kr_0^2/15 \tag{4.11}$$

(see Appendix).The arguments used to derive the prefactor of $(1 - 2v^{-1})$ within the PN model (32) (which depends on the effective spring constants of springs in parallel and in series (33) are independent of the specifics of the spring constant, so one might expect to find:

$$G^0 = (1 - 2v^{-1})(N_L/V)kr_0^2/15 \tag{4.12}$$

which would give a linear increase starting from $\nu = 2 = 2N_L/N_J$. The increase in G^0 with N_L shown in figure 4.4 is plainly non-linear, even for the simplest case where no loops or multiple bonds are allowed.

The system parameters used for MD/MC calculations included non-bonded junction-junction interactions and non-linear linker extension potential. To investigate the effects of these interactions on G^0, we performed brief simulations of networks under shear strain using different sets of bonded and non-bonded interactions. Replacing the anharmonic potential with a harmonic potential of the same spring constant and minimum-energy bond length decreases G^0 (Fig.4.6, rhombi). The effect of the nonbonded repulsions is more subtle. By themselves they are not directly responsible for a large proportion of the shear stress; however, their presence shifts the bond length distribution away from r_0, adding stress to the linkers on average as the system is forced to satisfy packing and bond constraints simultaneously. Even with pure harmonic bonded interactions, there was a non-linear increase in G^0 with linker concentrations, and eq. 4.12 overpredicted the shear modulus over most of the range in valence.

As discussed by Plischke et al.(34) , simulated defective lattice networks linked by harmonic bonds that follow equation $U = (1/2)k(r - r_0)^2$ and have no angle-dependent potential exhibit a finite shear modulus that, near the percolation transition, is primarily entropic in origin. They find $G^0 \propto (\nu - \nu_{perc})^2$ over the range of mean valence v from the percolation limit $\nu_{perc} \sim 1.86$ to the defect-free lattice with $\nu = 6$. In contrast, defect lattice networks simulated by Nishi et al.(35) on a diamond lattice with a worm-like chain model bonds (similar to the Gaussian chain model at low extensions, but with finite extensibility) yielded good agreement with the PN model from $\nu = 2.4$ to the defect-free structure at $\nu = 4$, with $G^0 \propto (\nu - 2)$. There appears to be a qualitative difference in the relationship between the number of linkers and the elasticity for networks containing Gaussian chains and those containing linkers with a preference for a particular, non-zero extension. In the latter case, using the simple approximation G^0/k_BT for the concentration of effective chains may be misleading.

In the cubic network topologies studied in ref. 35, the contribution to linear shear modulus from bond stretching can be shown to equal zero exactly, even in the absence of defects ($\nu = 6$).(36) . In contrast, bond stretching does play a role in shear stiffness in the present simulations, even at a junction valence of $\nu = 4$ where there is a noticeable effect of linker spring force constant on G^0. Junction positions are sufficiently constrained within the disordered topologies formed during MCMD that bond lengths must be distorted to accommodate shear strain. The network shear modulus then becomes increasingly sensitive both to the stiffness of the bonded potential and to the presence of nonbonded junction-junction repulsions as valence increases (Fig. 4.6 upper triangles, squares).

The potential and the effective force constant associated with the junction-junction interaction scales proportionally to the number of bridging linkers, meaning that a double bond is twice as stiff as a single bond. For the trivalent junction system, changes to the bond stiffness or the non-bonded interactions had a negligible influence on G^0. At $\nu = 4$ and above, increasing the spring constant of the anharmonic potential increases G^0 to an increasing extent, reflecting the growing contribution of bond stretching to the shear response. These influences generally grew with increasing junction valence, as shown in figure 4.6 (upper triangles).

Figure 4.5 shows that networks simulated using MD/MC with single and multiple bonds with the same total number of bonds have similar G^0 ; this seems to imply that the contribution of each bond to the shear modulus is independent of its stiffness. We should point out that even though the fraction of linkers that are in multiple bonds rises as high as 50% (for $\nu = 9$) the fraction of $N_{elastic}$ that consists of multiple bonds is not above 25%. The effective valence of this system is about 6. In figure 4.6, it can be seen that doubling the stiffness of all the bonds in a system at $\nu = 6$ only increases G^0 by 50%. A simple prediction would be then that the $\nu = 9$ system with multiple bonds would have a shear stiffness that is about $(0.75 \times 1 + 0.25 \times 1.5) = 1.125$ time the value of G^0 for a system with $\nu = 6$ and all single bonds; this predicted difference of 12% is within the scatter of figure 4.5. So, we can conclude only that a double bond contributes significantly less to the shear stress than two single bonds in this type of linker-junction network, not that the contributions of double and single bonds are precisely equivalent.

4.4.4 Trends in shear stress relaxation time

The shear stress relaxation rate in the present model has an obvious connection to the defect migration rate, whose dependence on various factors was treated in depth in ref. 22, and appears to be predictable from the statistics of the defect sites available. The amount of stress relaxed per defect migration event, was also considered in the same reference, which (for single-bonded systems with $\nu = 3 - 5$) found that the TNT prediction stemming from classical rubber theory underpredicted this amount by a factor of more than 3 for $\nu = 3$ and a factor of more than 2 for $\nu = 4, 5$. The extension to $\nu = 9$ and the incorporation of multiple bonds and loops do not change the picture much, except to show that this factor remains near 2 at high valence (figure 4.7). The high value of a at $\nu = 4$ in the presence of multiple bonds might reflect that the presence of a double bond shifts the effective valence of a tetravalent junction from 4 towards 3.

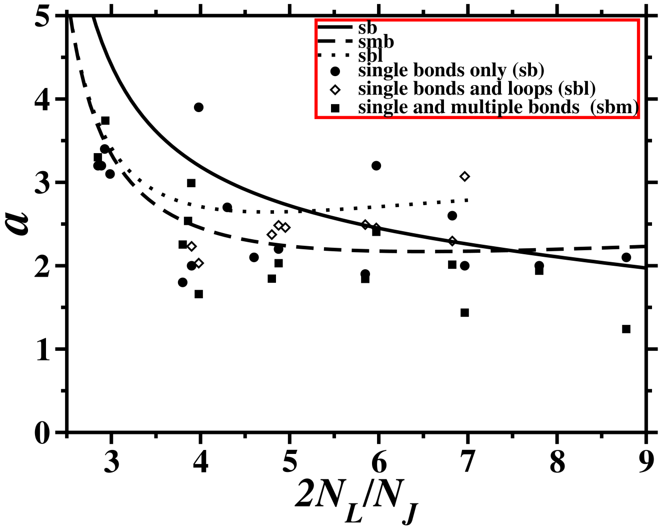

Figure 4.7: Apparent number of linkers relaxed per dissociation event - a vs. $2N_L/N_J$ from simulations (symbols) and predictions of equation 4.17 (solid curves)

Deviations from TNT are well documented in the literature. Modifications of TNT that incorporate the statistics of loop formation and super-bridges (junctions with only two connections to the network), along with the statistics of equilibrium self-assembly, have been used successfully to model linker concentration dependence of both shear relaxation time and plateau modulus. (8, 37) The current results, however, call for a different explanation, given that the findings hold even in the absence of loops and (at least for $\nu > 3$) in cases where super-bridges are negligible. The non-linear dependence of the plateau modulus on linker concentration calls into question the assumption that each linker carries on average a fraction $1/N_L$ of the stress. Here we propose that the observed trends in a, and the finding that $a > 2$ in these system, can be understood at least qualitatively by considering the dependence of the plateau modulus on the number of linkers.

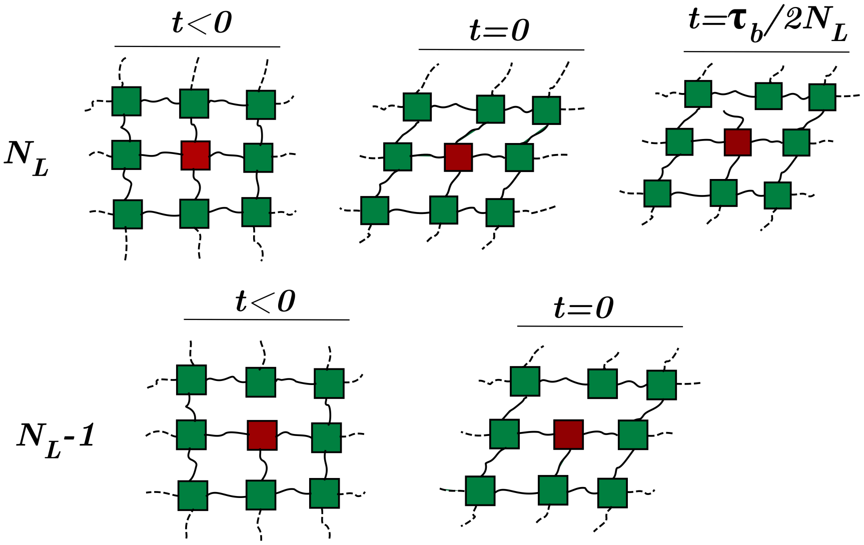

Figure 4.8: The equivalence of sub-networks ensemble assumption - Cartoon representation to explain equivalency of a $(N_L - 1, N_J)$ topology with missing linker due to pre-imposed stoichiometric mismatch and a (N_L, N_J) topology at the time of a first linker disconnecting from a perfectly matched reversible network

The cartoons in figure 4.8 are useful to explain this relationship. Consider a material containing N_J junctions with N_L linkers, originally under zero shear stress, subject at time $t = 0$ to an instantaneous shear strain step γ. Assuming that the intra-chain relaxation time is instantaneous, the stress $\sigma(0)$ at time $t = 0$ then equals $G_0\gamma$ where G_0 represents the plateau modulus. The linker-junction bond dissociation process is assumed to be stochastic and first-order with a characteristic bond lifetime τ_{bond} that is independent of applied strain; after a time $\Delta t = \tau_{bond}/(2N_L)$, one linker on average will have dissociated. In the current simulations, we have ensured that the dangling end reattaches to a new junction site immediately, but in the general case the dissociated end may instead remain unattached, as in the cartoon. After its initial dissociation, the linker is assumed to relax at the current strain state, and will no longer contribute (on average) to the current shear stress whether it reattaches or not. Therefore, the shear stress at time Δt can be attributed to the stress from the sub-network of $N_L - 1$ linkers that persist in their original connections from before the strain was applied. It is evident that the stress from this sub-network corresponds to the *initial* stress (before any linkers dissociate) upon a shear strain of the same magnitude in a network having the same network topology, but missing one linker at the point of the dissociation event. That is,

$$\sigma_{N_L,N_J}(\Delta t) = \sigma(0)_{N_L-1,N_J} \tag{4.13}$$

The change in shear stress over time in the transient network can thus be related to the change in stress of a fixed network associated with a change in network structure:

$$\sigma_{N_L,N_J}(t = \tau_B/(2N_L)) - \sigma_{N_L,N_J}(t = 0) = \sigma(0)_{N_L-1,N_J} - \sigma(0)_{N_L,N_J} \tag{4.14}$$

Converting the differences into differentials gives:

$$\left(\frac{\partial \sigma}{\partial t}\right)_{N_L,N_J,\gamma} \times \frac{\tau_B}{2N_L} = \left(\frac{\partial \sigma(t=0)}{\partial N_L}\right)_{N_J,\gamma} \tag{4.15}$$

Then, assuming a single exponential decay in stress with time constant τ_{shear}, dividing both sides by strain $\gamma = \sigma(0)/G_0$, yields

$$-\frac{G^0}{\tau_{shear}}\frac{\tau_B}{2N_L} = -\left(\frac{\partial G^0}{\partial N_L}\right)_{N_J,\gamma} \tag{4.16}$$

(Dividing through by volume yields eq. 4.1.) This equation is rigorous for the shear moduli G^0 of the specific pair of network topologies that differ by the presence or absence of one particular linker (as, for instance, the pair in figure 4.8). To make a useful comparison with experiment or simulation, we must substitute the thermal ensemble averages of G^0 over all topologies with N_L or $N_L - 1$ linkers; the nature of this approximation introduced in so doing will be considered below.

To cast this relation in terms of the system properties determined in the present simulations, we substitute the mean valence $\nu = 2N_L/N_J$ and $a = (\tau_{bond}/\tau_{shear})$ and find:

$$a = \frac{\nu}{G^0}\left(\frac{\partial G^0}{\partial N_L}\right)_{N_J,V} \tag{4.17}$$

Predicted values of a using equation 4.17 and simulation values for a with increasing n are shown in figure 4.7. In simulation, across all systems $a \sim 2$ with slightly higher a values in networks having loops or lower degree of stoichiometric mismatch. The scatter data points with highest values in a for $\nu > 3$ correspond to cases of very low stoichiometric mismatch and very low defect migration success probability; as discussed previously,(22) in such systems there is a strong selection bias for the most highly stressed linkers to participate in defect migration events. Systems with multiple bonding tend to give lower values of a.

Using the empirical fits for G^0 shown in figure 4.4, we have used eq. 4.17 to calculate a vs. ν for three systems and see qualitative agreement with the simulation data. The poor ability of the simple polynomial fits to reproduce the derivative of G^0 with respect to ν may account for some of the deviation, especially near $\nu = 3$ and $\nu = 9$. Equation 4.17 overpredicts the rate of stress relaxation, but still gives a better approximation than the TNT theory result $a = 1$. The cases where it underpredicts the rate of stress relaxation are for singly-bonded networks at the lowest defect fractions, where the probability of linker end reattachment to its original junction is very high and p is very low. As discussed previously,(22) at low p the most high-energy, highly-stressed linkers are disproportionately likely to undergo successful bond reassignment, and thus each defect migration event carries a disproportionate amount of stress.

4.4.5 Implications of equation 4.1

Note that in a defect-free network where CRT holds, $G^0 = c_L k_B T$, and the TNT is recovered: $\tau_{shear} = \tau_b/2$ and $a = 1$. In a defect-free linker-junction network where shear modulus obeys the PN relationship, i.e. $G^0 = (c_L - c_J)k_B T$, eq.4. 1 yields:

$$\tau_{shear} = (1 - c_J/c_L)\tau_b/2 \tag{4.18}$$

More generally, if the plateau modulus follows a power law $G^0 \propto (c_L - c_{perc})^\alpha$ near the percolation threshold c_{perc} ,τ_{shear} is predicted to follow:

$$\tau_{shear} = \tau_b(1 - c_{perc}/c_L)/2\alpha \tag{4.19}$$

Viscosity would then scale as $(c_L - c_{perc})^{\alpha+1}/c_L$. This functional form is at least grossly consistent with the sharp rise and plateau typically observed in τ_{shear} near the percolation transition. The proposed relationship, eq. 4.1, is potentially useful in that it provides a means to estimate a microscopic relaxation time τ_b from knowledge of the concentration dependence of G^0 and τ_{shear}, even close to percolation where τ_{shear} changes rapidly.

4.4.6 Assumptions underlying eq. 4.1

First, we have assumed that the presence of a dangling linker does not contribute to the shear stress. The junction-linker bond energy is presumed to be independent of the number of other linkers attached to the junction. We have assumed that removing one linker from the system and allowing the system to reach equilibrium will reduce the mean number of *bridging* linkers by one, which would seem to be inconsistent with any structure that has an appreciable fraction of defects. The relationship 4.17 will, in fact, hold under a less stringent approximation, that

$$\frac{\partial N_{L,bridge}}{\partial N_L} = \frac{N_L, bridge}{N_L} \tag{4.20}$$

If eq. 4.20 holds, then $c_L(\partial G^0/\partial c_L) = c_{L,bridge}(\partial G^0/\partial c_{L,bridge})$. Eq. 4.20 will be approximately true over much of the linker concentration range, so long as the defect proportions do not change too rapidly with concentration. This approximation will break down when linkers and junctions are near stoichiometric balance, and adding a linker to the system will decrease the number of open junction sites while increasing the number of dangling linkers, leading to no net change in $c_{L,bridge}$.

The most subtle approximation is that the ensemble of network topologies created by the disconnection of one end of a linker-junction bond has the same shear modulus as the equilibrium ensemble of network topologies formed upon the removal of a bridging linker while keeping the number of junctions fixed. One can define the set of topologies of the system characterized by a certain N_L and N_J as a set of lists of bonding pairs (i, j) where i and j are the linker and junction indices respectively, and where a given i can appear no more than 2 times in the list and a given j can appear no more than ν times in the list. Any (N_L, N_J) topology from which the appearance of $i = N_L$ is eliminated is a valid $(N_L - 1, N_J)$ topology. The approximation is that the set of these topologies (with probability weightings reflecting the free energies of their parent (N_L, N_J) topologies) has the same average shear modulus as the thermal ensemble of $(N_L - 1, N_J)$ topologies. These two ensembles will be similar in terms of the numbers of bridging linkers and defects (loops, vacancies, and dangling ends) of various sorts; they will differ primarily in that the pairs of vacant sites formed from the removal of one end of a linker from the N_L-linker system are spatially correlated while in the ensemble of $N_L - 1$ topologies the vacant site defects are distributed randomly.

Note that a mapping between the ensemble of transiently disjoined N_L-linker networks and the ensemble of $(N_L - 1)$-linker topologies has been discussed so far only in the context of linker-junction systems, because every linker that is removed leaves junction site defects that have no way of recombining. It is worth considering to what extent eq. 4.1 may apply to single-component end-linking telechelic associating polymer networks. In such systems, the junction is a self-assembled aggregate or micelle of linker ends. The number of junctions is determined by a dynamic equilibrium. Decreasing the number of linkers in such a network may or may not produce topologies that resemble the transiently dissociated network, because the number of nodes can adapt. For instance, in case of a strong structural preference for a certain number of linkers per node, the system could maintain constant multiplicity of all junctions over a wide linker concentration range. In such a case, changing the linker concentration would produce a system with fewer junctions but the same multiplicity, whereas the stress remaining after a series of transient dissociation and reattachment events would be determined by the properties of a sub-network with the same number of junctions and fewer linkers per junction. To the extent that the shear modulus depends on the distribution of valence multiplicities, and not just the number of bridging linkers, such a system would show deviations from eq. 4.1.

4.5 Conclusions

In this report we expanded our previous analysis of stress relaxation in protein networks with defects to include higher valency networks with junction multiplicity (ν) in the range six to nine. We have considered systems in which linkers may loop and/or in which multiple linkers can bridge the same pair of junctions. The fraction of multiple junction pairings can be predicted from a simple probability model by considering the number of junction sites available for each mode of bonding between pairs of junctions. Higher loop fraction with valence was observed in networks with only single bonding from crowding effect. We also explored the changes in rate of defect migration with changing the network structures. The defect migration success probability (p) increases with valency at fixed degree of stoichiometric mismatch when only single bonding between pairs of junctions is allowed. The values of p decrease with valence in absence of multiple bonding at same defect ratio as most first shell junction neighbors are already bonded (crowding effect). The migration rate (p) is increased by the presence of loops and multiple bonding as there are more sites accessible for the disconnected linker to connect to upon its dissociation.

The dependence of plateau modulus on junction valence strongly deviates from the Gaussian chain and phantom network model predictions of a linear relationship of G^0 in concentration of linkers, or from a new formula for G^0 that is based on affine deformations of independent linkers. The roughly quadratic dependence observed is consistent with previous simulations of a similar system, a defective cubic lattice whose vertices are linked by tethers with a preferred bonding distance.[11] Where multiple bonding was investigated, it was seen that each linker involved in multiple bonding contributes significantly less to G^0 compared to a lone linker connecting a pair of junctions.

In this set of simulations, the shear relaxation time, τ_{shear} is still dependent on defect fraction and reduced by loops and multiple bonding due to an increase in defect migration rates. The proportional share of stress relieved by each defect migration event, denoted a, was seen to maintain a value near 2 even as junction valence climbed to 9. A formula to relate τ_{shear} to the dependence of G^0 on valence is derived from considering the equivalence between a network that has undergone a linker dissociation event after shear strain and a network in which that linker was never present. The proposed relationship is however expected to fail in nearly stoichiometrically matched networks due to a high likelihood of forming dangling bonds rather than adding N_L elastic linkers capable to support stress. The general material properties such as plateau modulus G^0, its non-linear observed dependence in number of linkers (N_L), and the relaxation time τ_{shear} were related to the microscopic timescale τ_{bond}. In simulation a, the apparent number of linkers relaxed by the defect migration move remains 2 as valence increases.

4.6 Appendix

4.6.1 Affine deformation approximation for shear modulus of center-force Hookean network

We derive a bulk shear modulus for a network consisting of springs with potential:

$$U(r) = \frac{1}{2}k(r - r_0)^2 \qquad (A1)$$

which is an approximation to the quartic potential defined in Eq. 4.2. Each linker end-to-end vector in the unstrained system is represented as:

$$r = (r_x, r_y, r_z) = (r_o sin\theta cos\phi, r_o sin\theta sin\phi, r_o cos\theta) \qquad (A2)$$

Under an affine shear deformation γ in the $x - y$ plane, $\Delta r_x = \gamma r_y$ and each linker vector is distorted to:

$$r = (r_x, r_y, r_z) = (r_o sin\theta cos\phi + \gamma r_o sin\theta sin\phi, r_o sin\theta sin\phi, r_o cos\theta) \qquad (A3)$$

To first order in γ, the change in linker distance is:

$$\Delta \left|r\right| = \frac{1}{2}r_o \gamma sin^2\theta sin(2\phi) \qquad (A4)$$

Approximating the linker length distribution around r as a delta function at r_0, plugging Eq. (A4) into (A1) and averaging over orientations yields:

$$\langle U \rangle_{\gamma} = \frac{1}{2} k r_0^2 \frac{\gamma^2}{4} \frac{1}{4\pi} \int_0^{\pi} sin^5\theta \int_0^{2\pi} sin^2(2\phi) d\theta d\phi = \frac{k r_0^2 \gamma^2}{30} \qquad (A5)$$

Taking a volume element with dimensions $L_x \times L_y \times L_z$, containing N_L linkers, the shear modulus can be obtaines as the ratio of shear stress (force per area) to shear strain:

$$G = \frac{\sigma_{xy}}{\gamma_{xy}} = \frac{N_L}{A\gamma_{xy}} \cdot \frac{d < U >_{\gamma_{xy}}}{d\Delta x} = \frac{N_L}{L_X L_Z} \cdot \frac{d < U >_{\gamma_{xy}}}{d\gamma_{xy}} \cdot \frac{d\gamma_{xy}}{d\Delta x} = \frac{N_L}{L_X L_Z L_Y} \cdot \frac{d < U >_{\gamma_{xy}}}{d\gamma_{xy}} = \frac{N_L k r_o^2}{15V}$$

$$(A6)$$

References

[1] Sebastian Seiffert and Joris Sprakel. Physical chemistry of supramolecular polymer networks. *Chem. Soc. Rev.*, 41:909–930, 2012. 75

[2] Constantinos Tsitsilianis. Responsive reversible hydrogels from associative ”smart” macromolecules. *Soft Matter*, 6(11):2372–2388, 2010. 75

[3] M. Rubinstein and N Alexander, Semenov. Dynamics of entangled solutions of associating polymers. *Macromolecules*, 34:1058–1068, 2001. 75

[4] M. Rubinstein and A. N. Semenov. Thermoreversible gelation in solutions of associating polymers: 2. linear dynamics. *Macromolecules*, 31:1386–1397, 1998.

[5] A. N. Semenov and M. Rubinstein. Thermoreversible gelation in solutions of associative polymers. 1. statics. *Macromolecules*, 31:1373–1385, 1998.

[6] L. G. Baxandall. Dynamics of reversibly crosslinked chains. *Macromolecules*, 22(4):1982–1988, 1989.

[7] M.E. Cates. *Macromolecules*, 20(9):2289–2296, 1987.

[8] Tom Annable, Richard Buscall, Rammile Ettelaie, and D Whittlestone. *Journal of Rheology*, 37:695–726, 1993. 95

[9] R. J.J. Jongchaap, R.H.W. Wintjes, M.H.G. Duits, and J. Mellema. A

generalized transient network model for associative polymer networks. *Macromolecules*, 34:1031–1038, 2001.

[10] James T. Kindt. Simulation and theory of self-assembly and network formation in reversibly cross-linked equilibrium polymers. *The Journal of Chemical Physics*, 123(14):144901–11, 2005.

[11] Robert S. Hoy and Glenn H. Fredrickson. Thermoreversible associating polymer networks. i. interplay of thermodynamics, chemical kinetics, and polymer physics. *The Journal of Chemical Physics*, 131(22):224902, 2009.

[12] L. Leibler, M. Rubinstein, and R. Colby. Dynamics of reversible networks. *Macromolecules*, 24:4701–4707, 1991.

[13] A.S. Lodge. A network theory of flow birefringence and stress in concentrated polymer solutions. *Trans. Faraday Soc.*, pages 120–139, 1956.

[14] A. S. Lodge. Constitutive equations from molecular network theories for polymer solutions. *Rheologica Acta*, 7(4):379–392, 1968.

[15] Fumihiko Tanaka. Thermoreversible gelation of associating polymers. *Physica A: Statistical Mechanics and its Applications*, 257:245–255, 1998.

[16] F. Tanaka and S. F Edwards. Viscoelastic properties of physically crosslinked networks. transient network theory. *Macromolecules*, 25:1516–1523, 1992.

[17] F. Tanaka and S. F Edwards. *J. Non-Newtonian Fluid Mech.*, 43:247–271, 273–288,289–309, 1992.

[18] F. Tanaka and T. Koga. Intramolecular and intermolecular association in thermoreversible gelation of hydrophobically modified associating polymers. *Computational and Theoretical Polymer Science*, 10:259–267, 2000.

[19] R.H.W. Wintjes, R. J.J. Jongchaap, M.H.G. Duits, and J. Mellema. A new transient model for associative polymer networks. *Journal of Rheology*, 43(2):375–391, 1999.

[20] Misazo Yamamoto. The visco-elastic properties of network structure i. general formalism. *Journal of the Physical Society of Japan*, 11(4):413–421, 1956.

[21] Misazo Yamamoto. The visco-elastic properties of network structure ii. structural viscosity. *Journal of the Physical Society of Japan*, 12(10):1148–1158, 1957.

[22] A. West and J. T. Kindt. Effects of defects on the shear relaxation in self-assembled protein networks. *Soft Matter*, 8:2895–2906, 2012. 76, 79, 85, 90, 98

[23] A. Kaye. *Brit. J. Appl. Phys.*, 17:803–806, 1966.

[24] Tstutomu Indei. Rheological study of transient networks with junctions of limited multiplicity. ii. sol/gel transition and rheology. *The Journal of Chemical Physics*, 127:144905, 2007.

[25] Daniel Vernon and Michael Plischke. Viscoelasticity near the gel point: A molecular dynamics study. *Phys. Rev. E.*, 64:031505–1–031505–5, 2001.

[26] Tsutomu Indei, JayD Schieber, and Jun-ichi Takimoto. Effects of fluctuations of cross-linking points on viscoelastic properties of associating polymer networks. *Rheologica Acta*, 51(11-12):1021–1039, 2012. 75

[27] Congqi Yan and Darrin J. Pochan. Rheological properties of peptide-based hydrogels for biomedical and other applications. *Chem. Soc. Rev.*, 39:3528–3540, 2010. 76

[28] Minkyu Kim, Shengchang Tang, and Bradley D. Olsen. Physics of engineered protein hydrogels. *Journal of Polymer Science Part B: Polymer Physics*, 51(7):587–601, 2013. 76

[29] Cheryl T. S. Wong Po Foo, Ji Seok Lee, Widya Mulyasasmita, Andreina Parisi-Amon, and Sarah C. Heilshorn. Two-component protein-engineered physical hydrogels for cell encapsulation. *Proceedings of the National Academy of Sciences*, 106(52):22067–22072, 2009. 76

[30] Hubert M. James. Statistical properties of networks of flexible chains. *The Journal of Chemical Physics*, 15(9):651–668, 1947. 91

[31] Hubert M. James and Eugene Guth. Theory of the increase in rigidity of rubber during cure. *The Journal of Chemical Physics*, 15(9):669–683, 1947. 91

[32] P. J. Flory, M. Gordon, and N. G. McCrum. Statistical thermodynamics of random networks [and discussion]. *Proceedings of the Royal Society of London. A. Mathematical and Physical Sciences*, 351(1666):351–380, 1976. 92

[33] M. Rubinstein and R. Colby. *Polymer Physics.* Oxford University Press Inc., New York, 2003. 92

[34] M. Plischke, D. C. Vernon, B. Joós, and Z. Zhou. Entropic rigidity of randomly diluted two- and three-dimensional networks. *Phys. Rev. E*, 60:3129–3135, 1999. 92

[35] Kengo Nishi, Masashi Chijiishi, Yukiteru Katsumoto, Toshio Nakao, Kenta Fujii, Ung il Chung, Hiroshi Noguchi, Takamasa Sakai, and Mitsuhiro Shibayama. Rubber elasticity for incomplete polymer networks. *The Journal of Chemical Physics*, 137(22):224903, 2012. 93

[36] Shechao Feng and Pabitra N. Sen. Percolation on elastic networks: New exponent and threshold. *Phys. Rev. Lett.*, 52:216–219, 1984. 93

[37] Paulina J. Skrzeszewska, Frits A. de Wolf, Marc W. T. Werten, Antoine P. H. A. Moers, Martien A. Cohen Stuart, and Jasper van der Gucht. Physical gels of telechelic triblock copolymers with precisely defined junction multiplicity. *Soft Matter*, 5:2057–2062, 2009. 95

5

Introduction to elasticity of lipid bilayer edge work

5.1 Background

A lipid membrane creates a selective diffusion barrier between the interior and the exterior of a cell. The first description of this thin interface as a lipid bilayer assembly dates back to 1925 to work by Gorter and Grendal. (1) A new picture for the structure of cell membrane was introduced in 1972 by Singer and Nicholson (2) known as the fluid-mosaic model and also shows the embedded proteins. Our understanding of lipid bilayers and lipid self-assembly evolved significantly since this simple picture was postulated. The lipid bilayers and lipid structures found in cells are very dynamic systems. As facilitators of vital cellular processes such as fusion, fission, endocytosis, and exocytosis, lipid membranes must stretch, compress, bend, break, self-repair, or re-pack in smaller size structures of unusual and ill-defined shapes. Describing both the elastic behavior of lipid structures undergoing such processes and the lipid conformations that individual molecules must adopt during such instances via simulations and theory methods is thoroughly fascinating.

The research introduced here investigates the magnitude of force acting at the lipid bilayer edge to close macroscopic size pores ($\sim \mu m$ in diameter). This force is tangent to the edge, has a pN magnitude, and it is called edge tension (Λ). The conformational change in lipids packed at the bilayer edge compared to intact bilayers is also investigated.

Very many types of lipid molecules have been identified across living systems. Lipid composition affects both the structure and the elastic properties of self-assembled lipid structure. For example in mammalian cells the composition of lipid bilayers consists of various lengths fatty acids (a.k.a lipid tails) attached via a glycerol backbone to a hydrophilic head group molecule of the type phosphatidylcholine (PC), phosphatidylethanolamine (PE), phosphatidylinositol (PI), and phosphatidylserine (PS) (3). Sphyngolipids such as sphyngomyelin and glycosphingolipids along with sterol molecules such as cholesterol are also present. Various classes of interfacial and integral proteins proteins are included within the lipid bilayers. Proteins allow the passing of small molecules; proteins serve as receptors during recognition events; proteins host important reactions. The incorporation of proteins modifies the local lipid bilayer properties such as increase its curvature and disrupts the ordering of lipid tail packing. Other cell non-native inclusions such as incorporated quantum dots are also expected to affect the structure and modify the local lipid bilayer conformation.

The size of lipid headgroup is an important consideration in lipid bilayer studies when investigating configurational properties of self-assembled structures. A guiding principle in predicting the geometric shape of the resulting self-assembled structures is the packing parameter (4) (p) , a simple geometric criteria defined as ratio of volume (v) of one lipid to length of hydrocarbon lipid tail length (l) and optimum head group area (a_o) : $p = v/(la_o)$. A packing parameter of ~ 1 corresponds to forming a planar bilayer and $p \sim 1/3$ corresponds to forming spherical micelles.

A strength of simulation as method of scientific investigation is the ability to precisely control a system's composition. Models of lipid bilayers implemented in simulation typically consist of a single component lipid. In all systems investigated in this work, the PC headgroup is used and lipid tail lengths ranging from 12-18 carbons with at most one double bond per tail. The self-assembled structure that results is the lipid bilayer configuration ($p \sim 1$).

The elastic properties of macroscropic pores have been previously studied in single PC lipid component giant unimellar vesicles (GUVs) structure (5–9). Typical experiments consist in assembling the lipid of interest into a GUV structure, instilling a pore into the lipid bilayer by a method such as an electric pulse, or the action of a laser beam, and then following the dynamics of re-sealing the bilayer via (fluorescence) microscopy techniques. The theoretical frameworks that accompany many of these experiments was developed by Brochard and Wyart[6]. The evolution of such a pore is controlled by the action of two forces, the surface tension (γ) defined as force per edge unit length acting to expand the pore and the edge tension force mentioned previously attempting to eliminate the pore. We mention that the ratio of surface tension (γ) to edge tension (Λ), Λ/γ corresponds to an important length scale (R) in lipid bilayer edge elasticity-pores with size larger than this value grow indefinitively and those with smaller size than R can re-seal leading to an intact bilayer.

In experiments the magnitude of edge tension was found affected by both the length of lipid tail used to form the GUV and by the presence of non-lipid molecules at the edge. The edge tension of a PC lipid with twelve carbons connected as saturated tails was recently reported as 2.5 pN. (7) The edge tension of a PC lipid with eighteen carbons and one double bond per tail was 27.7 pN. (8) For the same and other PC lipid systems the edge tension values tend to depend significantly on the experimental method used to investigate edge tension.(5, 10, 11) Molecules with negative spontaneous curvature such as cholesterol raise edge tension values and detergent molecules with large headgroups lower the edge tension. (5)

The edge tension and lipid conformation at the edge was characterized in theory and simulation. Molecular elasticity theories consider the geometry of the lipid bilayer with macroscopic pores to correspond to a hemi cylindrical geometric shape assembly. (12–14) The starting point in understanding the nature of self-assembly of lipids in these theories is the opposing force-model (OFM) of Israelachvilli (4). When a lipid structure changes its geometric shape such as it bends or stretches in response to an applied perturbation (such as forming an edge), a new headgroup area (a) characterizes the new assembly. The lipid tails might also contort to new configurations. The value of a is determined by two competing forces acting at the level of hydrocarbon-hydrophilic interfacial region, an attractive interfacial hydrophobic force and a headgroup repulsion force.

According to the OFM formalism the resulting molecular free energy per molecule in a lipid assembly or aggregate is given by :

$$f = \gamma \cdot a + K/a \tag{5.1}$$

The first term is an attractive energy term with γ surface tension at the hydrocarbon-water interfacial region and the second term is a repulsive energy due to steric/electrostatic head-group repulsions. The constant K is lipid molecule specific as to allow variations in the headgroup size and shape.

Within the OFM model, assuming a second order Taylor expansion of free energy around the planar bilayer headgroup area a_o:

$$df(a_0) = \frac{1}{2} f''(a_0)\,(a_{edge} - a_0)^2 \tag{5.2}$$

Also considering that $a_0 = (K/\gamma)^{1/2}$ and $K_a \sim 2\gamma$ for a monolayer, as well as a hemicylinder edge lipid packing geometry ($a_{edge} = 2a_0$), leads to the edge tension quantity having the formula:

$$\Lambda = df \cdot \rho_{edge} = \frac{\pi h K_a}{16} \tag{5.3}$$

with f the molecular free energy, ρ_{edge} the edge lipid density, h is the intact monolayer thickness, K_a the area compressibility modulus, and a_{edge} the edge area per lipid. The optimum area per headgroup a_o and the bilayer thicknesses (h) of PC lipids of tail lengths investigated in this work have been previously presented from experiment and simulation. (15–24) Area compressibility moduli K_a have also been studied in simulation and experiments. (25–28)

The lipid density at edge is given by:

$$\rho_{edge} = \frac{\pi\left(h/2\right)^2}{2v} = \frac{\pi h}{4a_o} \tag{5.4}$$

with v the lipid tail volume.

Other theoretical work for example one of May's studies referenced above(13) includes an additional term in the free energy per molecule due to assuming changes in conformations of lipid tails. We also point out that equation 5.3 only considers a lipid structure stretching contribution to resulting edge tension. The formation of bilayer edge from monolayer bending elasticity is considered to also play a role in edge formation and the magnitude of edge tension from such considerations has also been presented (29) .

The edge tension and pore formation in lipid bilayers has also been studied in simulations. One class of such investigations focused on calculating the edge tension of nm size circular pores of lipid bilayers during their earliest formation stage. Example studies from this category include investigating the minimum stable pore radius, the corresponding bilayer surface tension, and characterization of pore shape(30), the free energy profile as function of pore radius(29), and the free energy barrier associated with initiating a pore (31).

Recent experiments of Smith and co-workers (32) attempted to characterize the behavior of edge pore lipids in experiment. The presence of edge is believed to affect the lipid molecule diffusion constants near the edge, and to also affect the onset of lipid tail phase transition. Lipid simulations methodologies have been previously developed to study both the magnitude of edge tension and also the packing of lipids at the edge at a nm length scale resolution (11, 33).

Kindt and co-workers using the ribbon geometry implementation investigated the edge tension associated with m size pore in simulation. The process of edge formation in ribbon geometry and the edge tension from atomistic resolution ribbon simulations (5-20 ns long) were also reported (11). While the $\sim$ pN order of magnitude of edge tension was also confirmed in this set of simulations, longer simulations were recommended to use in order to attain well converged values with changing the lipid type. Other coarse-grain and atomistic related studies included investigating the effect of lipid composition on edge structure and magnitude of edge tension as well as the role of thermal fluctuations in affecting the edge tension. (34–36)

References

[1] E.F. Gorter and F. Grendel. On biomelecular layers of lipoids on chromacytes of blood. *J. Exp. Med.*, 41:439–443, 1925. 109

[2] S.J. Singer and G.L. Nicolson. The fluid mosaic model of the structure of cell membrane. *Science*, 175:720–731, 1972. 109

[3] G. van Meer and A. I. P.M. Kroon. Lipid map of the mammalian cell. *Journal of Cell Science*, 124:5–8, 2011. 110

[4] J. N. Israelachvili. *Intermolecular and Surface Forces.* Acamdemic Press, New York, 1992. 110, 112

[5] O. Sandre H. Guitouni Karatekin, E., P.-H. Puech N. Borghi, and F. Brochard-Wyart. Cascade of transient pores in giant vesicles: line tension and transport. *Biophys. J.*, 84:1734–1749, 2003. 111

[6] F. Brochard-Wyart, P. G. de Gennes, and O. Sandre. Transient pores in stretched vesicles: role of leak-out. *Physica A: Statistical Mechanics and its Applications*, 278:32–51, 2000.

[7] Narayanan Srividya and Subra Muralidharan. Determination of the line tension of giant vesicles from pore-closing dynamics. *The Journal of Physical Chemistry B*, 112(24):7147–7152, 2008. 111

[8] T Portet and R Dimova. A new method for measuring edge tensions and stability of lipid bilayers: Effect of membrane composition. *Biophys. J.*, 99:3264–3273, 2010. 111

[9] Doncho V. Zhelev and David Needham. Tension-stabilized pores in giant vesicles: determination of pore size and pore line tension. *Biochimica et Biophysica Acta (BBA) - Biomembranes*, 1147(1):89–104, 1993. 111

[10] I. Genco, A. Gliozzi, A. Relini, M. Robello, and E. Scalas. Electroporation in symmetric and asymmetric membranes. *Biochimica et Biophysica Acta (BBA) - Biomembranes*, 1149(1):10–18, 1993. 111

[11] Frank Y. Jiang, Yann Bouret, and James T. Kindt. Molecular dynamics simulations of the lipid bilayer edge. *Biophysical Journal*, 87(1):182–192, 2004. 111, 114

[12] R. J. Molotkovsky and S. A. Akimov. Calculation of line tension in various models of lipid bilayer pore edge. *Biochemistry (Moscow) Supplement Series A: Membrane and Cell Biology*, 3(2):223–230, 2009. 112

[13] May. A molecular model for the line tension of lipid membranes. *Eur. Phys. J. E*, 3:37–44, 2000. 113

[14] S. May, Y. Kozlovsky, A. Ben-Shaul, and M.M. Kozlov. Tilt modulus of a lipid monolayer. *Eur. Phys. J. E*, 14:299–308, 2004. 112

[15] Norbert Kucerka, Jana Gallov, Daniela Uhrkov, Pavol Balgav, Monica Bulacu, Siewert-Jan Marrink, and John Katsaras. Areas of monounsaturated diacylphosphatidylcholines. *Biophysical Journal*, 97(7):1926–1932, 2009. 113

[16] Norbert Kucerka, Yufeng Liu, Nanjun Chu, Horia I. Petrache, Stephanie Tristram-Nagle, and John F. Nagle. Structure of fully hydrated fluid phase dmpc and dlpc lipid bilayers using x-ray scattering from oriented multilamellar arrays and from unilamellar vesicles. *Biophysical Journal*, 88(4):2626–2637, 2005.

[17] Norbert Kucerka, John F. Nagle, Jonathan N. Sachs, Scott E. Feller, Jeremy Pencer, Andrew Jackson, and John Katsaras. Lipid bilayer structure determined by the simultaneous analysis of neutron and x-ray scattering data. *Biophysical Journal*, 95(5):2356–2367, 2008.

[18] N. Kucerka, S. Tristram-Nagle, and J. F. Nagle. Structure of fully hydrated fluid phase lipid bilayers with monounsaturated chains. *The Journal of membrane biology*, 208(3):193–202, 2005.

[19] David Poger and Alan E. Mark. On the validation of molecular dynamics simulations of saturated and cis-monounsaturated phosphatidylcholine lipid bilayers: A comparison with experiment. *Journal of Chemical Theory and Computation*, 6(1):325–336, 2009.

[20] David Poger, Wilfred F. Van Gunsteren, and Alan E. Mark. A new force field for simulating phosphatidylcholine bilayers. *Journal of Computational Chemistry*, 31(6):1117–1125, 2010.

[21] Jeffery B. Klauda, Richard M. Venable, J. Alfredo Freites, Joseph W. OConnor, Douglas J. Tobias, Carlos Mondragon-Ramirez, Igor Vorobyov, Alexander D. MacKerell, and Richard W. Pastor. Update of the charmm all-atom additive force field for lipids: Validation on six lipid types. *The Journal of Physical Chemistry B*, 114(23):7830–7843, 2010.

[22] Chris Oostenbrink, Alessandra Villa, Alan E. Mark, and Wilfred F. Van Gunsteren. A biomolecular force field based on the free enthalpy of hydration and solvation: The gromos force-field parameter sets 53a5 and 53a6. *Journal of Computational Chemistry*, 25(13):1656–1676, 2004.

[23] O. Berger, O. Edholm, and F. Jhhnig. Molecular dynamics simulations of a fluid bilayer of dipalmitoylphosphatidylcholine at full hydration, constant pressure, and constant temperature. *Biophysical Journal*, 72(5):2002–2013, 1997.

[24] See-Wing Chiu, Sagar A. Pandit, H. L. Scott, and Eric Jakobsson. An improved united atom force field for simulation of mixed lipid bilayers. *The Journal of Physical Chemistry B*, 113(9):2748–2763, 2009. 113

[25] Qaiser Waheed and Olle Edholm. Undulation contributions to the area compressibility in lipid bilayer simulations. *Biophysical Journal*, 97(10):2754–2760, 2009. 113

[26] Erik Lindahl and Olle Edholm. Spatial and energetic-entropic decomposition of surface tension in lipid bilayers from molecular dynamics simulations. *The Journal of Chemical Physics*, 113(9):3882–3893, 2000.

[27] Derek Marsh. Elastic curvature constants of lipid monolayers and bilayers. *Chemistry and Physics of Lipids*, 144(2):146–159, 2006.

[28] W. Rawicz, K. C. Olbrich, T. McIntosh, D. Needham, and E. Evans. Effect of chain length and unsaturation on elasticity of lipid bilayers. *Biophysical Journal*, 79(1):328–339, 2000. 113

[29] J. Wohlert, W. K. den Otter, O. Edholm, and W. J. Briels. Free energy of a trans-membrane pore calculated from atomistic molecular dynamics simulations. *The Journal of Chemical Physics*, 124(15):154905, 2006. 113

[30] Hari Leontiadou, Alan E. Mark, and Siewert J. Marrink. Molecular dynamics simulations of hydrophilic pores in lipid bilayers. *Biophysical Journal*, 86(4):2156–2164, 2004. 113

[31] T. V. Tolpekina, W. K. den Otter, and W. J. Briels. Nucleation free energy of pore formation in an amphiphilic bilayer studied by molecular dynamics simulations. *The Journal of Chemical Physics*, 121(23):12060–12066, 2004. 114

[32] Smith AM, Vinchurkar M, Gronbech-Jensen N, and Parikh An and. Order at the edge of the bilayer: Membrane remodeling at the edge of a planar supported

bilayer is accompanied by a localized phase change. *Biophys. J.*, 99:3264–3273, 2010. 114

[33] Peter M. Kasson and Vijay S. Pande. Molecular dynamics simulation of lipid reorientation at bilayer edges. *Biophysical Journal*, 86(6):3744–3749, 2004. 114

[34] Yong Jiang and James T. Kindt. Simulations of edge behavior in a mixed-lipid bilayer: Fluctuation analysis. *The Journal of Chemical Physics*, 126(4):045105, 2007. 114

[35] J. de Joannis, F.Y. Jiang, and J. T. Kindt. Simulations of edge behavior in a mixed-lipid bilayer; fluctuation analysis. *J. Chem. Phys.*, 126:045105, 2006.

[36] Hao Wang, Jason de Joannis, Yong Jiang, Jeffrey C. Gaulding, Birgit Albrecht, Fuchang Yin, Kunal Khanna, and James T. Kindt. Bilayer edge and curvature effects on partitioning of lipids by tail length: Atomistic simulations. *Biophysical Journal*, 95(6):2647–2657, 2008. 114

6

Simulation Studies of Structure and Edge Tension of Lipid Bilayer Edges: Effects of Tail Structure and Force-Field

6.1 Introduction

Because the lipid bilayer is the foundation of biological membranes, its mechanical properties influence the stability and flexibility of living cells. A key property of the lipid bilayer is the reversible work per unit length required to form an edge defect, which is equivalent to the line tension (Λ) of the edge, hereafter edge tension. This tension drives small isolated bilayer patches to curve into closed vesicles (1) and causes pores in extended bilayer sheets to close spontaneously. (2, 3) Conditions of very low edge tension lead to the thermally-induced proliferation of pores and membrane fragments, while very high edge tension may impede bilayer fusion and fission.

Quantifying edge tension experimentally is challenging. A range of strategies have been developed. (2–11) The most recent efforts in this area (10, 11) have used variations on a strategy first employed (8) by Brochard-Wyart and co-workers, based on a measuring the dynamics of closure of a transient pore induced in a giant unilamellar vesicle. Computer simulation is a valuable complement to experimental studies of lipid bilayer edge tension for several reasons. The ability to investigate the structure of the edge is one. Another is the ability to control composition and maintain an impurity-free system; the observation by Karatekin et al. (8) of a large difference in edge tension between vesicles formed with DOPC obtained from two different sources indicates that trace quantities can affect the edge line tension. Two main computational strategies have been used for the analysis of edge tension in bilayer simulations. Edge tension in a single pore in a finite patch, maintained at fixed area, can be inferred from the surface tension that resists pore closing and the radius of the pore. (12, 13) One drawback of this method is that due to the hourglass shape of the pore it relies on an arbitrary definition of the pore radius. Furthermore, a bilayer under surface tension will have properties different from a stress-free bilayer, which may influence the edge properties. The other strategy is the use of a ribbon geometry, (14–16) with the edge of the ribbon directed along one axis of the simulation box. The reduction in mean pressure along the edge axis, multiplied by the simulation box area perpendicular to the edge, yields a force that can be attributed to the sum of the tensions of the two edges:

$$2\Lambda = L_X L_Z \left(\left(\frac{P_{XX} P_{ZZ}}{2} \right) - P_{YY} \right) \tag{6.1}$$

where the edge is located along the Y axis of the simulation box with dimensions $L_X \times L_Y \times L_Z$, with P_{XX}, P_{YY}, and P_{ZZ} representing the diagonal elements of the pressure tensor. In previous studies aimed at determining edge line tensions from atomistic simulation models, it has been confirmed that Λ matches experimental values in order of magnitude ($\sim 10-11$ N), but large uncertainties in pressure tension elements prevented calculation of Λ at sufficient precision to study variations in Λ among lipids. Wohlert et al.(15) found that pore-based and ribbon-based methods yielded 40 pN and 50 pN respectively for the edge tension of DPPC, but based on our error analysis in the current and previous (16) studies we estimate an uncertainty of ±10 pN for the ribbon calculation from the short trajectory duration of 5 ns. In the present study, edge tensions have been calculated from simulations of bilayer ribbons composed of seven different lipids that share a common phosphatidylcholine headgroup structure but differ in the length and degree of saturation of their tails (figure 6.1). Simulations on one lipid type were performed with three forcefields to assess whether different parameters sets yield important differences in this property.

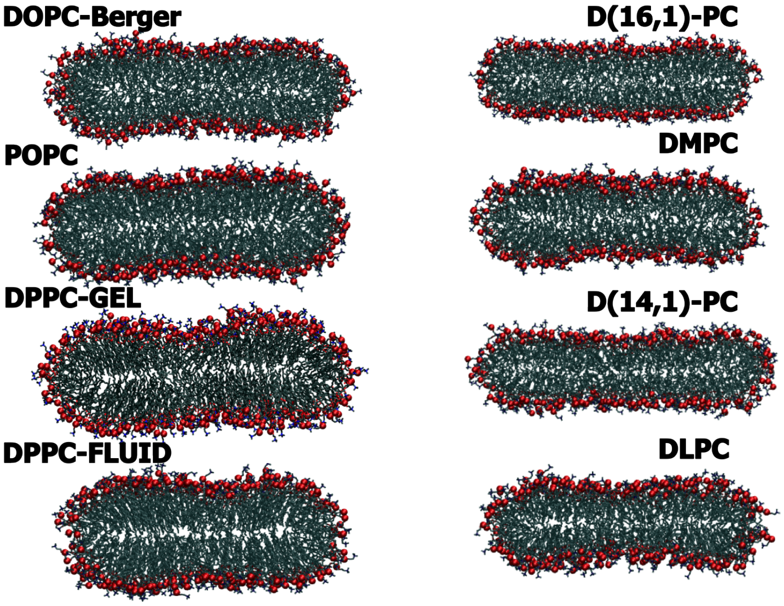

Figure 6.1: Snapshots of ribbons cross-sections in the XZ plane - at the 100ns of the trajectories. The red spheres show the phosphorus (P) headgroup atom positions.

Simulation trajectories >200 ns were used to reduce statistical uncertainty in the mean pressure tensor elements and lower estimated statistical uncertainties below ± 3 pN. Correlations between edge line tension and other properties of the bilayer have been studied to determine how best to represent the origin of edge line tension in terms of the elastic properties of the membrane.

6.2 Methods

6.2.1 Intact Bilayer Simulations

To obtain reference data on lipid properties in an edge-free environment, 128-lipid bilayer patches, continuous in two dimensions under periodic boundary conditions, were modeled via MD using Gromacs 4.5.4 (17) with a time step of 2 fs. The lipids studied shared a common phosphatidylcholine (PC) headgroup and glycerol backbone. A series of di-saturated-tail lipids with 12-, 14-, or 16-carbon fatty acyl tails (dilauroyl, dimyristoyl, and dipalmitoyl phosphatidylcholine, henceforth DLPC, DMPC and DPPC); a series of di-cis-Δ-9 monounsaturated-tail lipids with 14-, 16- or 18-carbon fatty acyl tails (dimyristoleoyl, dipalmitoleoyl, and dioleoyl PC, henceforth D(14,1)PC, D(16,1)PC, and DOPC); and the mixed-tail lipid POPC were studied. All lipids were simulated using the Berger united atom forcefield (18) (incorporating tail torsional parameters for unsaturated-tail sites as used previously in our group (19)). Additional trajectories for DOPC bilayers were performed with the 43A1-S3 united atom forcefield of Chiu et al. (20) and with the atomistic CHARMM C36 lipid parameter set. (21, 22) The water models used in conjunction with the Berger force-field, the 43A1-S3 parameter set, and the C36 forcefield were SPC (23), SPC/E, (24) and TIP3P (25) respectively. The number of waters per lipid and the box dimensions for intact bilayers are detailed in table 6.1.

The temperature was maintained at 300 K using the Berendsen thermostat with a 0.4 ps time constant. (26) Pressure was maintained at 1 bar in both the P_{xx}/P_{yy} lateral dimensions and in the P_{zz} normal direction using the Berendsen semiisotropic pressure coupling scheme with a constant of 1.0 ps and 4.5×10^{-5} bar^{-1} compressibility. Lipid covalent bonds and water geometry were constrained via

Table 6.1: Simulations performed and structural description

	Num. Lipids	Water/Lipid Ratio	Force-Field	Cumulative Time(ns)	Box(nm)
			Ribbons		
DOPC	256	84.3	CHARMM-C36	230	19.5, 7.0, 8.0
	256	64.6	43A1-S3	200	20.0,7.0, 8.0
	256	64.6	Berger	300	20.0, 6.7, 6.2
D(16,1)-PC	256	42.8	Berger	230	15.4, 6.5, 6.5
D(14,1)-PC	256	42.8	Berger	250	15.4, 6.5. 6.5
POPC	256	69.7	Berger	272	19.5, 7.0, 7.0
DPPC-Fluid	256	42.8	Berger	210	19.3, 6.5, 6.5
DPPC-Gel	256	42.8	Berger	210	17.0, 5.7, 9.0
DMPC	256	42.8	Berger	215	19.3, 6.5, 6.5
DLPC	256	42.8	Berger	210	15.2, 6.5, 6.3
	256	75.6	Berger	250	18.0, 7.0, 7.0
			Intact Bilayers		
DOPC	128	53.3	CHARMM C36	41	8.3, 8.3, 5.1
	128	28.6	43A1-S3	80	6.5, 6.6, 6.6
	128	28.6	Berger	78	6.5, 6.6, 6.6
D(16,1)-PC	128	28.6	Berger	80	6.6, 6.6, 6.0
D(14,1)-PC	128	28.6	Berger	80	6.5, 6.5, 6.0
POPC	128	28.6	Berger	80	6.2, 6.2, 6.8
DPPC-323K	128	28.6	Berger	100	6.5, 6.5, 6.6
DPPC-300K	128	28.6	Berger	77	6.5, 6.5, 6.5
DMPC	128	28.6	Berger	80	6.2, 6.3, 6.3
DLPC	128	28.6	Berger	80	6.2, 6.2, 6.1
			Bilayers with pores		
DOPC	256	65.5	Berger	212	11.0, 11.0, 7.0
DOPC	256	112.5	Berger	215	11.5, 11.5, 9.2
DMPC	256	42.8	Berger	211	10.4, 10.4, 5.8
POPC	256	69.5	Berger	220	10.7, 10.7, 7.6

LINCS (27) and SETTLE (28) algorithms respectively. Coulombic interactions were evaluated using the PME technique with 0.12 nm grid spacing and cubic interpolation. (29) A cut-off of 1.0 nm was used for Van der Waals interactions.

6.2.2 Ribbon simulations

To initiate structures for ribbon trajectories for all lipids except D(16,-1)PC and D(14,1)PC, a fully equilibrated and solvated continuous 128-lipid bilayers was replicated 2-fold in the X direction and centered in a simulation box $3 \times 1 \times 1$ times the dimensions of the original box, leaving two discontinuous edges parallel to the Y dimension. The newly created space was solvated using the genbox utility of Gromacs 4.5.4, with waters in the lipid tail region removed, yielding total numbers of water molecules indicated in table 6.1. A brief minimization using the steepest descents method was applied where necessary to remove unfavorable water contacts. The D(16,-1)PC and D(14,1)PC ribbons were produced by removing two and four carbons respectively from the tails of a lipid at the endpoint of the DOPC ribbon simulation; the empty space created was rapidly filled by constriction of the simulation box under the applied pressure. Details of the simulation and force-field parameters were identical to the reference bilayer simulations, except that in the ribbon production runs the pressure was maintained at 1 bar using Berendsen anisotropic pressure coupling with 5.0 ps time constant and $4.5e^{-5}$ bar^{-1} xx/zz compressibilities, and with the box dimension along the Y-axis (parallel to the ribbon edge) fixed.

In the case of DPPC, the simulation temperature (300 K) is below the gel-fluid transition temperature (314 K according to experiment, (30) and near 308 K for the Berger forcefield.(31)) Because the phase transition rate is generally slow on the simulation timescale, ribbon structures were prepared both from bilayers started in the tiled gel (L'_β) and the fluid (L_α) phase; these will be referred to as "DPPC-gel" and "DPPC-fluid" systems, even though neither equilibrated ribbon structure can be identified definitively with one phase or the other. Ordered, tilted gel-phase bilayers were prepared following the procedure in reference 30 ; the initial tail tilt azimuthal angle was directed approximately 30 away from the Y-axis. Finally, two independent trajectories, with different box dimensions, were carried out for DLPC to investigate the role of finite-size artifacts on structure and line edge tension in the ribbons.

The first 10 ns of all trajectories were excluded for the purposes of analysis. The edge tensions were obtained using eq 6.1, with reported uncertainties calculated using the blocking method.(32) The 10 ns duration necessary for initial system equilibration is decided as initial simulation period not affecting the converged values of edge tension. For structural analysis, the set of lipid coordinates for each frame to be analyzed was first translated to bring the center-of-mass of the lipid ribbon to the origin of a Cartesian coordinate system and rotated (using the Gromacs editconf utility) so that its principle axes of inertia lay along the coordinate axes. Phosphorus site P-density profiles were constructed from sampling phosphorus atom X and Z coordinates from MD trajectories at 250 ps resolution. Binning and averaging the phosphorous Z-coordinates of all P-sites in 0.05 nm increments along the x direction identified the contour line of each leaflet of the ribbon, resulting in two functions $z_{upper}(x)$ and $z_{lower}(x)$, whose difference defines a local ribbon thickness. The contour lines showed a minimum thickness near the midpoint along x. The x-position near each edge where local thickness reached a maximum, x_t, was considered the onset of the lipid bilayer edge region; the edge contour was hemi-elliptical to a reasonable approximation. The semi-major elliptical axis was calculated as $x_{max} - x_t$ where x_{max} is the highest occupied bin along x, while the minor elliptical axis was the local thickness at x_t (figure 6.2). The edge area per lipid (A_{EDGE}) was determined from multiplying the perimeter of the ellipse by the L_Y dimension of the box and dividing the result by the average number of P-sites in the edge region. The area per lipid in the bilayer-like middle region (A_{MIDDLE}) and the ribbon interior thickness h were retrieved from sculpting a 2.0 nm × 2.0 nm xy block near the center of the ribbon and counting the local area density and average local thickness.

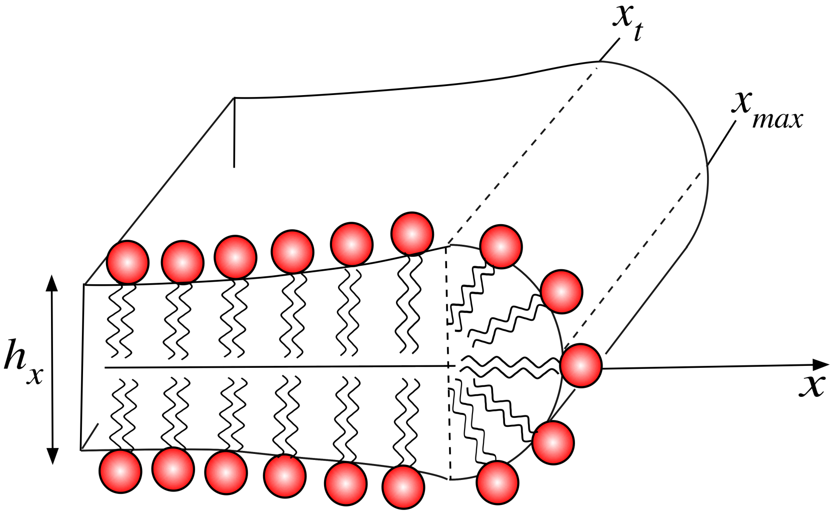

Figure 6.2: Structural parameters associated with bilayer edge geometry -

A qualitative measure of the degree and direction of local tail tilt alignment was visualized by first calculating the displacement vector $d_{C,C+2}$ and midpoint in the XZ plane between each tail CH_2 site and the site 2 carbons farther down the tail. The vectors were binned in two dimensions according to the position of the midpoint in X and Z (with a resolution of 0.2 nm). The vector sum of all vectors with midpoints in that bin (summing over the length of the ribbon) was taken for each frame and divided by the bin volume (0.2 nm $\times$0.2 nm $\times L_Y$); an average of that vector density was taken over all production trajectory frames. The segments plotted represent the mean of the product of the displacement vectors (in nm) with the density (in sites/nm^3), scaled to 4% of their value to improve visibility, and are oriented in the direction of the vector sum of all $d_{C,C+2}$ vectors in that X, Z region.

6.2.3 Bilayers with Pores in Constant Area Simulations

The pore simulations at constant area consist of 256 lipids and levels of hydration specified in table 6.1. To create the unit cell, a 344 lipid bilayer patch was equilibrated for 10ns using the simulation parameters outlined in the 'Intact Bilayer Simulations', section 6.2.1. The pore was instituted by removing the remainder number of lipids from the center of the equilibrated bilayer. The constant xy area of the subsequent production runs was maintained by setting the xx/yy compressibilities to zero.

The pore in the DOPC bilayer hydration level 112.5 was instilled by removing 256 lipids from the center of a 512 lipids patch, hydrating the systems further to avoid interactions between periodic images along the L_Z direction, and closing the pore further in 85 ps of standard molecular dynamics simulation.

The radius of pores in simulation was determined in the following manner. The x, y, z vector components of the phosphorus atoms were sampled across >200 ns trajectories at 150 ps resolution and subsequently centered at $[0, 0, 0]$. From this data set the x and y components within 1 nm of the center of mass along the orthogonal bilayer normal direction were selected and binned at 1 ns subtrajectory resolution. This choice corresponds to only counting the lipids from the most circular section of the hourglass shaped pore. The radius of the circle (R_{PORE}) was determined using the *circfit* function of Matlab. The surface tension in simulations has the formula:

$$\gamma = L_z \times (P_{zz} - (P_{xx} + P_{yy})/2) \qquad (6.2)$$

The edge tension and surface tension are related via:

$$\Lambda = R_{PORE} \times \gamma \qquad (6.3)$$

6.3 Results AND Discussion

6.3.1 General observations on ribbon structures

Edge tensions, ribbon interior and edge dimensions and areas per lipid observed for all systems are shown in Table 6.2.

Table 6.2: Simulation edge tensions, edge dimensions, and lipid packing characterization.

				Ribbons			
	Edge tension (pN)	h (nm)	major axis (nm)	thickness at edge (nm)	N_{LIPIDS}/L_{EDGE} (nm^{-1})	A_{MIDDLE} (nm^2)	A_{EDGE} (nm^2)
DOPC	46.1 ± 1.65	3.69	2.68	4.18	6.9	0.686	1.10
DOPC-C36	44.3 ± 2.1	3.87	3.17	4.25	8.1	0.668	1.04
DOPC-43A1-S3	44.6 ± 3.1	3.85	3.25	4.25	8.9	0.652	0.964
D(16,1)-PC	44.0 ± 2.2	3.41	2.91	3.75	7.6	0.683	1.00
D(14,1)-PC	30.4 ± 1.8	3.14	2.23	3.54	6.1	0.686	1.04
POPC	32.4 ± 2.0	3.79	3.10	4.32	8.8	0.642	0.942
DPPC-Fluid	27.5 ± 2.9	4.12	3.24	4.48	10.4	0.594	0.836
DPPC-Gel	16.3 ± 3.7	4.16	3.01	4.50	10.6	0.572	0.797
DMPC	19.2 ± 2.8	3.39	3.01	3.96	9.1	0.619	0.866
DLPC-42.8	10.0 ± 2.7	2.95	2.24	3.48	6.6	0.634	0.945
DLPC-75.6	14.2 ± 2.1	3.01	2.81	3.42	8.5	0.628	0.845
				Intact Bilayers			
			t (nm)		$A_{BILAYER}$ (nm^2)		
DOPC			3.69		0.698		
DOPC-C36			3.80		0.678		
DOPC-43A1-S3			3.79		0.680		
D(16,1)-PC			3.39		0.693		
D(14,1)-PC			3.13		0.680		
POPC			3.73		0.652		
DPPC			3.76		0.620		
DMPC			3.37		0.631		
DLPC			2.99		0.638		
			Bilayers with Pores				
		R_{PORE} (nm)		Surface Tension (mN/m)	Edge tension (pN)		
DMPC		2.7		8.5		23.3 ± 0.6	
POPC		2.7		13.1		35.5 ± 0.5	
DOPC-65.5		2.7		13.5		36.4 ± 0.5	
DOPC-112.5		3.3		12.8		41.9 ± 0.5	

All systems showed a distinctly reduced density of headgroup sites at the edges (Figure 6.3) indicating an expansion in area per headgroup, and some tendency toward local thickening near the edges.

The P-P thicknesses h and areas of the middle section of the ribbons were

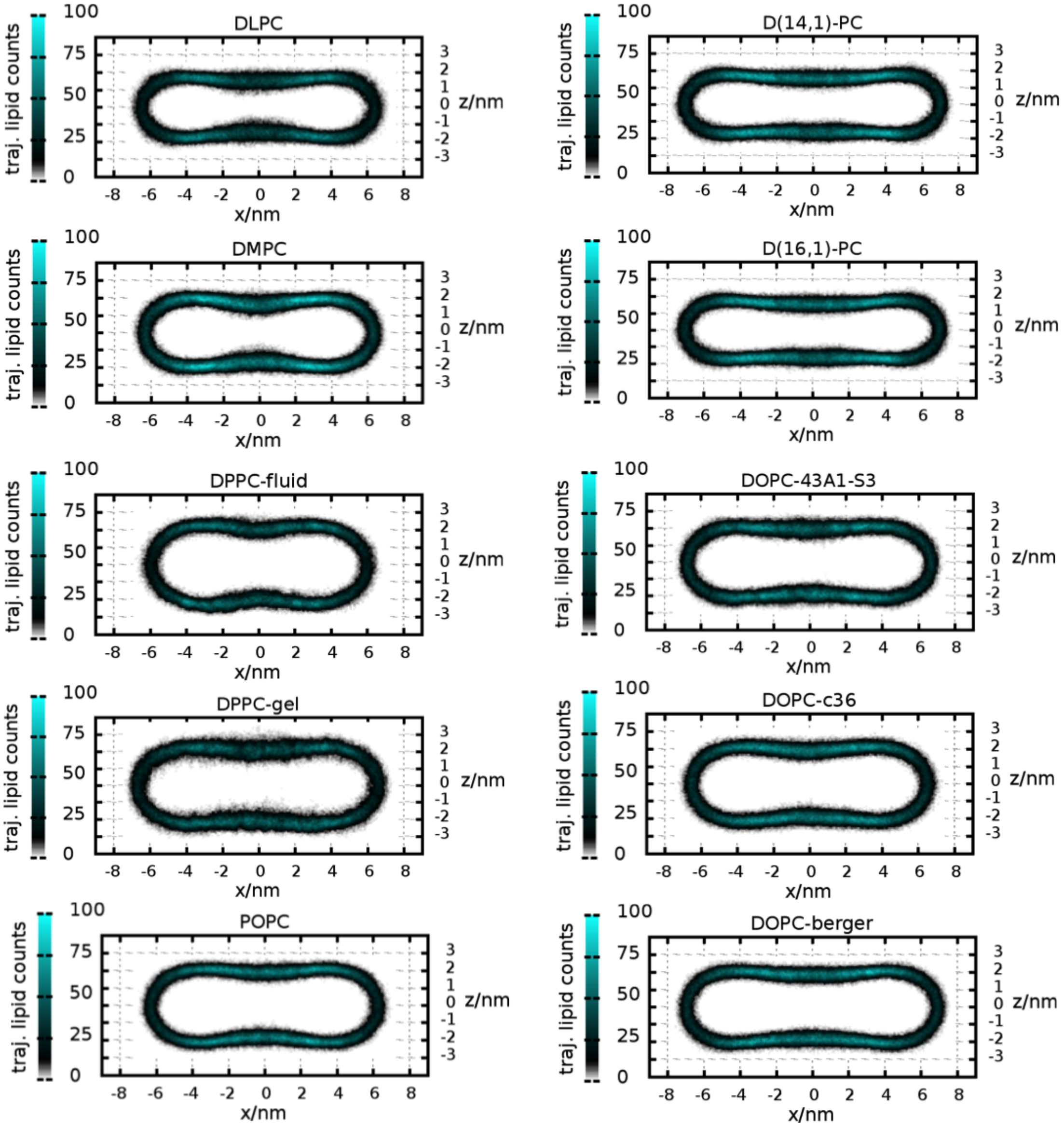

DLPC

D(14,1)-PC

DMPC

D(16,1)-PC

DPPC-fluid

DOPC-43A1-S3

DPPC-gel

DOPC-c36

POPC

DOPC-berger

Figure 6.3: 3D-Phosphorous (P) density plots - to show differences in ribbon shape and outline variations in lipid density. The plots were constructed from XZ vector positions sampled across the >200ns trajectories at a resolution of 250 ps.

consistent with the continuous bilayer thicknesses to within 2% (excepting the case of DPPC, for which the gel/fluid transition prevents a direct comparison.) Lipid areas calculated for the ribbon interior were similarly consistent with the mean area per headgroup of the intact bilayers. These results would suggest that the ribbons are wide enough (at least well above T_m) that the lipids at the ribbon midsection are not strongly perturbed by the proximity to the edge, which is a necessary condition to avoid artifacts from the finite ribbon width. On the other hand, the shapes of the DLPC ribbons simulated under different box dimensions showed some variation - in particular, in the system with a greater box size, the local maximum in thickness is farther away from the far extent of the edge, and the entire edge region (whose onset is defined here by a local maximum in thickness) is larger. Nonetheless, the edge tensions calculated in these two systems are in agreement within the estimated statistical uncertainty.

6.3.2 Edge tension of DOPC: dependence on force-field

Comparisons of the results obtained from different lipid forcefields are useful for guiding user forcefield selection and future forcefield development.(33) The edge tension predicted by a given forcefield for a bare bilayer edge is very likely relevant to its prediction of the relative stabilities of various proposed structures of proteinaceous pores.(34) DOPC, the most commonly studied lipid in experimental determinations of edge tension, was chosen for a comparative study across three force-fields. The Berger united atom forcefield (18) (incorporating tail torsional parameters as used previously in our group(19)) and the 43A1-S3 united atom forcefield of Chiu et al.(20) were compared with the atomistic CHARMM C36 lipid parameter set. (21, 22) The three characterizations yielded remarkably similar edge tensions of 46, 45, and 44 pN respectively. As all these parameter sets have been validated against the same experimental structural and elastic properties (areas, thicknesses, area compressibilities, and bending moduli), it is possible that some combination of these properties uniquely determines (or strongly constrains) the edge tension.

6.3.3 Edge tension of DOPC: comparison with experiment

Although consistent with each other, values near 45 pN obtained from simulation are significantly greater than experimentally determined values for the edge tension of DOPC bilayers, which have ranged from 7 pN to 28 pN.(6, 8, 11) Several explanations can be considered for this discrepancy. A systematic error in the simulation methods - e.g. some error in the interaction potential feature common to all three forcefields, or an effect artifact of the finite size of the ribbon system, or a slow ($>$ 200 ns timescale) transition to a more stable edge structure that is not captured in the current trajectories - could produce an excessively high edge tension in simulation.

As an additional check on the robustness of the simulated edge tensions, edge tensions of three lipid types were also obtained through the effect of a pore on bilayer surface tension, following Eq. 6.3. Edge tensions of DMPC and POPC obtained for pores of radius 2.7 nm were 3 to 4 pN greater than for ribbons, while for DOPC, pores of size 2.7 nm and 3.3 nm yielded line tensions 10 pN and 5 pN lower than the ribbon state. The pore size dependence could reflect the uncertainty in the proper definition of pore radius or an effect of the in-plane curvature on the edge stability; both of these factors would produce edge tensions that should approach the value obtained from a flat ribbon as the pore size is increased. It should be noted that the giant unilamellar vesicle pores from which the experimental edge tensions were obtained in ref. 11 have radii of order 1 μm, and therefore have negligible in-plane curvature. On the experimental side, the effect of impurities on edge tension may be a factor. The potential for contaminants to influence experimental measurements of edge tension has been documented. Comparison of DOPC obtained from two vendors using the same protocol yielded edge tensions differing by 14 pN. (8) As in the case of the surface tension of bulk water, which can be completely eliminated by a small mole fraction of surfactant but can only be raised modestly by high concentrations of inorganic salts,(35) low levels of impurities are much more likely to reduce edge tension rather than raise it. “Edge-active” impurities(1) can be very effective at reducing edge tension because they will strongly partition to the edge and change its properties dramatically, even if they represent a small fraction of lipids present in the bilayer away from the edge. In one case where a systematic study was made of the effect of an edge-active molecule, (36) the threshold level at which the short-tail lipid DHPC stabilizes the DMPC edge (eliminating the edge tension completely) was estimated to be as low as 1-2% at 25° C. In contrast, molecules that would tend to raise the free energy of the edge will simply stay mixed in the main bilayer, and at low levels are expected to contribute to the edge tension only slightly, through the entropy loss associated with excluding them from the edge. (One important case where an increase in edge tension has been observed upon addition of a new membrane component is cholesterol;(8, 11) such effects have only been reported, however, at cholesterol levels of 10% or greater, where cholesterol is known to cause changes in lipid ordering through the bulk of the bilayer.)

6.3.4 Lipid tail dependence of edge tension

Using Berger force-field parameters, the effects of tail length and degree of saturation on edge tension were compared after ribbon simulations of a series of saturated-tail lipids with tail lengths 12, 14, and 16; cis- mono-unsaturated lipids with tail lengths 14, 16, and 18; and a single mixed saturated C_{16}/mono-unsaturated C_{18}-tail lipid (POPC). As evident in figure 6.4, edge tension was positively correlated with tail length, while lipids with two cis mono-unsaturated fatty acyl chains displayed greater edge tensions than fully saturated lipids at the same tail length. A correlation with tail length would seem to imply a correlation with bilayer thickness; however, comparing DMPC and D(16,1)-PC, which have nearly the same thickness but very different edge tensions, shows that other bilayer properties must be taken into account.

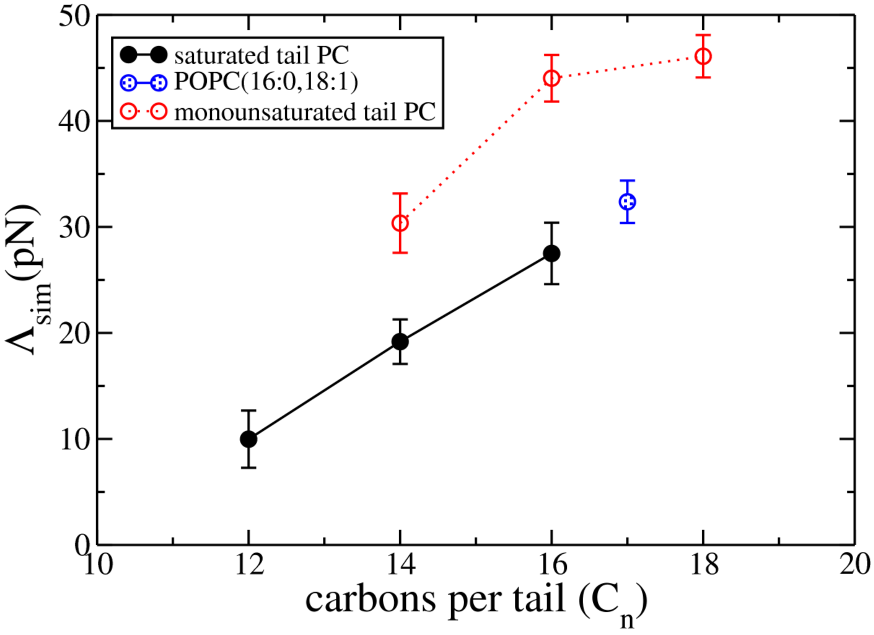

Figure 6.4: Edge tensions (Λ_{sim}) from ribbon simulation vs. number of carbons (C_n) in lipid tails - from simulation of saturated lipids: DLPC-42.8, DMPC, DPPC-Fluid (filled circles), from simulation of unsaturated lipids (open circles), and from simulation of mixed-tail lipid POPC (grey circle).

6.3.5 Effects of the edge environment on lipid conformation and packing

The structural origin of edge tension arises from the deformation of the lipids that occupy the edge. We have investigated structural changes to the tails and to the headgroups. As an indicator of tail disorder, tail dihedral statistics (specifically, fraction of tail C-C bonds dihedrals angles that are in the range associated with the gauche conformer) were compared for lipids at the ribbon edges and lipids in the flat bilayer interior. For DLPC and DMPC, the fractions are nearly identical. For DPPC, edge lipid dihedrals had a slightly greater probability (10.7%) to be found in the higher-energy gauche conformer than ribbon interior lipid dihedrals (9.5%), independent of the initial phase (gel or fluid phase) used in ribbon construction (table 6.3).

Table 6.3: Percentage (%) tail dihedrals

	Ribbon	
	Middle	Edge
DLPC-42.8	11.1	11.4
DLPC-75.6	11.1	11.4
DMPC	10.9	11.2
DPPC-Fluid	9.5	10.7
DPPC-Gel	9.0	10.5
	Bilayer	
DLPC	11.1	
DMPC	11.0	
DPPC	10.6	

As an indicator of headgroup environment, we have assessed the area per lipid at the edge and compared it with the ribbon interior. From the simulated ribbons we have found the area per lipid at the edge by fitting the surface of the curved edge to an ellipse and using the perimeter of the ellipse. The standard definition for the surface of a phospholipid bilayer is the surface of maximum electron density, which tends to coincide with the peak in the phosphorus atom distribution, which was used for the analysis of edge shape and area per lipid as described in Methods. Area per headgroup was always greater at the edge, consistent with a simple geometric treatment of the edge shape as a hemicylinder.(37) The degree of the expansion (see table 6.2) was lower than the factor of 2 predicted from the simplest model of an incompressible bilayer with an edge cross-section shaped like a semicircle with diameter equal to the bilayer thickness. There are several reasons the simple ratio is not applicable: the edge shape is not exactly a semicircle, the bilayer can display local thickening near the edge, and the bilayer is not strictly incompressible (especially in the hydrophilic region where volume per lipid depends on the degree of hydration.) Area expansion at the edge was greater for unsaturated-tail lipids.

6.3.6 Correlation between structure and edge tension

To better understand the factors determining edge tension, we seek an appropriate quantitative description of this deformation and the associated elastic energy cost. Previous phenomenological treatments of line tension have focused on the curvature of the edge; (38) for instance, an empirical correlation between Λ and the bilayer curvature modulus κ_c has been identified. (9) Wohlert et al. have previously compared the line tension obtained both through pore and ribbon methods with predictions of a simple curvature elasticity formula based on the bending modulus of the bilayer.(15) In generating this formula, the edge is assumed to be a hemicylinder whose curvature is a constant $1/r$ (with r the thickness of a monolayer) and whose area per unit length of the edge is πr. The corresponding elastic energy (neglecting spontaneous curvature) per unit length, within a Helfrich-type framework for curvature elasticity, is:

$$\Lambda = \frac{\kappa_{monolayer}}{2}\left(\frac{1}{r}\right)^2(\pi r) = \frac{\kappa_{monolayer}\pi}{2r} = \frac{\kappa_{bilayer}\pi}{2t} \tag{6.4}$$

In ref. 15, the predicted value of Λ =20 pN for DPPC at 323 K obtained based on eq. 6.4 (using $k_{bilayer}$ determined in previous simulations of the same model (39)) was significantly smaller than the values of Λ = 40 or 50 pN obtained using pore and ribbon methods respectively. Equation 6.4 relies on several questionable assumptions: that monolayer spontaneous curvature is negligible, that the elastic energy is harmonic in curvature even at the extreme curvatures of the edge, that $\kappa_{monolayer}$ is simply half of the bilayer curvature modulus κ_c, and that the radius at which the curvature should be evaluated can be assigned is well-defined. Inserting bending modulus and thickness data from the recent experimental literature (all obtained through X-ray diffraction at a temperature of 303 K) for DOPC,(40) ($\kappa_{bilayer} = 7.6 \times 10^{-20}$ J, t =3.67 nm) DMPC, (41) ($\kappa_{bilayer} = 6.9 \times 10^{-20}$ J , t =3.53 nm) and DLPC (41) ($\kappa_{bilayer} = 5.5 \times 10^{-20}$ J, t = 3.08 nm) into eq. 6.4 yields nearly identical edge tensions (33 pN, 31 pN, and 28 pN respectively), in contrast to the wide range (44-46 pN, 20 pN, 10-14 pN) obtained from simulation. A systematic correlation of the simulated edge tensions with predictions of eq. 6.4 and related formulas would be of interest, ideally assessed using consistent conditions of forcefield and temperature. At present we have not performed the extensive simulations necessary to assess bending elasticity (39) and spontaneous curvature (42) for each of the lipids considered. Instead, following the framework of Israelachvili et al.,(43) we note that (assuming incompressible tails) the lipid headgroups at the edge must be spaced more widely than in the bilayer, where the area per headgroup is determined as an optimal balance between headgroup and tail packing influences. This increased spacing is evident in the reduced phosphorus site density around the rims in Figure 6.3. The expansion of headgroups increases the surface energy associated with contact between the solvent and lipid tails. We hypothesized that the edge tension is proportional to the product of the increase in area (per unit length of the edge) and a surface tension associated with the solvent-hydrophobic interface, and that the headgroup-expansion effect dominates any other effects of molecular packing in contributing to the edge tension:

$$\Lambda_{pred} = \frac{A_{EXCESS}}{L_{EDGE}}\gamma = \frac{N_{LIPIDS}}{L_{EDGE}}\left(A_{EDGE}\left(\Delta r\right) - A_{MIDDLE}\right)\gamma \tag{6.5}$$

Equation 6.5 has two adjustable parameters: the surface tension mentioned above, and a surface offset Δr that defines the contour of the curved surface. It can be seen as a radical simplification of more complete free energy expressions used in previous theory (44) for the thermodynamics of the edge. From the simulated ribbons we have found the area per lipid at the edge, by fitting the surface of the curved edge to an ellipse and using the perimeter of the ellipse. However, the area of a curved surface will depend on the definition of the surface's position. Whereas the most common definition for the surface of a phospholipid bilayer is based on phosphorus atom sites, as was used for the analysis of edge shape and area per lipid as described in Methods, lateral pressure profiles calculated from previously published simulations (45–48) reveal that the plane of minimal lateral pressure (greatest surface tension) coincide roughly with the region populated by glycerol and acyl ester sites, 0.19-0.25 nm below (towards the midplane of) the phosphorus site peak. Here we treat the offset Δr between the standard phosphorus site surface and the surface at which the tension should be evaluated as an adjustable parameter. To correct the area for the offset Δr, we have recalculated the area of the hemi-elliptical edge $A_{EDGE}(\Delta r)$ by reducing the semi-major and semi-minor axis lengths of the ellipse from Table 6.2 by Δr, and determined the parameters of γ and Δr that minimize the least-square deviation between Λ_{pred} from Eq. 6.5 and the edge tension obtained from simulation using Eq. 6.1. (Only systems simulated using the Berger force-field parameters were included in this fit.) The results from the area expansion model (Eq. 6.5) are compared to simulation results in Figure 6.5.

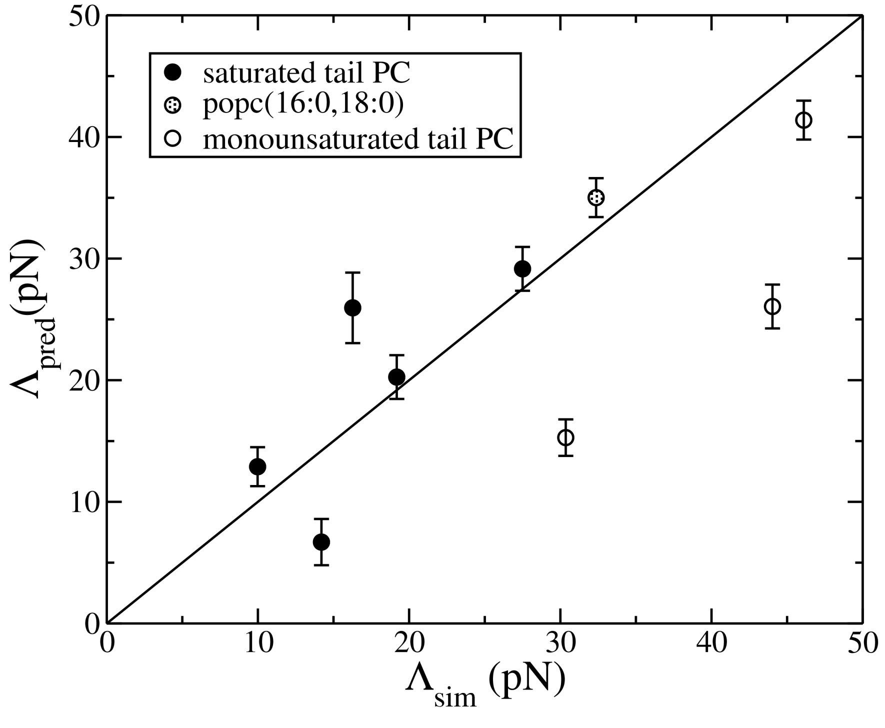

Figure 6.5: Edge tension from area expansion model - (Λ_{pred} (pN) equation 6.2) vs. edge tension from simulations (Λ_{sim}(pN)). Filled, grey, and open circles are edge tensions of saturated-tail lipids, mixed-tail lipid POPC, and unsaturated-tail lipids respectively. A line with slope 1 is used to guide the eye.

The saturated-tail lipids, plus POPC and DOPC, give good agreement with model predictions; the correlation between predicted and simulated values is worst for D(14,1)-PC and D(16,1)-PC. The best-fit choices of γ and Δr were 36.0 mN/m and -0.54 nm respectively. The surface tension is within a factor of two of experimental values for water/alkane surface tension (50-55 mN/m).(49) (The model neglects headgroup-headgroup repulsions, which will contribute a negative term to the free energy as the spacing increases, and would reduce the apparent surface tension.) The offset distance Δr is rather greater than expected for the location of the plane of greatest surface tension. Nonetheless, the results suggest that a measure of area expansion is sufficient to rationalize the observed trends in edge tension to a first approximation.

Although tail effects are not explicitly included in Eq. 6.5, they are obviously important in determining how the lipids can be packed at the edge such that area expansion can be minimized. Tail packing effects can explain the effect of tail saturation on the edge tension. Bilayer thickening near the edge produces a rim with a larger radius of curvature and a lower area/volume ratio. The saturated-tail lipids showed lower degrees of area expansion at the edge and also showed a greater tendency for local thickening near the edge. The greater accommodation through local thickening can be attributed to the greater extensibility of the saturated-tail chains. In contrast to the saturated-tail chains, which have an energetic minimum in a fully extended state, the energetic minimum for tails with a single cis double bond has a kinked conformation due to the torsional potentials of C-C single bonds neighboring the double bond.(50) The under-prediction of the edge tension by Eq. 6.5 for the 14- and 16-carbon unsaturated-tail lipids may indicate that unfavorable tail packing at the curved edge per se, as opposed to the ability of a packing arrangement to reduce headgroup expansion, contributes to the instability of the edge in these cases.

The most striking example of how tail packing is coupled to the curvature at the edge is found in a DPPC bilayer ribbon initiated in a tilted gel-phase (L'_β) state, with tail groups highly ordered and extended. Over the course of 25 ns simulation at 300 K (below the phase transition temperature of 308 K estimated for this DPPC model (31)) the lipids reoriented from having a uniform tilt alignment in both leaflets (originally pointing partially along the edge direction and partially toward the left edge) to having a “herringbone” mirror-image tilt at both sides, with a disordered region in between. A ribbon initiated with lipids in a disordered, fluid (L_α) arrangement and equilibrated at the same temperature developed the same pattern. Although this structure can be discerned from individual snapshots (figure 6.3), it is even more apparent from a plot of the tail orientation field vector within the cross-sectional plane of the ribbon (figure 6.6). In contrast to the other lipids modeled, where the tails were untilted (aligned along Z on average) except at the highly curved rims, DPPC tails tended to tilt with their ends towards the center of the ribbon except in a narrow zone near the center of the ribbon ($x = 0$).

A reduction of diffusion rates near bilayer edge defects (51) at temperatures near T_m has been reported in the literature, which may be associated with the ability of the edge to induce such a gel-like herringbone arrangement within the bilayer even when the temperature is above the bulk T_m. The observation of a uniform mirror-image tilt arrangement across the leaflets in previous low-temperature simulations of intact bilayers of DSPC (52) suggests that such an ordered structure may be energetically close to the common tilted-gel structure with tails in the two leaflets co-aligned. In the ribbon simulations, the geometry imposes a transition in the direction of tail vectors in each leaflet between the left and right ribbon edges; the change in direction in the flat part of the ribbon is accompanied by considerable disorder. In an extended system as studied experimentally in reference 51, the edges are far from each other and the herringbone pattern could potentially persist into the bilayer interior on a micrometer scale.

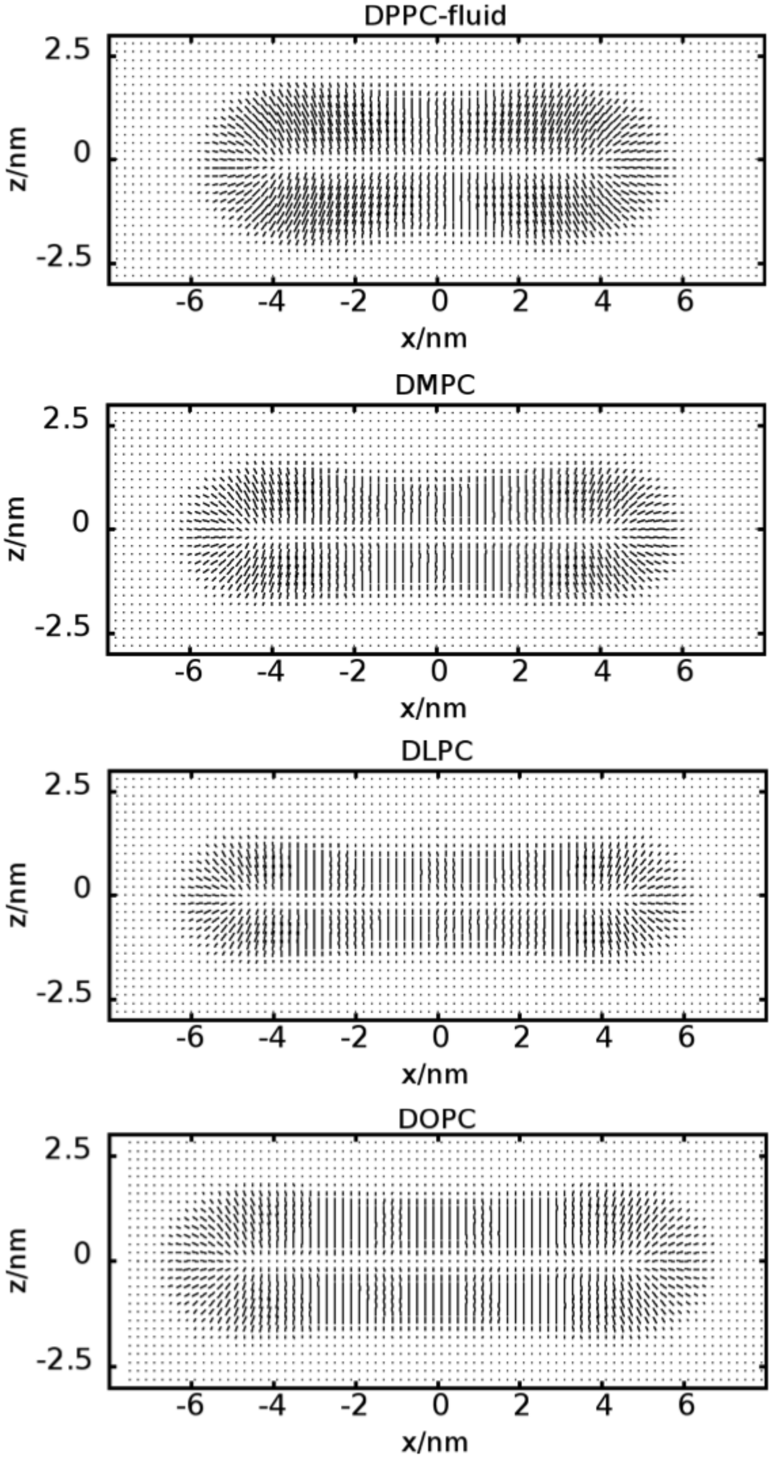

Figure 6.6: Tail orientation plots - for four lipid ribbons, averaged over centered, aligned frames taken at 250 ps increments over MD trajectories. Segment lengths are proportional to the product of tail site density and degree of alignment as described in Methods.

6.4 Conclusions

The edge tensions of bilayers have been determined for a series of PC lipids using atomistic and united-atom molecular dynamics simulations of bilayer ribbons. In the case of DOPC, the values obtained using three different forcefields coincided closely near 45 pN, a value that is over 50% higher than the upper limit of the broad range of experimentally determined values. Besides the real possibility that finite-size effects or shortcomings common to all three forcefields are responsible for this discrepancy, another plausible explanation for the discrepancy is the ability of low-level impurities to reduce edge tension in the experimental systems. Edge tensions decreased with increasing tail length, with the exception of the DPPC system near its transition temperature. Edge tensions were greater for mono-unsaturated tail lipids than for saturated tail lipids with the same number of tail carbons. Edge tension could be correlated roughly with the degree of area expansion associated with forming the edge, although the definition of the area expansion involved an unknown parameter related to the surface at which the area was measured. Tail properties influenced edge tension both through setting the overall thickness and through influences on packing at the edge; in general, saturated tail lipids were better able to adapt the local bilayer thickness near the edge to reduce the area expansion per headgroup. The DPPC lipid near its transition temperature showed a distinct herringbone tilt pattern near the edge; this mode of accommodation may help explain the apparent ordering that occurs near edges in supported bilayers.

References

[1] Peter Fromherz. Lipid-vesicle structure: Size control by edge-active agents. *Chemical Physics Letters*, 94(3):259 – 266, 1983. 120, 132

[2] Christiane Taupin, Maya Dvolaitzky, and Claude Sauterey. Osmotic pressure-induced pores in phospholipid vesicles. *Biochemistry*, 14(21):4771–4775, 1975. 120, 121

[3] Doncho V. Zhelev and David Needham. Tension-stabilized pores in giant vesicles: determination of pore size and pore line tension. *Biochimica et Biophysica Acta (BBA) - Biomembranes*, 1147(1):89–104, 1993. 120

[4] W. Harbich and W. Helfrich. Alignment and opening of giant lecithin vesicles by electric fields. *Z. Naturforsch., A: Phys. Sci.*, 34:1063–1065, 1979.

[5] L.V. Chernomordik, M.M. Kozlov, G.B. Melikyan, I.G. Abidor, V.S. Markin, and Yu.A. Chizmadzhev. The shape of lipid molecules and monolayer membrane fusion. *Biochimica et Biophysica Acta (BBA) - Biomembranes*, 812(3):643 – 655, 1985.

[6] I. Genco, A. Gliozzi, A. Relini, M. Robello, and E. Scalas. Electroporation in symmetric and asymmetric membranes. *Biochimica et Biophysica Acta (BBA) - Biomembranes*, 1149(1):10–18, 1993. 131

[7] J.D. Moroz and P. Nelson. Dynamically stabilized pores in bilayer membranes. *Biophysical Journal*, 72(5):2211 – 2216, 1997.

[8] O. Sandre H. Guitouni Karatekin, E., P.-H. Puech N. Borghi, and F. Brochard-Wyart. Cascade of transient pores in giant vesicles: line tension and transport. *Biophys. J.*, 84:1734–1749, 2003. 121, 131, 132

[9] Evan Evans, Volkmar Heinrich, Florian Ludwig, and Wieslawa Rawicz. Dynamic tension spectroscopy and strength of biomembranes. *Biophysical Journal*, 85(4):2342 – 2350, 2003. 135

[10] Narayanan Srividya and Subra Muralidharan. Determination of the line tension of giant vesicles from pore-closing dynamics. *The Journal of Physical Chemistry B*, 112(24):7147–7152, 2008. 121

[11] T Portet and R Dimova. A new method for measuring edge tensions and stability of lipid bilayers: Effect of membrane composition. *Biophys. J.*, 99:3264–3273, 2010. 121, 131, 132

[12] D. Peter Tieleman, Hari Leontiadou, Alan E. Mark, and Siewert-Jan Marrink. Simulation of pore formation in lipid bilayers by mechanical stress and electric fields. *Journal of the American Chemical Society*, 125(21):6382–6383, 2003. 121

[13] Hari Leontiadou, Alan E. Mark, and Siewert J. Marrink. Molecular dynamics simulations of hydrophilic pores in lipid bilayers. *Biophysical Journal*, 86(4):2156–2164, 2004. 121

[14] T. V. Tolpekina, W. K. den Otter, and W. J. Briels. Nucleation free energy of pore formation in an amphiphilic bilayer studied by molecular dynamics simulations. *The Journal of Chemical Physics*, 121(23):12060–12066, 2004. 121

[15] J. Wohlert, W. K. den Otter, O. Edholm, and W. J. Briels. Free energy of a trans-membrane pore calculated from atomistic molecular dynamics simulations. *The Journal of Chemical Physics*, 124(15):154905, 2006. 122, 135

[16] Frank Y. Jiang, Yann Bouret, and James T. Kindt. Molecular dynamics simulations of the lipid bilayer edge. *Biophysical Journal*, 87(1):182–192, 2004. 121, 122

[17] B. Hess, C. Kutzner, D. van der Spoel, and E. Lindahl. Gromacs 4: Algorithms for highly efficient, load-balanced, and scalable molecular simulation. *J. Chem. Theory Comput.*, 4:435–447, 2008. 123

[18] O. Berger, O. Edholm, and F. Jahnig. Molecular dynamicssimulations of a fluid bilayer of dipalmitoylphosphatidylcholine at full hydration, constant pressure, and constant temperature. *Biophysical Journal*, 72:2002–2013, 1997. 123, 130

[19] Jason de Joannis, Patrick S. Coppock, Fuchang Yin, Makoto Mori, Absalom Zamorano, and James T. Kindt. Atomistic simulation of cholesterol effects on miscibility of saturated and unsaturated phospholipids: Implications for liquid-ordered/liquid-disordered phase coexistence. *Journal of the American Chemical Society*, 133(10):3625–3634, 2011. 123, 130

[20] See-Wing Chiu, Sagar A. Pandit, H. L. Scott, and Eric Jakobsson. An improved united atom force field for simulation of mixed lipid bilayers. *The Journal of Physical Chemistry B*, 113(9):2748–2763, 2009. 123, 130

[21] Jeffery B. Klauda, Richard M. Venable, J. Alfredo Freites, Joseph W. OConnor, Douglas J. Tobias, Carlos Mondragon-Ramirez, Igor Vorobyov, Alexander D. MacKerell, and Richard W. Pastor. Update of the charmm all-atom additive force field for lipids: Validation on six lipid types. *The Journal of Physical Chemistry B*, 114(23):7830–7843, 2010. 123, 130

[22] Par Bjelkmar, Per Larsson, Michel A. Cuendet, Berk Hess, and Erik Lindahl. Implementation of the charmm force field in gromacs: Analysis of protein stability effects from correction maps, virtual interaction sites, and water models. *Journal of Chemical Theory and Computation*, 6(2):459–466, 2010. 123, 130

[23] H.J.C. Berendsen, J.P.M. Postma, W.F. Gunsteren, and J. Hermans. Interaction models for water in relation to protein hydration. In Bernard Pullman, editor, *Intermolecular Forces*, volume 14 of *The Jerusalem Symposia on Quantum Chemistry and Biochemistry*, pages 331–342. Springer Netherlands, 1981. 123

[24] H. J. C. Berendsen, J. R. Grigera, and T. P. Straatsma. The missing term in effective pair potentials. *The Journal of Physical Chemistry*, 91(24):6269–6271, 1987. 123

[25] William L. Jorgensen, Jayaraman Chandrasekhar, Jeffry D. Madura, Roger W. Impey, and Michael L. Klein. Comparison of simple potential functions for simulating liquid water. *The Journal of Chemical Physics*, 79(2):926–935, 1983. 123

[26] H. J. C Berendsen, J. P. M Postma, A DiNola, and J. R Haak. Molecular dynamics with coupling to an external bath. *J. Chem. Phys.*, 81:3684 – 3690, 1984. 123

[27] B. Hess, H. Bekker, H. J. C. Berendsen, and J. Fraaije. Lincs: A linear constraint solver for molecular simulations. *J. Comput. Chem*, 18:1463–1472, 1997. 124

[28] S Miyamoto and P. A Kollman. Settle: An analytical version of the shake and rattle algorithms for rigid water models. *J. Comput. Chem.*, 13:952–962, 1992. 124

[29] U. Essman, L. Perera, M. L. Berkowitz, T. Darden, H. Lee, and L. G. Pedersen. A smooth particle mesh ewald method. *J. Chem. Phys.*, 103:8577–8592, 1995. 124

[30] M.C. Phillips, B.D. Ladbrooke, and D. Chapman. Molecular interactions in mixed lecithin systems. *Biochimica et Biophysica Acta (BBA) - Biomembranes*, 196(1):35 – 44, 1970. 125

[31] Patrick S. Coppock and James T. Kindt. Determination of phase transition temperatures for atomistic models of lipids from temperature-dependent stripe domain growth kinetics. *The Journal of Physical Chemistry B*, 114(35):11468–11473, 2010. 125, 139

[32] Daan Frenkel and Smit Berend. *Understanding Moelcular Simulation: From Algorithms to Simulations*, volume 1. Academic Press, London, 2002. 125

[33] Thomas J. Piggot, ngel Pieiro, and Syma Khalid. Molecular dynamics simulations of phosphatidylcholine membranes: A comparative force field study. *Journal of Chemical Theory and Computation*, 8(11):4593–4609, 2012. 130

[34] Durba Sengupta, Hari Leontiadou, Alan E. Mark, and Siewert-Jan Marrink. Toroidal pores formed by antimicrobial peptides show significant disorder. *Biochimica et Biophysica Acta (BBA) - Biomembranes*, 1778(10):2308 – 2317, 2008. 130

[35] Grinnell Jones and Wendell A. Ray. The surface tension of solutions of electrolytes as a function of the concentration. i. a differential method for measuring relative surface tension. *Journal of the American Chemical Society*, 59(1):187–198, 1937. 132

[36] Mohamed N. Triba, Dror E. Warschawski, and Philippe F. Devaux. Reinvestigation by phosphorus {NMR} of lipid distribution in bicelles. *Biophysical Journal*, 88(3):1887 – 1901, 2005. 132

[37] Hao Wang, Jason de Joannis, Yong Jiang, Jeffrey C. Gaulding, Birgit Albrecht, Fuchang Yin, Kunal Khanna, and James T. Kindt. Bilayer edge and curvature effects on partitioning of lipids by tail length: Atomistic simulations. *Biophysical Journal*, 95(6):2647–2657, 2008. 134

[38] R. J. Molotkovsky and S. A. Akimov. Calculation of line tension in various

models of lipid bilayer pore edge. *Biochemistry (Moscow) Supplement Series A: Membrane and Cell Biology*, 26:149–159, 2009. 135

[39] Erik Lindahl and Olle Edholm. Mesoscopic undulations and thickness fluctuations in lipid bilayers from molecular dynamics simulations. *Biophysical Journal*, 79(1):426 – 433, 2000. 135, 136

[40] Jianjun Pan, Stephanie Tristram-Nagle, Norbert Kuerka, and John F. Nagle. Temperature dependence of structure, bending rigidity, and bilayer interactions of dioleoylphosphatidylcholine bilayers. *Biophysical Journal*, 94(1):117 – 124, 2008. 135

[41] Norbert Kuerka, Yufeng Liu, Nanjun Chu, Horia I. Petrache, Stephanie Tristram-Nagle, and John F. Nagle. Structure of fully hydrated fluid phase DMPC and DLPC lipid bilayers using x-ray scattering from oriented multilamellar arrays and from unilamellar vesicles. *Biophysical Journal*, 88(4):2626 – 2637, 2005. 135

[42] Mario Orsi, Julien Michel, and Jonathan W Essex. Coarse-grain modelling of dmpc and dopc lipid bilayers. *Journal of Physics: Condensed Matter*, 22(15):155106, 2010. 136

[43] Jacob N. Israelachvili, D. John Mitchell, and Barry W. Ninham. Theory of self-assembly of hydrocarbon amphiphiles into micelles and bilayers. *J. Chem. Soc., Faraday Trans. 2*, 72:1525–1568, 1976. 136

[44] May. A molecular model for the line tension of lipid membranes. *Eur. Phys. J. E*, 3:37–44, 2000. 136

[45] Erik Lindahl and Olle Edholm. Spatial and energetic-entropic decomposition of surface tension in lipid bilayers from molecular dynamics simulations. *The Journal of Chemical Physics*, 113(9):3882–3893, 2000. 136

[46] Samuli Ollila, Marja T. Hyvnen, and Ilpo Vattulainen. Polyunsaturation in lipid membranes: dynamic properties and lateral pressure profiles. *The Journal of Physical Chemistry B*, 111(12):3139–3150, 2007.

[47] Justin Gullingsrud and Klaus Schulten. Lipid bilayer pressure profiles and mechanosensitive channel gating. *Biophysical Journal*, 86(6):3496 – 3509, 2004.

[48] Michael Patra. Lateral pressure profiles in cholesteroldppc bilayers. *European Biophysics Journal*, 35(1):79–88, 2005. 136

[49] A. Goebel and K. Lunkenheimer. Interfacial tension of the water/n-alkane interface. *Langmuir*, 13(2):369–372, 1997. 138

[50] Michal Bachar, Patrick Brunelle, D. Peter Tieleman, and Arvi Rauk. Molecular dynamics simulation of a polyunsaturated lipid bilayer susceptible to lipid peroxidation. *The Journal of Physical Chemistry B*, 108(22):7170–7179, 2004. 138

[51] Andreia M. Smith, Madhuri Vinchurkar, Niels Gronbech-Jensen, and Atul N. Parikh. Order at the edge of the bilayer: Membrane remodeling at the edge of a planar supported bilayer is accompanied by a localized phase change. *Journal of the American Chemical Society*, 132(27):9320–9327, 2010. 139

[52] Shan-Shan Qin, Zhi-Wu Yu, and Yang-Xin Yu. Structural characterization on the gel to liquid-crystal phase transition of fully hydrated dspc and dspe bilayers. *The Journal of Physical Chemistry B*, 113(23):8114–8123, 2009. 139

7

Oleic acid (OA) capped CdSe quantum dots embedded in the lipid bilayer- A united-atom simulation description

7.1 Introduction

Several recent reviews explore the motivation and the common uses of quantum dots (QDs) and metal nanoparticles (NPs) in biological applications. (1–5) The class of materials commonly referred to as nanocrystals or "quantum dots" (QD) consist of a semiconductor core coated by an organic surfactant layer. In literature the passivating surfactant layer is also referred to as "ligands" or "capping agents". The semiconductor component, typically composed of group II-VI or III-V elements, has size dependent, unique optical properties. (6–12) These properties include broad absorption spectra, narrow emission bands whose frequency depends on QD size.

Relative to molecular dyes, they are more photostable and have longer fluorescence excitation lifetimes. The fluorescence properties of quantum dots have been exploited in several ways. In FRET experiments quantum dots were able to track changes in distances between interacting molecules. In molecule targeting experiments, the surface of the quantum dot was engineered as to bind specific DNA/mRNA sequences, to label specific proteins or fibers during key reactions and interactions, to initiate antigen to antibody recognition events, and to adhere to specific surface cell receptors.

Often quantum dots and nanoparticles must interact or cross the enclosing cell membrane in order to reach specific targets. Size, shape, and the charge/polar character of the passivating surfactant layer, all affect the manner in which quantum dots or nanoparticle interact with lipid membranes . (13–17) The charges of the lipid headgroups themselves and the elastic properties of the lipid membranes also play a role. Rod-like structure cannot cross the lipid membranes as well as spherically shaped nanoparticles. (18) Charged nanocrystals, especially positively charged nanocrystals, favor lipid bilayer translocation. Typical translocation mechanisms consist in inducing localized pores in the lipid bilayers or in thinning and subsequent breaking of the membrane (19). Neutral nanoparticles prefer the hydrophilic phase and may be used during instances where no membrane interaction is preferred. (17) Nanoparticles capped with both hydrophilic and hydrophilic character ligands reside at the interfacial region.

Quantum dots and metal NPs can be transported across cell membranes inside the lumen of large unimellar vesicles (LUVs) or liposomes, structures commonly used as molecular delivery systems. Several experimental reports from the past decade showed that both metal NPs and QDs structures passivated by hydrophobic ligands may also be embedded inside the hydrophobic acyl chain wall of the liposome. Successful QD incorporation requires employing hydrophobic capping ligands and also small nanoparticle size (<6-7 nm total size (20)), the later needed to minimize hydrophobic mismatch between the two monolayer leaflets.

The first report on incorporating nanoparticles inside the liposome wall was from

English and co-workers.(21) They employed octanol covered silicon NPs in the 2.5-3.5 nm range. The nanoparticles were found to reside either completely buried inside the hydrophobic layer or partially exposed to the surface. Small hydrophobic-coated quantum dots have also been successfully embedded inside the hydrophobic wall of the liposome. In one example a ~ 3 nm CdSe QD, TOPO coated was successfully embedded in the wall of large unimellar vesicles (LUVs) (22). The surface of the liposome was further engineered as to either fuse with the plasma membrane, and direct the quantum dot fluorescent probes to reside inside the native plasma membrane, or as to have the intact QD carrying liposome translocate inside the cellular cytoplasm. In the latter case, the LUV system can be engineered to also transport a molecule of interest (such as a drug molecule) across the lipid bilayer. The incorporation of the quantum dots inside the lipid bilayer is believed to disrupt both the lipid headgroup packing and neighboring lipid tail monolayer structure. In some cases may lead to unzipping of the two monolayers, an event that in turn furthers nanoparticle aggregation.(23, 24)

From theoretical models (20) wrapping of the two monolayers around QDs is enabled by both monolayer ability to bend and also its ability to stretch. Elastic material constants such as bending moduli (k) and area stretching moduli (K_a), along with monolayer spontaneous curvature (c_o), and monolayer thicknesses (t) are expected to play a role with respect to size of QDs that are possible to embed. Several simulation studies characterizing the interactions of lipid bilayers with metal nanoparticles have been reported. (17, 25–27) These studies show how the presence of nanoparticles affect the lipid tail configuration state such as the gel-fluid transition of dipalmitoyl phosphatidylcholine (DPPC) bilayers, and also how the nature of electrostatic charges or hydrophobic character of the ligands modulate the membrane-nanoparticles interfacial interaction as well as the nanoparticle translocation. For quantum dots systems in lipid bilayers, all published studies so far have used coarse-grained force-fields to describe the interactions of both lipids and ligands.

In a recent study Zheng and co-workers (28) investigated the photo-oxidation of 3.0 nm diameter CdSe QDs passivated by oleic acid when embedded in the wall of small unilamellar vesicles (170 nm SUVs) of different phase lipids. Their study found increased stability to photoxidation when the QDs were embedded in gel lipid distearoyl phosphatidylcholine (DSPC) compared to fluid phase distearoyl phosphatidylcholine (DOPC) (or near-phase transition dimyristoyl phosphatidylcholine (DMPC)). The observed phenomenon was explained as DSPC lipid/ligand interface confining the oxides to the surface of the quantum dot. Their study also showed selective ligand exchange with SUVs lipid type. When QDs were embedded in fluid lipid DOPC, several longer length SH-(PEG)$_{82}$-Cy5 molecule successfully replaced the QD native ligands. At the same added new ligand concentration, no successful native ligand exchange process was observed in the QD/DSPC case.

The structural conformation of lipids interacting with ligands of quantum dot and that of ligands passivating the nanocrystals can be characterized in simulations. To date understanding the ligand/lipid interface associated with quantum dots (QDs) positioned inside the lipid bilayers from simulation work with an united atom (UA) or all atom (AA) level description proved challenging. Tens of thousands of water molecules are needed in order to properly hydrate the bilayer embedded QD system. The advent of efficient, scalable parallel codes made it possible to attempt such an implementation. In this work we present findings from incorporating two different size QDs, 2.6 nm and 3.4 nm diameter wurtzite CdSe quantum dots capped with oleic acid ((9**Z**)-octadec-9-enoic acid ot OA) in dilauroyl phosphatidylcholine (DLPC), DMPC, DOPC, and DSPC lipid bilayers from simulations using a united atom (UA)) description of all components involved. The choice of embedding lipids allows understanding of how bilayer thicknesses and phase of lipid tail couple with size and degree of passivation of embedding nanoparticle. The thicknesses of the chosen monolayers embedding the QD should also influence the manner of accommodating the passivating ligands.

We are interested to understand the static and the dynamic conformational changes in lipid tails that occurs in order to accommodate the QD nanocrystals. Characterizing the spatial distribution of oleic acids ligands is also useful to better understand the access to QD surface during ligand exchange processes. At the same QD size, two different capping ligand densities are employed. Changes in lipid bilayer properties with varying the quantum dots initial embedding orientation with respect to the L_Z bilayer normal are also examined.

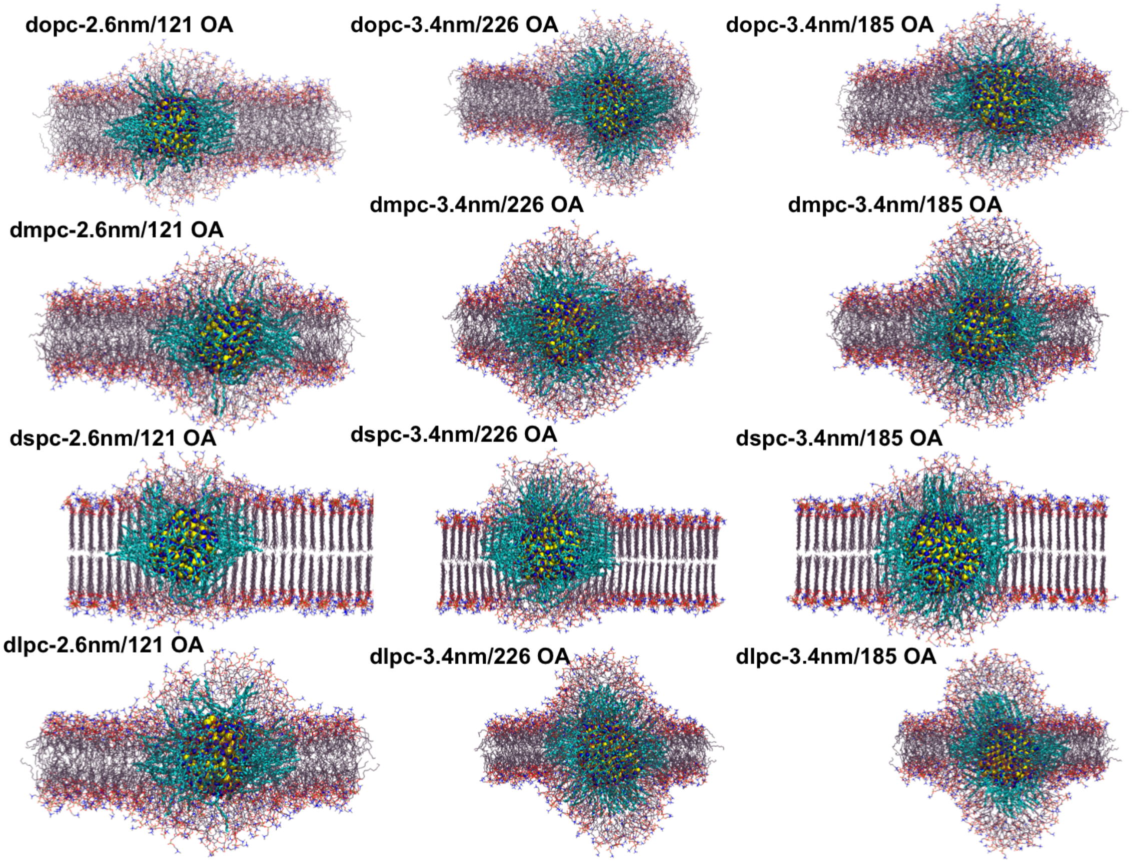

Figure 7.1: Snapshots of quantum dots embedded in DSPC, DMPC(V-state), DOPC, and DLPC - The simulation instances at t=100 ns are displayed ; - XZ plane view

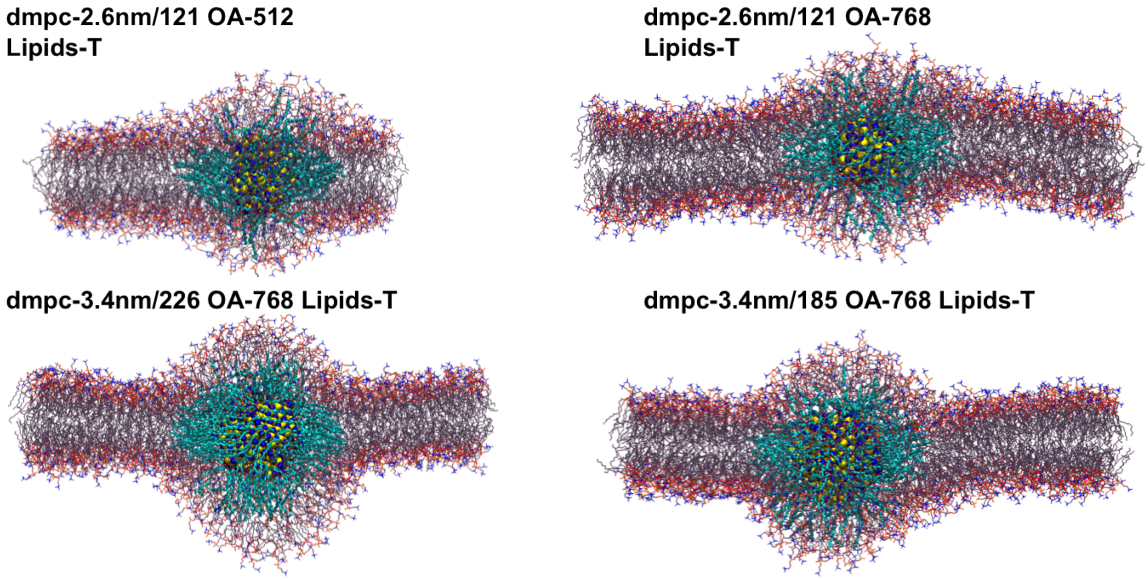

dmpc-2.6nm/121 OA-512 Lipids-T

dmpc-2.6nm/121 OA-768 Lipids-T

dmpc-3.4nm/226 OA-768 Lipids-T

dmpc-3.4nm/185 OA-768 Lipids-T

Figure 7.2: Snapshots of quantum dots incorporated in DMPC, T-state orientation - The simulation configurations at t=100 ns instance are shown ; -XZ plane view

7.2 Methods

7.2.1 Oleic acid capped -nanocrystal preparation-

The initial coordinates of ~ 1.2 aspect ratio prolate shaped, Cd rich CdSe quantum dots were generated from sculpting into an wurtzite lattice with constants a = 0.43 nm and c=0.701 nm (29). The 100 nanocrystal facet (for a full description of CdSe nanocrystal surface notation see Rosenthal et. all (30)) was left as Cd and Se terminated with Se atom having a single dangling bond. All other nanocrystal surfaces are terminated in Cd atoms. The 2.6 nm diameter quantum dot has a 462 total number of atoms and a 1.25 Cd:Se stoichiometric ratio. The ~ 3.4 nm QD has a total of 918 atoms and a 1.21 Cd:Se ratio.(29) The Cd atom interacts with the Se atom via both pairwise long-range electrostatic interactions and short-range LJ interactions as described in the Rabani force-field (29). The total numbers of ligands capping the 2.6 nm nanocrystal is 121 oleic acid (OA) molecules, number that results from coordinating each surface Cd atom in a divalent manner to the oxygen atoms on the ligands. Two ligand capping densities were implemented to cover the 3.4 nm nanocrystal surface, more specifically 185 OA ligand molecules and 226 OA ligands. The Berger united atom (UA) force-field parameter description (31, 32) was enforced for the OA ligand, the typical representation used for the 18:1(9Z) tail of POPC lipid. The Cd-O bond is implemented as a harmonic bond with an equilibrium inter-separation of 0.24 nm. Increasing the negative partial charges on the oleic acid oxygen atoms counterbalanced the extra charge due to excess Cd surface atoms present in the system.

The ligands were combined with the bare CdSe nanocrystal in the following manner. First the tail of an oleic acid was stretched out to a linear configuration preserving the cis-kink found at the C_9-C_{10} position. The extended ligands were placed with the carboxyl group oxygen atoms at a 0.24 nm distance from a quantum dot surface Cd bonding partner using an in-house developed perl script. The ligand shell of fully capped quantum dot was next relaxed in vacuum during a 1 ns molecular dynamics (MD), NVT ensemble simulation while keeping the nanocrystal structure frozen. The MD simulation runs were done using the Gromacs-4.5.4 simulation software. (33) This package implements the leap-frog scheme for integrating Newton's equations of motion. The temperature was maintained at 300 K using the Berendsen thermostat and a 0.1 ps time constant. (34) Periodic boundary conditions (*pbc*) were implemented in all three Cartesian directions. A 2 fs time step was used in simulation. The electrostatic interactions were treated via the PME algorithm with a 0.12 grid spacing and cubic interpolation. (35) A cut-off of 1.0 nm was used for the van-der-Waals interactions. At the end of the simulation run, the initial ligand orientation appeared completely melted and the nanocrystal displayed homogenous monolayer coverage.

7.2.2 Combining the capped nanocrystals with lipid bilayers, MD Parameters

In most cases (table 7.1) a 128 lipid bilayer was replicated by 2 x 2 x 1 using the *genconf* utility of Gromacs to yield a total 512 lipids assembled into a 12 x 12 nm patch. The coordinates of the solvated upper lipid monolayer were translated in the Z-direction by 7 nm. The quantum dot was placed between the two leaflets having the orientation T-state or V-state described in table 7.1. The embedding orientations refer to placing the QDs between the two lipid monolayers with its prolate major axis parallel to bilayer normal, the V state or perpendicular to bilayer normal, the T state. The monolayers were next closed to form the bilayer structure via an applied pressure in the Z-direction, while keeping a fixed $L_x \times L_y$ area. The leaflets closed thus embedding the quantum dot in 20-50 ps simulation time. The resulting lipid bilayer-QD structures were sampled in $\sim$ 150 ns NPT molecular dynamics simulations. The CdSe nanocrystal structure was no longer kept frozen during the MD runs. We also observed the previously reported, two outermost nanocrystal surface layers reconstructions (29). The Berger force-field (31) described the lipid interactions and the SPC water model was implemented for the water solvent. The temperature was kept fixed at 300 K using the Berendsen thermostat and a 0.1 ps time constant. For all lipid systems (except DSPC) the pressure was kept fixed at 1.0 bar using the Berendsen barostat (τ_p =1.0 ps, $4.5e^{-5}$ bar $^{-1}$ compressibility values) and the semiisotropic pressure coupling scheme. The electrostatic interactions were computed via the PME scheme using a 0.12 nm grid spacing. The cut-off for the Van der Waals interaction was 0.9 nm. The covalent bonds of lipids and those of OA molecule were constrained via the LINCS algorithm. (36) The SETTLE algorithm (37) was utilized in constraining the bonds of water molecules.

The initial DSPC bilayer gel configuration was previously realized and characterized in our own group. (38) The production MD simulation conditions differ for the DSPC bilayer in that the Berendsen anisotropic coupling scheme was implemented (τ_p =2.0 ps) that allowed for changes of box/angle dimensions in all three Cartesian directions. For the data analysis purposes, in order to insure QD-lipid bilayer equilibration, the first 100 ns of MD simulation were excluded for all systems composed of 512 lipids. The frames used during the analysis (50ns in all cases) were sampled across the trajectory at a 15-40 ps resolution.

7.2.3 Analysis Method

For data analysis purposes, in order to insure QD-lipid bilayer equilibration, the first 100 ns of MD simulation were excluded fo all systems. The tilting of the quantum dot (table 7.1 last column and figure 7.7) was determined using the *g_bundle* utility of Gromacs software package in the following manner. First the top Se layer atom coordinates and the lowest Se layer atom coordinates of the Cd terminated quantum dot are selected. The xz-center of mass of each of the two layers is calculated and an axis/vector is constructed from the newly calculated center of mass points. The tilting angle reported in table 7.1 is the angle between the newly inter-layer created

Table 7.1: Overview of simulated systems

	Water/Lipid Ratio	QD Size (nm)	Time (ns)	Embedding State	QD orientation Φ_Z (°)
DLPC	63.1	2.6	150	V	37.5 ± 4.4
DLPC	108.9^b	3.4	150	V	15.6 ± 2.5
DLPC	107.5^c	3.4	150	V	29.3 ± 2.4
DMPC	61.1	2.6	150	V	42.4 ± 3.1
DMPC	61.1	2.6	150	T	120.0 ± 4.0
DMPC	62.9^a	2.6	150	T	100.0 ± 3.5
DMPC	108.7^b	3.4	150	V	32.6 ± 4.0
DMPC	$86.0^{a,b}$	3.4	130	T	66.5 ± 2.0
DMPC	104.5^c	3.4	150	V	27.0 ± 2.9
DMPC	85.8^c	3.4	120	T	84.2 ± 2.0
DOPC	54.4	2.6	150	V	38.9 ± 4.0
DOPC	89.6^b	3.4	150	V	27.2 ± 2.4
DOPC	100.1^c	3.4	150	V	62.8 ± 3.0
DSPC	60.6	2.6	150	V	24.9 ± 1.3
DSPC	60.6^b	3.4	150	V	18.4 ± 1.4
DSPC	104.4^b	3.4	150	V	22.5 ± 1.4
DSPC	103.7^c	3.4	150	V	37.2 ± 2.5

a=768 lipids unit cell, b= 226 OA, c= 185 OA

vector and the z-axis bilayer normal.

The phosphorus (P) atom number density from figure 7.3 corresponds to selecting all lipids from near QD outward to the extent of bilayer-like thickness recovery, in a cylinder geometry. The number of cylindrical slices along L_Z direction was 100. To center the calculated density at zero, the center of mass along the Z direction of the CdSe/OA assembly was subtracted and averaged over the last 50 ns of the trajectories.

The distance dependent deuterium order parameters reported in figures 7.4-7.5 were constructed by selecting circular concentric shells outward from the embedding location of the QDs. Saturated lipid tails order reported values were determined via the *g_order* program of Gromacs. The values corresponding to DOPC unsaturated carbons were calculated using a different version of *g_order* that was modified further (39) to correctly calculate the order parameters corresponding to these atoms.The center of mass of CdSe nanocrystal and that of its passivating OA ligands, (x_{com}, y_{com}) in the xy plane were determined for each frame sampled across trajectories at a 15-40 ps resolution. The (x_{com}, y_{com}) point is used as a center point when counting the lipids as concentric shells. The (x, y) coordinates of the phosphorous (P) atoms of each frame were also selected and used to determine which lipids belong to a specific concentric shell. A typical lipid bilayer shell used in order parameter calculations is shown in figure 7.8.

The calculations were conducted for the $sn-1$ tail and $sn-2$ tail separately and then the final values were averaged over the last 50 ns trajectory sections. The formulas for order parameter of a fluid phase lipid bilayer that can be related to deuterium order parameter found in experiments is (40):

$$-S_{CD} = (\frac{2}{3}S_{xx} + \frac{1}{3}S_{yy}) \tag{7.1}$$

$$S_{xx(yy)} = \frac{2}{3}\left\langle \left(e_{ix(y)} \cdot e_{ix(y)}\right)^2 \right\rangle - \frac{1}{2}$$

$$e_{ix(y)} = \frac{r_{i+1,x(y)} - r_{i-1,x(y)}}{\left|r_{i+1,x(y)} - r_{i-1,x(y)}\right|}$$

r_i is the position vector connecting $C_{i+1}C_{i-1}$ when determining the order parameter for carbon position number i on lipid tail.

Order parameters of intact bilayers were obtained from the simulations of bilayers described in previous chapter in an analogous manner to when calculating the order parameter of a single QD concentric lipid shell. Lipid tail orientational time autocorrelation functions were obtained by first finding the unit vector r_j directed from carbon 4 to carbon 9 on the $sn-2$ lipid tail of each lipid j, then calculating the average autocorrelation function:

$$C_j(t) = \langle r_j\left(\tau\right) \cdot r_j(\tau + t)\rangle \tag{7.2}$$

over the trajectory segment from $\tau = 100$ ns to $\tau = 150$ ns for t up to 25 ns. The averages of $C_j(t)$ were taken over lipids j classified as either bulk-like (far from the QD) or perturbed (near to the QD). Lipids were classified as near or far from the QD based on their radial distance in the xy plane from the QD center-of-mass. The cut-off radius was determined for each structure as the distance at which the lipid bilayer recovered its unperturbed thickness. In the case of DSPC, a subset of lipids within the cut-off radius had gel-like properties; in these, the orientational autocorrelation function persisted above 0.92 over the 25 ns analysis range. These 20-30% of lipids were excluded from the average plotted in figure 7.6.

The first step in determining the water number density introduced in figure 7.8 consists in computing the radial distribution function $g(r)$ between the Cd atom found at the QD center point and the oxygen atom of water molecules. The $g(r)$ function is next multiplied by the bulk water density used to solvate the lipid/QD systems (ρ_{bulk}).

7.3 Results

The positioning of the embedded quantum dot (CdSe/OA) within the lipid bilayer is quantified across all lipid types as number densities vs. L_Z box dimensions in a cylindrical geometry (out to intact bilayer like conformation recovery) and observed asymmetric. Sample data of monolayer embedding preference is presented in figure 7.3. The QD's slight preference for one monolayer leaflet is most pronounced for lipid DSPC at higher ligand capping density or smaller size QD. The bare nanocrystal tilting angles with respect to bilayer normal are summarized in table 7.1 for both initial embedding states, the V-state and the T-state. Across lipid types,when averaging over the last 50 ns of the trajectories, several systems adopt nanocrystal core tilting angle of $\sim 30°$ when larger size nanorcrystals were embedded(figure 7.7:a,d). About ten degrees higher tilting angle were calculated for cases embedding a

2.6 nm diameter core quantum dot (figure 7.7:c).

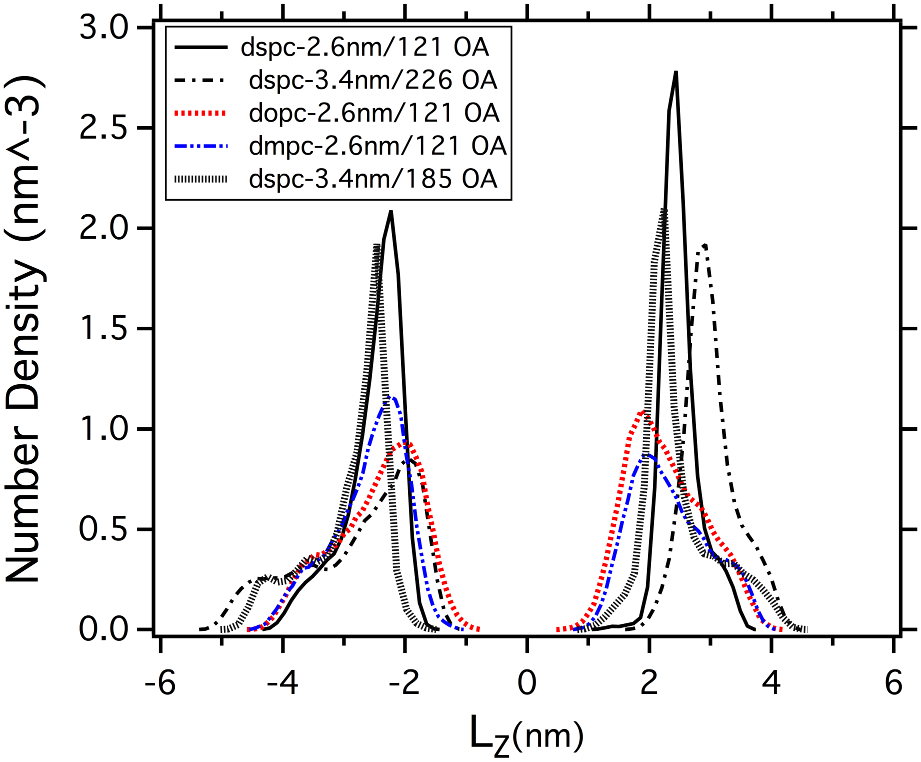

Figure 7.3: Preferred positioning of embedded QDs inside lipid monolayers - Phosphorous (P) density vs. L_Z box dimension of QD embedded in lipid bilayers from sculpting a cylinder of radius ($r_{cut-off}$) around the quantum dot to the point of bilayer like thickness recovery.

At the start of this investigation, we set out to discern the manner in which distortions in lipid tail configurations are influenced by the size of the quantum dot and by the ligand density. Embedded QD distance dependent order parameters are shown in figure 7.4. Each column corresponds to a single lipid type, DOPC, DMPC, and DSPC respectively. The first row is the instance of embedding a 3.4 nm diameter nanocrystal passivated by 185 oleic acid ligands, the second row corresponds to a 3.4 nm diameter QD capped with 226 oleic acid molecules, and the third row shows the order parameter data for the 2.6 nm diameter CdSe QD/121 OA system. This analysis shows that a smaller nanocrystal size and a lower ligand density leads to more ordered lipid tails. The order parameter curves constructed from including the embedded QDs further away lipids show less variability with nanocrystal size. Differences among concentric shells however persist.

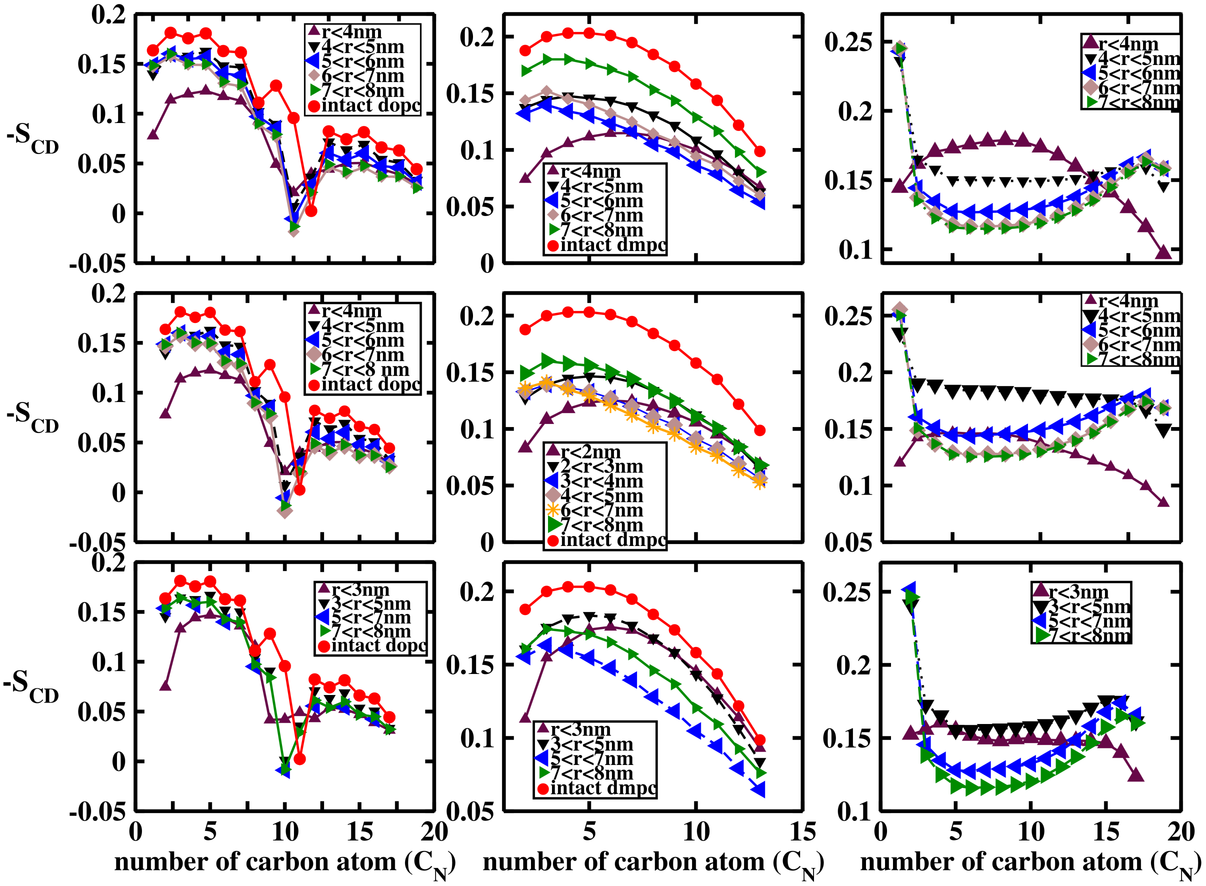

Figure 7.4: Lipid tail ordering with QD size and degree of ligand passivation - Distance dependent order parameter vs. number of tail carbon for QD free lipid bilayer and for QDs embedded in lipid bilayers. Each column correspond to a single lipid type: DOPC left, DMPC center , and DSPC right ; The data across rows refers to changing the QD oleic acid ligand density from 185 OA to 226 OA at same 3.4nm QD size (row 1 vs. row 2) and diameter size from 3.4 nm, 226 OA to 2.6 nm, 121 OA (row 2 vs. row 3).

We also investigated if the manner of initially positioning the nanocrystal between the two monolayers affects the resulting trends in order parameters. Figure 7.5 displays distance dependent order parameters of lipid tails from regions closest to the quantum dot ($r_{cut-off} < 4$nm) at same size embedded QD (2.6 nm) in lipid DMPC.

Less ordered lipid tails are observed in QDs embedded as T-state. The curves are superimposable at distances larger than $r_{cut-off} > 4$nm. Comparable size differences were determined between state V and state T of embedded 3.4nm QD/226 OA and 3.4 nm/185 OA systems with $r_{cut-off} >\sim 6$ nm (data not shown).

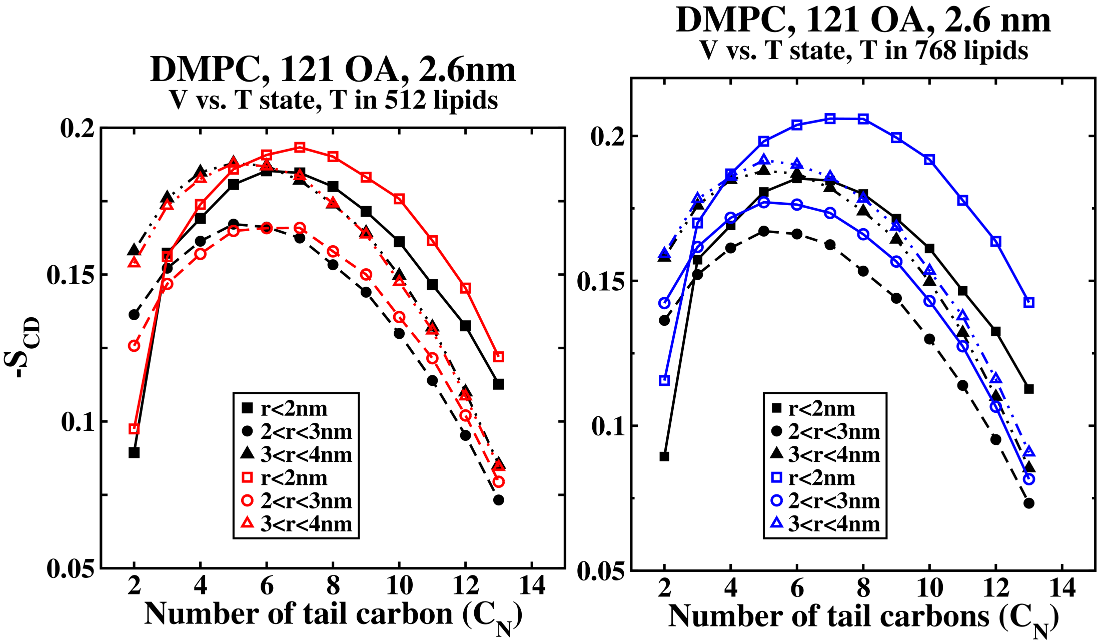

Figure 7.5: Lipid tail ordering with QD embedding orientation - Distance dependent order parameter vs. carbon position in lipid tail - with QD embedding orientation and number of lipids in unit cell. The QD embedding orientation refers to initially (t=0 ns) placing the QD between DMPC monolayers with its prolate major axis either parallel (*black filled symbols*, V state) to bilayer normal or perpendicular (*red or blue clear symbols*, T state) to bilayer normal

Qualitative differences in lipid tail mobility with lipid phase are presented by calculating the decays in the orientational autocorrelation functions of a unit vector constructed between position of carbons four and position of carbon nine (figure 7.6). The left side panel of the figure displays data at same size quantum dot (3.4nm/226 OA) across different phase lipids. Relative to QD free lipid monolayer regions, the presence of the embedded QD in the bilayer enhances the oleic acids nearby DSPC lipid tail mobility, hinders the motion of neighboring DMPC tails, and it is not impairing the movement ability of DOPC tails. The time scales of the autocorrelation decays are found unaffected by both size of embedded quantum dot and degree of nanocrystal passivation. (figure 7.6, right panel).

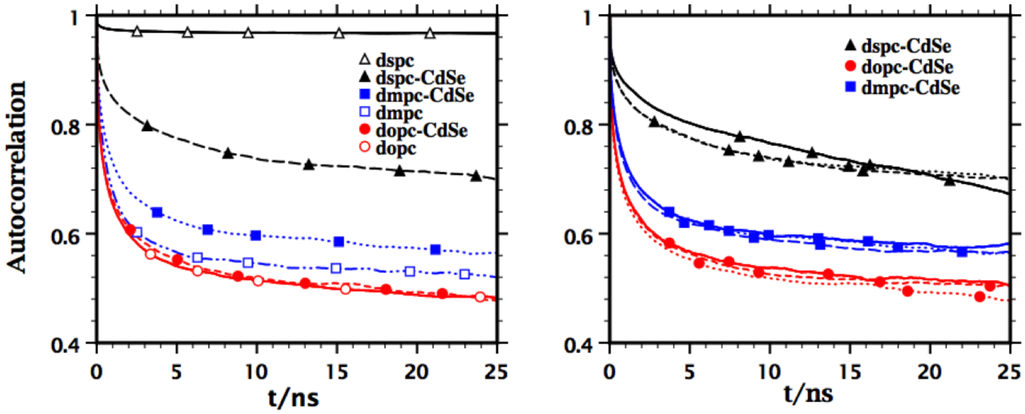

Figure 7.6: Orientational autocorrelation function - Left Panel: Decays in lipid tail unit vector (r_{C_4,C_9}) autocorrelation functions constructed from the last 50 ns trajectory sections. *Red* color, lipid DOPC: 3. 4 nm size QD/226 OA, solid line corresponds to lipids far away from the embedded QD, and dashed line constructed from lipids near QD. *Blue* color, lipid DMPC: 3.4nm QD/226 OA system, dashed line from QD far away lipids, and dotted line from near QD lipids. *Black* color, lipid DSPC: 3.4nm QD /226 OA molecules system, solid line from gel like lipids and the dashed line line from melted lipids. **Right Panel**: Autocorrelation function decay variability with size of nanocrystal and ligand density from lipids that interact with QD passivating ligands: 2.6 nm QD/121 OA solid line, 3.4 nm QD/226 OA dotted line , and 3.4 nm QD/185 OA dashed line.

7.4 Discussion

7.4.1 Embedded Nanocrystal Trajectory Descriptions

As shown in figures 7.1-7.2, in most cases the ligand shell around the 2.6 nm nanocrystals is concentrated laterally (almost bunched) and depleted, disordered, and density wise asymmetric at the two QD poles. A similar oleic acid ligand preference is observed when embedding a 3.4 nm diameter QD but with a higher density of ligand molecules pointing towards the PC headgroups. For larger nanocrystals, a greater fraction of ligands are depleted at the poles and packed laterally when DOPC or DSPC lipid is used compared to DMPC or DLPC lipid. Previous simulations of QD free DMPC, DLPC, DOPC, and DSPC lipid bilayers in similar simulation conditions employed in this investigation or in experiment determined thicknesses values as 3.37 nm, 2.99 nm, 3.69 nm (41) , and 4.7 nm (42) respectively. The more pronounced pole ligand depletion when embedding the larger nanocrystals in DOPC and DSPC can be related to lipid monolayers having larger thicknesses and thus an improved ability to accommodate a higher number of ligands laterally.

Simulations at different initial QD embedding orientation (T-state vs. V-state, figure 7.2) show similar ligand pole bunching thus further confirming that the distribution of ligand is determined mostly by the embedding bilayers and not by the shape of the quantum dot as ligands corresponding to other nanocrystal facets are in direct contact with the DMPC tails.

Simulations at different initial embedding orientation (DMPC, T-state vs. V-state, figure 7.2) further confirm that the distribution of ligand pole bunching is determined mostly by the bilayers and not by the shape of the quantum dot. For smallest size T-state embedded QDs (figure 7.2), the ligand bunching appears similar to when the nanocrystal was prepared in an initial V-state although ligands corresponding to other nanocrystal facets are in direct contact with the DMPC tails.

The average tilting of the quantum dot in each simulation instance across the 50ns analysis trajectory section is summarized in table 7.1. Sample evolutions over the entire trajectories are shown in figure 7.7. Across lipid types the largest tilting angles with respect to bilayer normal are determined in systems incorporating a 2.6 nm diameter nanocrystal, with lowest values recorded in lipid DSPC. The standard deviation of the tilt angle over the 50 ns trajectory segment is also largest for this size QD alluding to the smallest size syste's ability to rotate faster and thus expose ligands to be replaced during ligand exchange processes at a faster rate (figure 7.7c). In all simulation cases, the trajectories of QDs incorporated in DSPC show little variations in tilt angles, thus in gel lipids the embedded QDs are locked in place (fig 7.7: a,c,d).

The DSPC QD/185 OA has a symmetric embedding (figure 7.3) compared to the

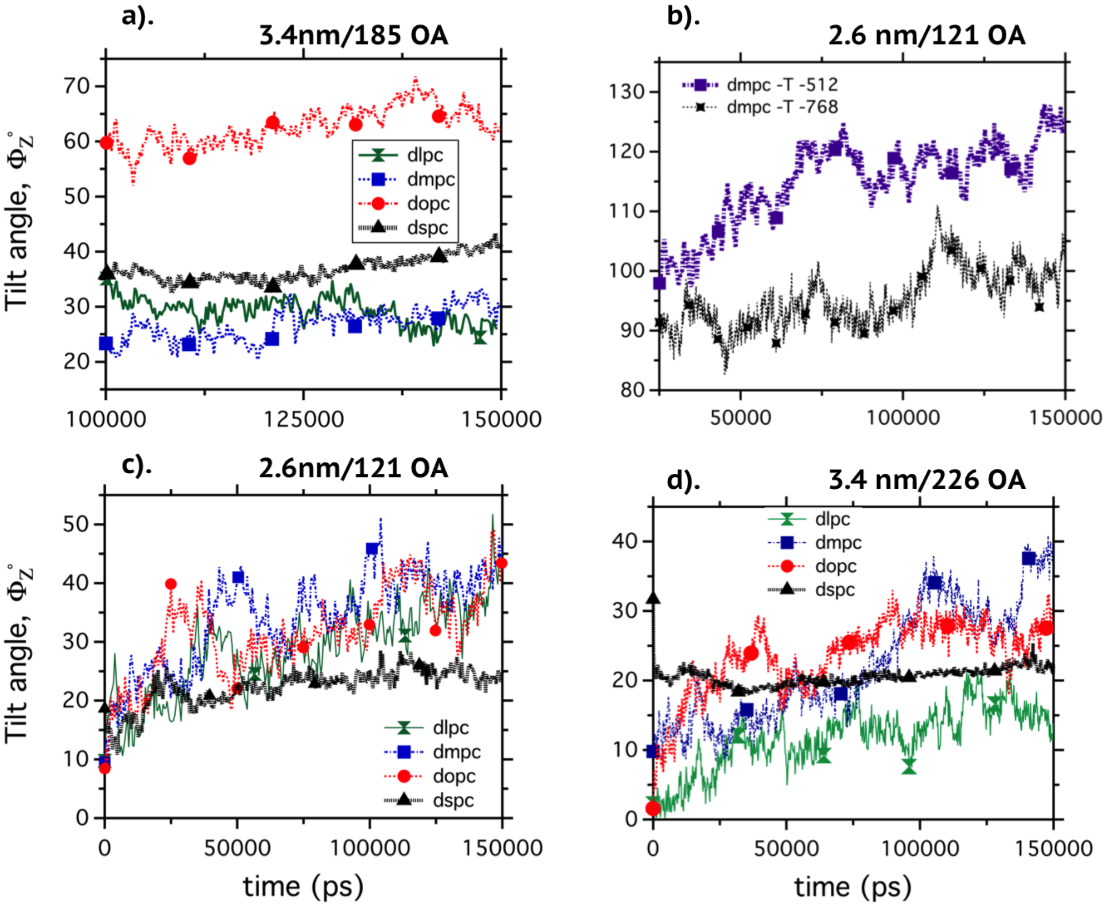

Figure 7.7: Nanocrystal tilt angle vs. time - Evolution of tilt angle with trajectory time across different QDs/lipid systems

other DSPC cases due to more even ligand density populations at the two QD poles. The tilting angle is also the largest for this system suggesting that the ligand populations at the two QD poles and not just the lateral ligand densities versus those facing the PC headgroup can affect the final nanocrystal embedding orientation. The higher valuer in tilt angle of 3.4nm/185 in lipid DOPC (figure 7.7a) corresponds to a tilt angle of $\sim$ 30 degrees with respect to $-L_Z$ and perpendicular to the orientation of the other embedded QDs under similar conditions (3.4 nm CdSe/185 OA in DLPC, DMPC, DOPC).

In addition to ligand population distributions effects mentioned above and nanocrystal size, incomplete equilibration might slightly affect the recorded final angles values and longer simulations should be conducted to investigate further such effects (figure 7.7). Longer simulations would also allow us to quantify fractions of QD pole ligands interacting with wrapping lipids.

QDs incorporated in DSPC gel phase lipid show some unique features. To accommodate OA configurations pointing towards the PC headgroups, several DSPC lipid tails from the region of the quantum dot of this lipid type, take on unconventional conformations, oriented almost perpendicular to the bilayer normal. A percentage of DSPC tails that interact with laterally-oriented OA ligands manage to maintain a gel like structure, but are displaced toward the solvent (figure 7.8).

While a slight embedding asymmetry (figure 7.3) is also observed in DSPC with larger nanocrystal, a more pronounced asymmetry is observed for the $\sim$ 2.6 nm QD. At simulation trajectory time $\tau = 0$, however, the 2.6 nm QD embedded perfectly symmetric. At $\sim$ 10 ns trajectory time, the DSPC monolayers incorporating a 2.6 nm QD already displays significant asymmetry, with the QD exhibiting a preference for one of the leaflets. Also, there are other segments of the 150ns trajectory where more symmetric embedding is observed relative to the average curves displayed in figure 7.3. We also mention that at later trajectory time, $\sim$ 125 ns, the 2.6 nm QD incorporated in DSPC, displayed a topological defect site in that two lipid molecules

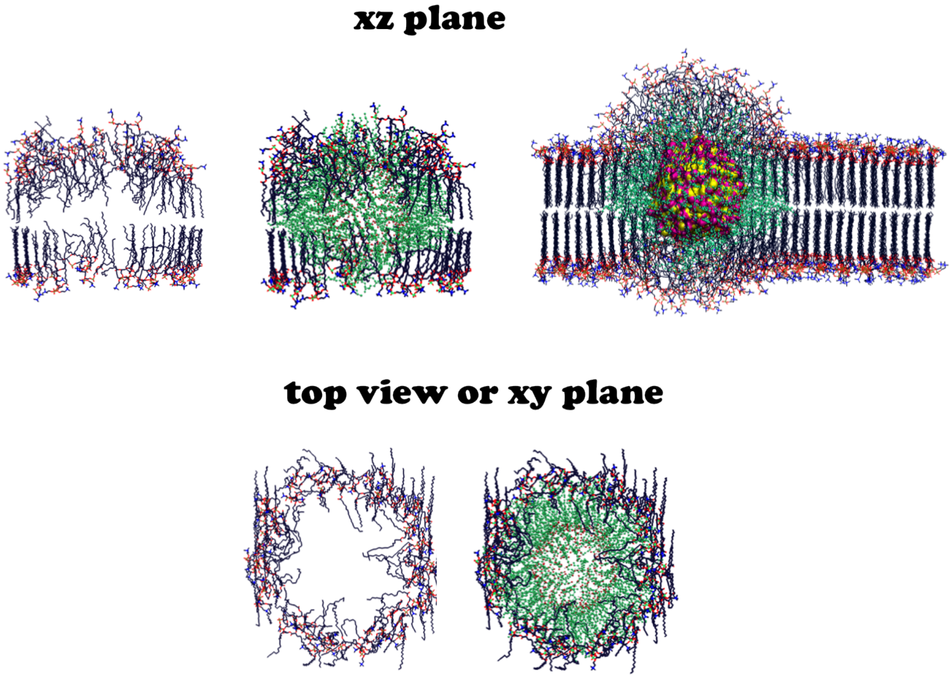

xz plane

top view or xy plane

Figure 7.8: DSPC lipid tail reorientation - Simulation snapshots of concentric shell at τ = 100 ns trajectory instance for DSPC lipid with 3.4nm/226 OA embedded QD to show manner of lipid tails reorientation to accommodate passivating oleic acid ligands. The lipid concentric shell $3nm < r_{cut-off} < 4nm$ is shown apart from the embedded QD (left bottom) and together with the nanocrystal (center, right top) in XZ plane (bilayer normal along Z) and as top view or XY plane (lower panels).

diffused close to the surface of the quantum dot and their headgroups proceeded to passivate one of the QD poles. Along with the two lipids, several water molecules were also able to reach the surface of the quantum dot. At $\sim$ 140 ns trajectory time the two lipids left the surface of the quantum dot and rejoined the wrapping DSPC lipids.

From snapshots of figure 7.1, the regions of the embedded QDs show lower bilayer bending curvature when DSPC lipid is used compared to DOPC, DMPC, and DLPC. Longer simulations could quantify the preferred embedding orientation with ligand density distribution. Output of such longer simulations (300-400 ns) can be used as basis in constructing a molecular model that can then further describe the elasticity of the wrapping monolayers. Input parameters of such a model would also consider ligand spatial distributions and the nanocrystal preferred tilt angles with factors that affect its geometric orientation.

7.4.2 Lipid Tail Disorder

All size diameter embedded nanocrystals lead to a lower lipid order parameter compared to a QD free bilayer patch even at distances far away from embedded QD (figure 7.4 and figure 7.5). A larger number of lipids are recommended be used in the unit cell to insure sufficient relaxation between XZ -QD periodic repeats.

For the 2.6nm QDs systems, the distance dependent order parameters of DOPC lipids selected from a circular patch of 2.0 nm radius relative to center of mass of CdSe/OA appear most disordered. These lipids are in direct contact with QD pole OAs pointing towards the PC headgroups. The ordered parameters constructed with tails from all other concentric shells nearly collapse unto a master curve (figure 7.4, left column). For larger nanocrystal cases, 3.4nm in diameter, a somewhat similar order parameter curve to that of the 2.0 nm radius patch of embedded 2.6nm QD is observed when lipids are amassed together to form a 4 nm radius lipid patch. The order parameter for 3.4 nm CdSe/QD with 226 ligands is similar in shape with 3.4

nm/185 OA, slightly ordered but less so compared to order parameter of lipids embedding the smallest 2.6 nm nanocrystal. This trend is not surprising considering that fewer ligands are available to interact with the DOPC molecule in the smallest nanocrystal and in doing can alter the preferred lipid tail ordering.

For 2.6 nm QDs in DMPC lipid, the order parameter of lipids organized as QD concentric shells display the following trend. The shape of the curve constructed from DMPC tails from a circular patch with $r_{cut-off} < 2 - 3$ nm is different from that a QD free bilayer. The second carbon (C_2) displays a considerably lower order parameter. Visually the two monolayers wrapped around the QD resemble a bilayer structure for a cut-off radius larger than 4-5 nm. The decrease in order parameter observed for the adjacent bilayer like regions that correspond to further out from location of embedded QD, corresponds to the bending monolayers changing the sign of bending curvature ($r_{cut-off} \sim 5 - 7$ nm). Beyond this region, $r_{cut-off} \sim 7 - 8$ nm ,the ordering increases for lipids from planar bilayer like conformation; free QD bilayer lipid tail ordering however is not recovered. A similar trend is observed for 3.4 nm QDs passivated with 185 OA or 226 OA (figure 7.4, middle column, row 1 vs. row 2).

The findings for QD/DMPC systems where the order parameters were investigated to record differences with QD initial embedding orientation (T vs. V state, figure 7.5) are reasonable considering different nanocrystal facet ligand populations are interacting with the tails of the embedding lipids. The near collapse of order parameter curves for 2.6 nm QD in 512 DMPC, even for lipids in close proximity of QD can be attributed to the nanocrystal re-orienting itself upwards towards the V-state at later trajectory times (figure 7.7,b) . Simulation snapshots shown in figure 7.1 along with tail order parameter (figure 7.4) calculations suggest that the incorporation of the QD in the gel-phase DSPC causes significant local disruption to the lipid tail order. One limitation of using circular shells to determine the order parameter for DSPC is that each circular lipid selection includes both lipid bilayer like lipid molecules and also lipids interacting with oleic acid molecules. The former lipids no longer resemble a gel structure (figure 7.7). As such the resulting order parameter curves consist of contribution from both gel like lipids and also disrupted or melted lipids. Also, the gel phase structure of DSPC corresponds to lipid tails having a tilt of $\sim 32°$ relative to bilayer normal. The decrease in order parameter with distance from embedded nanocrystal is due to this tilting effect and corresponds to higher fractions of DSPC lipid tails recovering the gel phase conformation.

7.4.3 Lipid Tail Mobility

The phase of the lipids affects the dynamic behavior of lipids/ligand interface. In experiments the melting temperatures (T_m) of lipids used in this study, DMPC, DOPC, DLPC, DSPC are $23°C$,$-20°C$, $-1°C$, and $54.5°C$ respectively (43). The degree of structural disorder of lipids quantified via order parameters need not be an indication of the dynamic fluidity; the behavior of a glassy system is a good analogy. While the structure of a glassy material is amorphous in nature, its molecular movement is considerably slowed down. To address the range and timescale of tail dynamics, we also calculated lipid tail orientational autocorrelation times.

More specifically, as a qualitative indicator of a larger barrier to any major disruption, like ligand exchange processes (28), we calculated the time autocorrelation functions decay in the unit vector (r_{C_4,C_9}) constructed from C_4 to C_9, $sn-2$ tail coordinates. DSPC shows a limited range of motion on the simulation timescale relative to DOPC, with DMPC intermediate, for the locally disordered region, independent of nanocrystal size and ligand density (figure 7.6). The motion of DMPC lipid tail is hindered by the presence of the quantum dot relative to lipids not interacting with the ligands covering the quantum dot. Such occurrence is not observed in lipid DOPC cases most likely due to the presence of the double bond in the DOPC tail imparting additional flexibility.

7.4.4 Other Findings

We also attempted to confirm through simulation QD surface small molecule accessibility and escape with lipid type. Water molecules seem to reach the surface of the quantum dot (figure 7.8). The actual number however corresponds to just several water molecules. The exchange between solvent bulk region and the surface of the quantum dot however is very slow (tens of ns). As such this set of simulations cannot be used to claim an agreement with experimental findings of Salaita et all. regarding small molecule escape originating from presence/absence of nanocrystal oxide shells. Free energy umbrella sampling calculations where water molecules are transferred from the surface of QDs to bulk region could show the free energy differences associated with water/small molecule exchange with different lipid types.

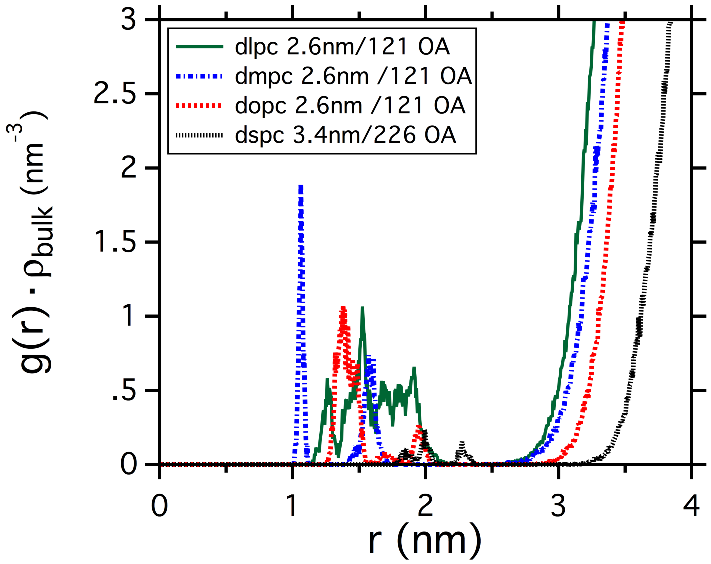

Figure 7.9: Small molecule access through the lipid/ligand interface - Number density function ($g(r)\rho_{bulk}$) vs. distance (r) . The zero point corresponds to the center of quantum dot. The x-axis interval between 2 nm and 3 nm where the number density function vanishes for all lipid systems except DLPC (right panel) corresponds to the region of the OA molecules.

The positioning of embedded quantum dot within the lipid bilayer was presented in figure 7.3 and observed asymmetric. Selective ligand exchange was determined in the work of Zheng et al. The manner in which QD passivated with several large ligands affects the QD embedding ability is unknown. Furthermore, the LUV systems that embed the QDs are circular structures and currently it is also unknown if the curved geometry of the bilayer couples with ligand type used to passivate the bilayer, ligand density, and QD size. Such features can also be evaluated in standard MD simulations of the type introduced here and other advanced free energy simulations methods.

7.5 Conclusions

In simulation the QDs capped with oleic acids remain embedded in all lipid bilayers as predicted in experiments. A slight embedding asymmetry is observed, a slight QD preference for one of the monolayers. This character is more pronounced in DSPC lipid bilayer with a smaller size embedded QD or larger size QD and lower ligand density. When incorporating a 2.6 nm diameter size quantum dot, the ligands are bunched laterally with just a few sticking out towards the lipid headgroups. While a greater number of ligands point towards the PC groups in the cases of 3.4nm QD dot capped with either 226 OA or 185 OA, two populations of ligands are still observed - a set that sticks out in the bilayer midplane and a group that points toward the headgroups. With ligands self-organizing in this manner, it is easy to hypothesize an anisotropic ligand exchange process. The lipid tail disorder in the region of the QD with lipid type was analyzed in two ways. The nanocrystal distance dependent deuterium order parameter ($-S_{CD}$) gives a static measure of likely lipid tail disorder due to the presence of passivating ligands. Smaller size nanocrystal and lower ligand densities induced a lower lipid tail disorder. Free QD bilayer tail ordering is not achieved at distances far away from embedded QD. Lipid tail orientational time autocorrelation functions show that even among DSPC tails that are disordered, reorientational is slower and more limited on the simulation timescale than for DOPC, with DMPC intermediate thus correlating with the melting temperature (T_m)

of lipids.

References

[1] Martin J.D Clift and Vicki Stone. Quantum dots: An insight and perspective of their biological interaction and how this relates to their relevance and clinical use. *Theranostics*, 2(7):668–680, 2012. 149

[2] Sandra J. Rosenthal, Jerry C. Chang, Oleg Kovtun, James R. McBride, and Ian D. Tomlinson. Biocompatible quantum dots for biological applications. *Chemistry & biology*, 18(1):10–24, 2011.

[3] Timothy Jamieson, Raheleh Bakhshi, Daniela Petrova, Rachael Pocock, Mo Imani, and Alexander M. Seifalian. Biological applications of quantum dots. *Biomaterials*, 28(31):4717–4732, 2007.

[4] Prashant K. Jain, Xiaohua Huang, Ivan H. El-Sayed, and Mostafa A. El-Sayed. Noble metals on the nanoscale: Optical and photothermal properties and some applications in imaging, sensing, biology, and medicine. *Accounts of Chemical Research*, 41(12):1578–1586, 2008.

[5] M De, P. S Gosh, and V. M Rotello. Applications of nanoparticles in biology. *Advanced Materials*, 20:4225–4241, 2008. 149

[6] Oliver Schmelz, Alf Mews, Thomas Basch, Andreas Herrmann, and Klaus Mllen. Supramolecular complexes from cdse nanocrystals and organic fluorophors. *Langmuir*, 17(9):2861–2865, 2001. 149

[7] W. William Yu, Lianhua Qu, Wenzhuo Guo, and Xiaogang Peng. Experimental determination of the extinction coefficient of cdte, cdse and cds nanocrystals. *Chemistry of Materials*, 16(3):560–560, 2004.

[8] W. William Yu, Lianhua Qu, Wenzhuo Guo, and Xiaogang Peng. Experimental determination of the extinction coefficient of cdte, cdse, and cds nanocrystals. *Chemistry of Materials*, 15(14):2854–2860, 2003.

[9] A. Striolo, J. Ward, J. M. Prausnitz, W. J. Parak, D. Zanchet, D. Gerion, D. Milliron, and A. P. Alivisatos. Molecular weight, osmotic second virial coefficient, and extinction coefficient of colloidal cdse nanocrystals. *The Journal of Physical Chemistry B*, 106(21):5500–5505, 2002.

[10] X. Michalet, F. F. Pinaud, L. A. Bentolila, J. M. Tsay, S. Doose, J. J. Li, G. Sundaresan, A. M. Wu, S. S. Gambhir, and S. Weiss. Quantum dots for live cells, in vivo imaging, and diagnostics. *Science*, 307(5709):538–544, 2005.

[11] Marcel Bruchez, Mario Moronne, Peter Gin, Shimon Weiss, and A. Paul Alivisatos. Semiconductor nanocrystals as fluorescent biological labels. *Science*, 281(5385):2013–2016, 1998.

[12] Ute Resch-Genger, Markus Grabolle, Sara Cavaliere-Jaricot, Roland Nitschke, and Thomas Nann. Quantum dots versus organic dyes as fluorescent labels. *Nat Meth*, 5(9):763–775, 2008. 149

[13] Ayush Verma and Francesco Stellacci. Effect of surface properties on nanoparticlecell interactions. *Small*, 6(1):12–21, 2010. 150

[14] Andre E. Nel, Lutz Madler, Darrell Velegol, Tian Xia, Eric M. V. Hoek, Ponisseril Somasundaran, Fred Klaessig, Vince Castranova, and Mike Thompson. Understanding biophysicochemical interactions at the nano-bio interface. *Nat Mater*, 8(7):543–557, 2009.

[15] Eun Chul Cho, Leslie Au, Qiang Zhang, and Younan Xia. The effects of size, shape, and surface functional group of gold nanostructures on their adsorption and internalization by cells. *Small*, 6(4):517–522, 2010.

[16] Yuri Roiter, Maryna Ornatska, Aravind R. Rammohan, Jitendra Balakrishnan, David R. Heine, and Sergiy Minko. Interaction of nanoparticles with lipid membrane. *Nano Letters*, 8(3):941–944, 2008.

[17] Yang Li, Xin Chen, and Ning Gu. Computational investigation of interaction between nanoparticles and membranes: Hydrophobic/hydrophilic effect. *The Journal of Physical Chemistry B*, 112(51):16647–16653, 2008. 150, 151

[18] B. Devika Chithrani and Warren C. W. Chan. Elucidating the mechanism of cellular uptake and removal of protein-coated gold nanoparticles of different sizes and shapes. *Nano Letters*, 7(6):1542–1550, 2007. 150

[19] Christina L. Ting and Zhen-Gang Wang. Minimum free energy paths for a nanoparticle crossing the lipid membrane. *Soft Matter*, 8(48):12066–12071, 2012. 150

[20] Haeng Sub Wi, Kyuyong Lee, and Hyuk Kyu Pak. Interfacial energy consideration in the organization of a quantum dot-lipid mixed system. *J. Phys.: Condens. Matter*, 20, 2008. 150, 151

[21] Heeun Jang, Lindsay E. Pell, Brian A. Korgel, and Douglas S. English. Photoluminescence quenching of silicon nanoparticles in phospholipid vesicle bilayers. *Journal of Photochemistry and Photobiology A: Chemistry*, 158(23):111–117, 2003. 151

[22] Gopakumar Gopalakrishnan, Christophe Danelon, Paulina Izewska, Michael Prummer, Pierre-Yves Bolinger, Isabelle Geissbhler, Davide Demurtas, Jacques Dubochet, and Horst Vogel. Multifunctional lipid/quantum dot hybrid

nanocontainers for controlled targeting of live cells. *Angewandte Chemie International Edition*, 45(33):5478–5483, 2006. 151

[23] G. D. Bothun. Hydrophobic silver nanoparticles trapped in lipid bilayers: Size distribution, bilayer phase behavior, and optical properties. *Nanibiotechnol.*, 6:13–23, 2008. 151

[24] Michael Rasch, Emma Rossinyol, Jose Hueso, Brian Goodfellow, Jordi Arbiol, and Brian Korgel. Hydrophobic gold nanoparticle self-assembly with phosphatidylcholine lipid: Membrane-loaded and janus vesicles. *Nano Letters*, 10(9):3733–3739, 2010. 151

[25] Hiroshi Noguchi and Masako Takasu. Adhesion of nanoparticles to vesicles: A brownian dynamics simulation. *Biophysical Journal*, 83(1):299–308, 2002. 151

[26] Edroaldo Lummertz da Rocha, Giovanni Finoto Caramori, and Carlos Renato Rambo. Nanoparticle translocation through a lipid bilayer tuned by surface chemistry. *Physical Chemistry Chemical Physics*, 15(7):2282–2290, 2013.

[27] J. P. Prates Ramalho, P. Gkeka, and L. Sarkisov. Structure and phase transformations of dppc lipid bilayers in the presence of nanoparticles: Insights from coarse-grained molecular dynamics simulations. *Langmuir*, 27(7):3723–3730, 2011. 151

[28] Weiwei Zheng, Liu Yang, Kevin Yehl, Ana West, Erin Shuler, J. T Kindt, and K. Salaita. Molecular engineering of the quantum dot surface using self-assembled lipid bilayer assemblies. *manuscript in preparation*, 2013. 152, 171

[29] E. Rabani. Structure and electrostatic properties of passivated cdse nanocrystals. *J. Chem. Phys.*, 115:1493, 2001. 155, 157

[30] J. Taylor, T. Kippeny, and Sandra J. Rosenthal. Surface stoichiometry of cdse nanocrystals determined by rutherford backscattering spectroscopy. *Journal of Cluster Science*, 12(4):571, 2001. 155

[31] O. Berger, O. Edholm, and F. Jahnig. Molecular dynamicssimulations of a fluid bilayer of dipalmitoylphosphatidylcholine at full hydration, constant pressure, and constant temperature. *Biophysical Journal*, 72:2002–2013, 1997. 155, 157

[32] M. I. Hoopes, M. G. Noro, M. L. Longo, and R. Faller. Bilayer structure and lipid dynamics in a model stratum corneum with oleic acid. *J. Phys. Chem. B*, 115(115):3164–3171, 2011. 155

[33] B. Hess, C. Kutzner, D. van der Spoel, and E. Lindahl. Gromacs 4: Algorithms for highly efficient, load-balanced, and scalable molecular simulation. *J. Chem. Theory Comput.*, 4:435–447, 2008. 156

[34] H. J. C Berendsen, J. P. M Postma, A DiNola, and J. R Haak. Molecular dynamics with coupling to an external bath. *J. Chem. Phys.*, 81:3684 3690, 1984. 156

[35] U. Essman, L. Perera, M. L. Berkowitz, T. Darden, H. Lee, and L. G. Pedersen. A smooth particle mesh ewald method. *J. Chem. Phys.*, 103:8577–8592, 1995. 156

[36] B. Hess, H. Bekker, H. J. C. Berendsen, and J. Fraaije. Lincs: A linear constraint solver for molecular simulations. *J. Comput. Chem*, 18:1463–1472, 1997. 157

[37] S Miyamoto and P. A Kollman. Settle: An analytical version of the shake and rattle algorithms for rigid water models. *J. Comput. Chem.*, 13:952–962, 1992. 157

[38] P. S Coppock and J. T Kindt. Atomistic simulations of mixed-lipid bilayers in the gel and fluid phases. *Langmuir*, 25:352–359, 2009. 157

[39] Chris Neal. personal communication to J.Kindt, University of Toronto, Toronto, 2011. 158

[40] Michael Patra. Lateral pressure profiles in cholesteroldppc bilayers. *European Biophysics Journal*, 35(1):79–88, 2005. 159

[41] Ana West, Kevin Ma, Jonathan L. Chung, and James T. Kindt. Simulation studies of structure and edge tension of lipid bilayer edges: Effects of tail structure and force-field. *The Journal of Physical Chemistry A*, 117:7114,7123, 2013. 165

[42] M. P. Goertz, B. L. Stottrup, J. E. Houston, and X.-Y. Zhu. Nanomechanical contrasts of gel and fluid phase supported lipid bilayers. *The Journal of Physical Chemistry B*, 113(27):9335–9339, 2009. 165

[43] D. Marsh. *Handbook of Lipid Bilayers.* CRC Press, Boca Raton, FL, 1990. 171